

RD-A151 428

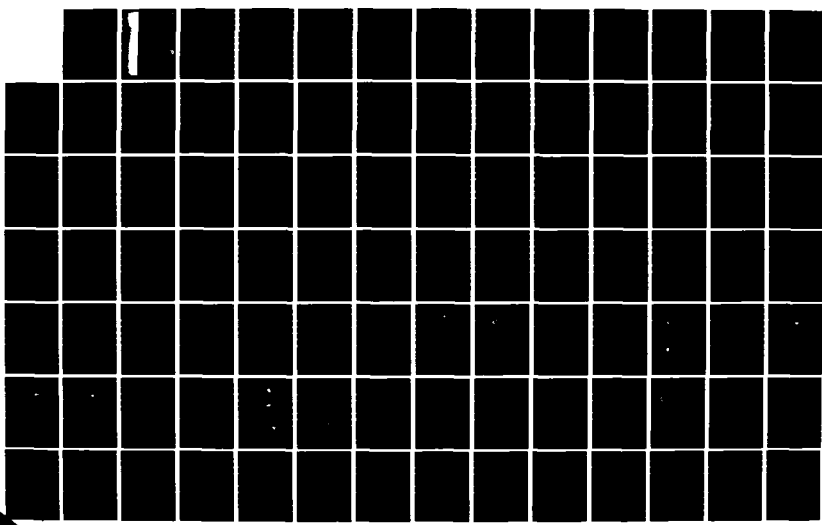
MODIFIED BETATRON ACCELERATOR STUDIES(U) MISSION  
RESEARCH CORP ALBUQUERQUE NM T P HUGHES ET AL. DEC 84  
ANRC-R-655 N60921-84-C-0078

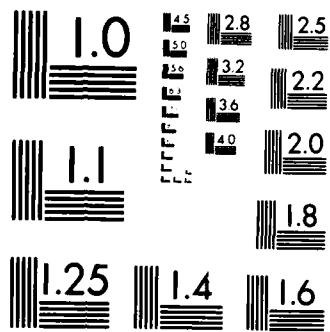
1/2

UNCLASSIFIED

F/G 20/7

NL





MICROCOPY RESOLUTION TEST CHART  
NATIONAL BUREAU OF STANDARDS-1963-A

AD-A151 420

AMRC-R-655  
Copy 40

FINAL REPORT: MODIFIED BETATRON ACCELERATOR STUDIES

Thomas P. Hughes  
Brendan B. Godfrey

December 1984

Prepared for:

Office of Naval Research  
Physical Sciences Division  
800 North Quincy Street  
Arlington, Virginia 22209

Under Contract:

N60921-84-C-0078

DTIC  
ELECTED  
S E D  
MAR 12 1985

Prepared by:

MISSION RESEARCH CORPORATION  
1720 Randolph Road, S.E.  
Albuquerque, New Mexico 87106

DISTRIBUTION IN WHOLE OR IN PART IS PERMITTED FOR ANY PURPOSE  
OF THE UNITED STATES GOVERNMENT. DISTRIBUTION APPROVED FOR  
PUBLIC RELEASE, UNLIMITED DISTRIBUTION.

DTIC FILE COPY

85 02 28 036

## UNCLASSIFIED

SECURITY CLASSIFICATION OF THIS PAGE (When Data Entered)

| REPORT DOCUMENTATION PAGE   |  | READ INSTRUCTIONS BEFORE COMPLETING FORM |
|---|--|--|
| 1. REPORT NUMBER  | 2. GOVT ACCESSION NO.                                      | 3. RECIPIENT'S CATALOG NUMBER            |
|   | AD-A151420   |  |
| 4. TITLE (and Subtitle)<br>Final Report - Modified Betatron Accelerator Studies   | 5. TYPE OF REPORT & PERIOD COVERED<br>Final Report         |  |
| 7. AUTHOR(s)<br>Thomas P. Hughes<br>Brendan B. Godfrey  | 6. PERFORMING ORG. REPORT NUMBER<br>AMRC-R-655             |  |
| 9. PERFORMING ORGANIZATION NAME AND ADDRESS<br>Mission Research Corporation<br>1720 Randolph Road, S.E.<br>Albuquerque, New Mexico 87106  | 8. CONTRACT OR GRANT NUMBER(s)<br>N00014-84-C-0078         |  |
| 11. CONTROLLING OFFICE NAME AND ADDRESS<br>Office of Naval Research<br>800 North Quincy Street<br>Arlington, Virginia 22209   | 10. PROGRAM ELEMENT PROJECT, TASK AREA & WORK UNIT NUMBERS |  |
| 14. MONITORING AGENCY NAME & ADDRESS (if different from Controlling Office)   | 12. REPORT DATE<br>December 1984                           |  |
|   | 13. NUMBER OF PAGES<br>115                                 |  |
|   | 15. SECURITY CLASS (of this report)<br>Unclassified        |  |
|   | 15a. DECLASSIFICATION DOWNGRADING SCHEDULE                 |  |
| 16. DISTRIBUTION STATEMENT (of this Report)<br>DISTRIBUTION IN WHOLE OR IN PART IS PERMITTED FOR ANY PURPOSE OF THE UNITED STATES GOVERNMENT. APPROVED FOR PUBLIC RELEASE, DISTRIBUTION UNLIMITED.  |  |  |
| 17. DISTRIBUTION STATEMENT (of the abstract entered in Block 20, if different from Report)  |  |  |
| 18. SUPPLEMENTARY NOTES   |  |  |
| 19. KEY WORDS (Continue on reverse side if necessary and identify by block number)<br>Betatron<br>Stellatron<br>Negative Mass Instability   |  |  |
| 20. ABSTRACT (Continue on reverse side if necessary and identify by block number)<br>This final report describes work carried out at MRC in the course of the past year on the equilibrium and stability properties of circular accelerators. A rigid-disk beam model in which the fields are treated exactly is used to study linear instabilities. This approach has uncovered an important inductive effect which at high toroidal mode numbers leads to either stability or to a hybrid instability. A corresponding effect has been found in electron-layer geometry. The new theory also shows that moving the equilibrium position toward the (cont'd) |  |  |

UNCLASSIFIED

SECURITY CLASSIFICATION OF THIS PAGE(When Data Entered)

inner wall can stabilize low mode numbers. With the aid of IVORY, simulation results it is shown that the transverse motion of beam particles is a key factor in determining beam stability. The upper bound on particle circulation frequency spread is shown to be a function only of the beam major and minor radii. This leads to upper bounds on stable currents in the modified betatron. Numerical results on stability in the stellatron and reversing-solenoidal-lens betatrons are presented. In addition, the sensitivity of equilibrium particle orbits in the stellatron to initial conditions is calculated. Results are applied to the NRL, UCI and UNM experimental machines where possible.

UNCLASSIFIED

SECURITY CLASSIFICATION OF THIS PAGE(When Data Entered)

## TABLE OF CONTENTS

| Chapter |   | Page |
|---------|---|------|
| I       | INTRODUCTION  | 7    |
| II      | NEGATIVE MASS INSTABILITY LINEAR THEORY   | 10   |
|         | A. DERIVATION OF THE LINEAR DISPERSION RELATION   | 11   |
|         | B. APPROXIMATE SCALINGS OF INSTABILITY GROWTH RATES   | 20   |
|         | C. NUMERICAL SOLUTIONS OF THE LINEAR DISPERSION RELATION  | 28   |
|         | D. SUMMARY AND DISCUSSION   | 43   |
| III     | UPPER BOUNDS ON STABLE CURRENTS IN THE MODIFIED BETATRON  | 47   |
| IV      | STELLATRON ACCELERATOR: EQUILIBRIUM PROPERTIES  | 58   |
|         | A. PARTICLE ORBITS IN THE STELLATRON  | 58   |
|         | B. NUMERICAL SIMULATIONS OF MISMATCHED EQUILIBRIA<br>INCLUDING SELF-FIELDS                          | 62   |
| V       | STELLATRON ACCELERATOR: STABILITY   | 69   |
| VI      | CALCULATIONS FOR THE UCI STELLATRON   | 74   |
|         | A. MOMENTUM COMPACTION  | 74   |
|         | B. TRANSITION FROM POSITIVE TO NEGATIVE MASS  | 75   |
|         | C. SINGLE PARTICLE ORBITS   | 75   |
|         | D. NEGATIVE-MASS INSTABILITY  | 79   |
| VII     | CALCULATIONS FOR THE REVERSING SOLENOIDAL LENS BETATRON   | 81   |
|         | REFERENCES  | 86   |
|         | APPENDIX A - INSTABILITY IN A RELATIVISTIC ELECTRON<br>LAYER WITH A STRONG AZIMUTHAL MAGNETIC FIELD | A-1  |
|         | APPENDIX B - SINGLE-PARTICLE ORBITS IN THE STELLATRON<br>ACCELERATOR                                | B-1  |

|                    |                         |
|--------------------|-------------------------|
| Accession For      |                         |
| NTIS GRA&I         |                         |
| DTIC TAB           |                         |
| Unannounced        |                         |
| Justification      |                         |
| By _____           |                         |
| Distribution/      |                         |
| Availability Codes |                         |
| Dist               | Avail and/or<br>Special |
| A-1                |                         |



## LIST OF ILLUSTRATIONS

| Figure |   | Page |
|--------|---|------|
| 1      | Cross section of rectangular beam in rectangular betatron cavity.   | 12   |
| 2      | Growth rates of the $\lambda = 1$ negative mass instability versus energy for 10 kA and 1 kA beams in 1 kG guide fields.  | 33   |
| 3      | Growth rates of the $\lambda = 10$ negative mass instability versus energy for 10 kA and 1 kA beams in 1 kG guide fields.   | 34   |
| 4      | Growth rates of the $\lambda = 20$ negative mass instability versus energy for 10 kA and 1 kA beams in 1 kG guide fields.   | 35   |
| 5      | Growth rates of the $\lambda = 30$ negative mass instability versus energy for 10 kA and 1 kA beams in 1 kG guide fields.   | 36   |
| 6      | Doppler-shifted frequencies of the modes associated with the $\lambda = 20$ negative mass instability of a 10 kA beam in a 1 kG guide field (Fig. 4).   | 38   |
| 7      | Growth rates of the $\lambda = 1$ negative mass instability versus energy for 10 kA beams in 1 kG, 10 kG, and 100 kG guide fields.  | 39   |
| 8      | Growth rates of the $\lambda = 20$ negative mass instability versus energy for 10 kA beams in 1kG, 10 kG, and 100 kG guide fields.  | 41   |
| 9      | Growth rate of the $\lambda = 20$ inductive instability versus energy of a 10 kA beam in an infinite guide field.   | 42   |
| 10     | Negative mass $\lambda = 1$ growth rates for a 10 kA beam in a 1 kG guide field determined from IVORY simulations compared to dispersion relation results.  | 44   |
| 11     | Negative mass growth rates at various $\lambda$ values for a 10 kA beam in a 1 kg guide field determined from IVORY simulations compared to dispersion relation results. Some simulations employed rigid disks instead of discrete particles. | 45   |
| 12     | In (a) particles have no transverse motion while in (b) particles oscillate about the beam center.  | 48   |
| 13     | Illustration of dependence of toroidal rotation frequency-spread on beam energy.  | 49   |

## LIST OF ILLUSTRATIONS

| Figure |   | Page |
|--------|---|------|
| 14     | Cold beam growth rates of negative mass instability on a 1 kA beam versus beam energy.  | 52   |
| 15     | Particle positions after 140 ns for $\gamma = 20$ beam in zero toroidal magnetic field.   | 55   |
| 16     | Upper bounds on stable currents in the modified betatron for (a) 1 kG and (b) 5 kG toroidal magnetic fields.  | 57   |
| 17     | Magnetic field configuration in the stellatron device, showing the superposition of a vertical mirror field, a toroidal guide field, and a helical quadrupole field.          | 59   |
| 18     | Large envelope oscillations excited in the stellatron by strong quadrupole fields.  | 60   |
| 19     | Numerically integrated orbits of particles which start at (a) $\tilde{r} = -2$ cm, $\tilde{z} = 0$ , $\theta = 0$ , (b) $\tilde{z} = -2$ cm, $\tilde{r} = 0$ , $\theta = 0$ . | 61   |
| 20     | Dependence of amplitude of particle orbits $ \xi $ on strength of quadrupole field, as measured by $\epsilon$ .   | 63   |
| 21     | Contrast between effect of (a) $m > 0$ and (b) $m < 0$ helical windings on particle orbits in the stellatron.   | 64   |
| 22     | Initialization of simulation code for energy mismatch runs.   | 66   |
| 23     | Snapshot of beam with $\gamma = 10$ after 145 ns ( $\approx$ 7 major revolutions).  | 67   |
| 24     | Snapshot of beam with $\gamma = 1.5$ after 42 ns ( $\approx$ 2 major revolutions).  | 68   |
| 25     | Nonlinear development of $\lambda = 8$ negative mass instability in the presence of strong stellatron fields ( $\epsilon = 1.4$ ).  | 71   |
| 26     | $\lambda = 20$ instability of a 10 kA, $\gamma = 7$ beam in a stellatron. This may be a gyrotron-type instability.  | 72   |
| 27     | Inverse of momentum compaction, $1/\alpha$ , versus beam energy in the UCI stellatron, for (a) single particles and (b) the beam centroid.                                    | 76   |

LIST OF ILLUSTRATIONS (Continued)

| Figure |  | Page |
|--------|--|------|
| 28     | Orbits in the UCI stellatron at $\gamma = 9$ for energy-matched particles started in the (a) focusing and (b) defocusing planes. | 77   |
| 29     | Orbits in the UCI stellatron at $\gamma = 9$ with (a) 10% and (b) 20% energy mismatch.   | 78   |
| 30     | Cold beam growth rates for the UCI betatron parameters versus beam energy.   | 80   |
| 31     | Reversing Solenoidal Lens Betatron configuration.  | 82   |
| 32     | Development of $\lambda = 20$ negative mass instability in the RSL.  | 85   |

## LIST OF TABLES

| Table |   | Page |
|-------|---|------|
| 1     | Approximate solutions to the dispersion relation, Eq. (13), for conventional betatrons and for modified betatrons well above the transition energy. Solutions are categorized by the toroidal field strength $B_\theta$ and the coupling coefficient $\chi$ . | 27   |
| 2     | Typical betatron parameters used in numerical solutions of the dispersion relation, Eq. (13).   | 30   |
| 3     | Approximate geometrical factors computed for the parameters in Table 2 at various toroidal mode numbers.  | 30   |
| 4     | Approximate $\ell = 1$ geometrical factors computed for the parameters in Table 2 but with the beam offset radially by various amounts.   | 32   |
| 5     | Modified betatron parameters in IVORY simulations.  | 53   |
| 6     | Summary of examples discussed in text.  | 54   |
| 7     | UCI stellatron parameters.  | 74   |

## I. INTRODUCTION

The modified betatron<sup>1,2</sup> and related devices, like the stellatron<sup>3</sup> and the reversing solenoidal lens (RSL) betatron,<sup>4</sup> are the subjects of theoretical and experimental investigations at present because of their potential as high-current accelerators. For these devices to operate successfully, one must be able to inject a high current beam, in one or many turns, onto a closed orbit in a torus, and maintain beam stability for the duration of the acceleration cycle. The latter may vary from tens of microseconds to several milliseconds. Depending on the application, it may then be necessary to extract the beam from the torus. During the period of our contract with the Office Of Naval Research (01 Nov 1983 - 31 Dec 1984), we have concentrated on the question of beam behavior after injection, i.e., when a circulating ring has been formed, because this behavior determines such key issues as the maximum operating current and the length of the acceleration cycle. One of the main concerns in this regard is collective instabilities, including the negative-mass instability,<sup>5-7</sup> which can grow on the beam. We have developed a new analytic theory of these instabilities as they occur in the modified betatron configuration. Excellent agreement is obtained between the theory and particle simulation results over a wide range of energy and wavelengths. In particular, the short-wavelength regime, which has not been adequately treated to date, is covered by the new theory. This allows us to obtain the scaling of growth rate with toroidal mode-number. Six regimes of behavior are identified, according to the magnitude of the toroidal magnetic field and the strength of the coupling between longitudinal and transverse motion (Table 1). We find that some subtle geometric effects have a considerable influence in beam stability. Ways to take advantage of these effects are discussed. A criterion for beam stability below the negative mass transition energy is given (Eq. 65). We can recover all the known limiting cases of the negative mass dispersion relation from the theory. The model we use provides an analytical framework into which one can, at some future date, incorporate in a straight-forward manner the effects of strong-focusing fields. This work is presented in Chap. II.

Numerical simulation results are presented in Chap. III which clearly illustrate how the equilibrium transverse motion of the beam particles influences beam stability. It is found that, for a given beam radius, the most stable configuration occurs when there is little or no transverse motion of beam particles. This is an important result, since, as we shall show, it follows that one does not necessarily require an energy spread to achieve maximum stability. Using the analytic results of Chap. II, we compute upper bounds on the currents stable to collective instabilities.

The linear theory of the stellatron and RSL betatron has not yet been worked out. However, we have performed several numerical simulations of these devices. Results for the stellatron in Chap. V show that in most of the cases looked at, the quadrupole fields decrease, but do not eliminate, the growth of instabilities. We present some evidence that the negative-mass transition in the stellatron gives a threshold for beam stability at moderate currents ( $\sim 1$  kA). The stability of the stellatron experiment at the University of California at Irvine<sup>8</sup> is addressed in Chap. VI. Limited results on the stability of the RSL betatron are given in Chap. VII.

In addition to looking at collective instabilities, we have looked at some questions relating to particle orbits in the stellatron and RSL devices. Regarding the stellatron, we find in Chap. IVA that in certain regimes the orbit of a particle is sensitive to small changes in the initial conditions. This has practical implications for where one should locate the beam injector in such a device. We have also done some self-consistent (i.e., including self-fields) simulations of a highly mismatched beam in the stellatron (Chap. IVB). For the RSL betatron, we have looked at a system whose parameters are close to those for the experimental device under construction at the University of New Mexico. The results in Chap. VII show that by adjusting the solenoidal fields, radial oscillations of the beam envelope can be made negligible even when there is a sizeable gap between the solenoids.

A discussion of an inductively-driven instability in an electron-layer which is analogous to that found in toroidal geometry (Chap. II) is given in Appendix A. Appendix B gives details of our work on single-particle orbits in the stellatron.

## II. NEGATIVE MASS INSTABILITY LINEAR THEORY

In our last annual report we described an analytical rigid-disk model of long wavelength negative mass instabilities in large aspect ratio conventional and modified betatrons for which the cavity and electron beam minor cross sections are concentric circles.<sup>7</sup> This work represented a significant advance over earlier studies<sup>9,10</sup> in that it took proper account of toroidal corrections to the electromagnetic fields. Agreement between model predictions of the negative mass growth rate and the results of numerical simulations was quite good.<sup>6</sup> However, this agreement showed signs of deteriorating at high beam energy and, of course, at large toroidal mode numbers (i. e., short wavelengths).

During the past year we have relaxed all approximations but that of a rigid-disk beam. The self-consistent electromagnetic fields of the electron beam in the accelerator cavity are evaluated exactly for arbitrary beam and cavity dimensions and arbitrary aspect ratios. In addition, the beam need not be centered radially in the cavity. These improvements are made possible by taking the beam and cavity to have rectangular minor cross sections. This requirement is not as limiting at it might seem at first glance. Three-dimensional numerical simulations with the IVORY code indicate that beam behavior in cavities of approximately square cross section is little different from that in cavities of circular cross section provided the cross sectional areas are equal. The new model gives even better agreement than its predecessor with negative mass instability linear growth rates from numerical simulations. In particular, discrepancies with the few simulations performed at high energies and at large toroidal mode numbers have been eliminated.

Some new effects are predicted by the revised model. Inductive electric fields dominate electrostatic fields at large toroidal mode numbers, giving rise to reduced instability growth rates and, for a few modes, even a stability window. It appears that the stability window can be shifted to low toroidal modes by moving the electron beam toward the inner wall of the cavity. We plan to investigate this interesting behavior in more detail

Instabilities in a modified betatron can be evaluated in a manner similar to that used for the conventional betatron provided the poloidal cyclotron frequency,  $B_\theta/\gamma$ , significantly exceeds the toroidal cyclotron frequency,  $\omega_0$ . We distinguish between beam energies comparable to and much greater than the transition energy,  $\gamma_{tr}$ , defined as the energy at which  $\omega_z$  vanishes. Since the former regime has no counterpart in the conventional betatron, we consider it later.

For the modified betatron at high energies, Eq. (13) reduces to

$$\Omega^4 - \Omega^2 \left( \omega_B^2 + \epsilon_0 \right) - \frac{\omega_B^2 \chi}{B_\theta^2/\gamma^2} = 0 \quad (52)$$

where

$$\omega_B^2 = \omega_r^2 \omega_z^2 / (B_\theta^2/\gamma^2) \quad (53)$$

is the poloidal drift frequency. (In obtaining these expressions we have assumed also that  $\epsilon \ll \omega_0^2$ , which is true in most cases of interest.) Solutions to Eq. (52) are

$$\Omega^2 \approx \frac{\omega_B^2 + \epsilon_0}{2} \pm \left[ \left( \frac{\omega_B^2 + \epsilon_0}{2} \right)^2 + \frac{\omega_z^2 \chi}{B_\theta^2/\gamma^2} \right]^{1/2} \quad (54)$$

As before, we consider the limits of small and large  $\chi$ . For small  $\chi$  Eq. (54) reduces to

$$\Omega^2 \approx \omega_B^2 + \epsilon_0, \quad - \frac{\omega_z^2 \chi}{B_\theta^2/\gamma^2} / (\omega_B^2 + \epsilon_0) \quad (55)$$

When  $\omega_B^2 \gg \epsilon_0$ , Eq. (55) in turn becomes

$$\Omega^2 \approx \omega_B^2, \quad - \chi/\omega_r^2 \quad (56)$$

For small  $\chi$ , i. e., weak coupling between longitudinal and transverse beam modes,

$$\frac{4\chi}{\omega_r^2} \approx \left(\frac{2\ell}{1-n}\right)^2 \frac{v}{\gamma} \left(g_3 - g_4 v_\theta^2\right) < 1 \quad (48)$$

the two pairs of roots in Eq. (47) reduce to

$$\Omega = \omega_r^2, -\chi/\omega_r^2 \quad (49)$$

The former represents transverse (in  $r$ ) oscillations, which are stable, and the latter represents predominantly longitudinal oscillations, one of which is unstable with a growth rate

$$\Gamma = \frac{\ell}{R} \left[ \frac{1}{1-n} \frac{v}{\gamma} \left( g_3 - g_4 v_\theta^2 \right) \right]^{1/2} \quad (50)$$

if  $\chi$  (equivalently,  $\epsilon_0$ ) is positive. Eq. (50) becomes the usual negative mass instability growth rate expression when  $g_3 = g_4$ .<sup>14,15</sup> However, the instability vanishes, if  $\chi$  is negative. This stabilization of the negative mass effect is caused by inductive coupling of the beam to the accelerator cavity,<sup>16,17</sup> which is discussed further in the next section.

With increasing  $\ell$  the inequality (48) eventually is reversed, giving rise to strong coupling between the longitudinal and transverse modes. One unstable hybrid mode with a growth rate

$$\Gamma = \frac{\ell^{1/2}}{R} \left[ \frac{v}{\gamma} \left( g_3 - g_4 v_\theta^2 \right) \right]^{1/4} \quad (51)$$

occurs if  $\chi$  is positive, and two unstable modes with growth rates reduced from Eq. (51) by  $\sqrt{2}$  occur otherwise. Numerical calculations performed to date suggest that the latter possibility is much more common. Note that the growth rate at large  $\ell$ , Eq. (51), scales as  $\ell^{1/2}$ , in contrast to the growth rate at small  $\ell$ , Eq. (50), which scales as  $\ell$ .

Although the precise values of  $g_1$  and  $g_2$  are not critical, the three remaining coefficients must be determined quite accurately. Expanding Eq. (40) and dropping small terms proportional to  $\Omega^2$  and  $v^2$  yields

$$x = 2\omega \omega_0 \frac{\ell}{R^2} \frac{v}{\gamma} (g_5 - g_4 v_\theta^2) + \frac{\ell^2}{R^4} \frac{v}{\gamma} (g_3 - g_4 v_\theta^2) \quad (43)$$

Thus, the coupling term  $x$  between longitudinal and transverse beam modes depends sensitively upon the differences between  $g_5$  and  $g_4$ , and  $g_3$  and  $g_4$ . Numerical evaluations of these factors indicate that the second term in Eq. (43) is more often the larger, in which case

$$x \approx \frac{\gamma^2}{R^2} \epsilon_0 \quad (44)$$

where  $\epsilon_0$  is  $\epsilon$  evaluated at  $\Omega = 0$ .

Let us now specialize to a high current conventional betatron, for which the general dispersion relation is

$$(\Omega^2 - \omega_r^2)(\Omega^2 - \epsilon) = x \quad (45)$$

For an equilibrium to exist in the conventional betatron at high current,  $\gamma$  must be sufficiently large that the first term in Eq. (38) dominates the second. Then, Eq. (45) becomes approximately

$$\Omega^4 - \omega_r^2 \Omega^2 - x = 0 \quad (46)$$

with solutions

$$\Omega^2 = \frac{\omega_r^2}{2} \pm \left[ \left( \frac{\omega_r^2}{2} \right)^2 + x \right]^{1/2} \quad (47)$$

less accurate but still tolerable. This is not true of Eq. (17), however, due to a strong cancellation between electrostatic and inductive contributions. With these approximations the terms occurring in the dispersion relation take the form

$$\omega_z^2 \approx n \omega_0^2 - g_1 \frac{2v}{\gamma b^2} \quad (37)$$

$$\omega_r^2 \approx (1 - n) \omega_0^2 - g_2 \frac{2v}{\gamma b^2} \quad (38)$$

$$\epsilon \approx \frac{v}{\gamma^3} \left( g_3 \frac{\ell^2}{R^2} - g_4 \omega^2 \right) \quad (39)$$

$$x \approx \left( \gamma \omega_0 \Omega + \frac{v}{\gamma^2} \frac{\ell}{R^2} g_5 \right)^2 - \gamma^2 \omega_0^2 (\Omega^2 - \epsilon) \quad (40)$$

where  $v$  is the beam current normalized to 17 kA. For a square beam roughly centered in a square cavity, the five geometrical factors are approximately

$$g_1 \approx g_2 \approx 1 \quad (41)$$

$$g_3 \approx g_4 \approx g_5 \approx \frac{1}{2} + \ln \left( \frac{A_c}{A} \right) \quad (42)$$

as can be verified numerically.  $A_c$  is the cavity cross sectional area, defined similarly to  $A$ .

Recall that  $\alpha$ , which typically is of order unity, occurs only in Eq. (15). The eigenfunctions entering into Eq. (29)-(32) are

$$g_E^\lambda = C_E^{-1/2} \left[ J_\lambda(\ell_{\lambda_E} r) Y_\lambda(\ell_{\lambda_E} r_2) - J'_\lambda(\ell_{\lambda_E} r_2) Y_\lambda(\ell_{\lambda_E} r) \right] \quad (33)$$

$$g_B^\lambda = C_B^{-1/2} \left[ J_\lambda(\ell_{\lambda_B} r) Y'_\lambda(\ell_{\lambda_B} r_2) - J'_\lambda(\ell_{\lambda_B} r_2) Y_\lambda(\ell_{\lambda_B} r) \right] \quad (34)$$

The quantities  $J_\lambda$  and  $Y_\lambda$  are standard Bessel functions of the first and second kinds.<sup>12</sup> A prime indicates differentiation with respect to the argument. The normalization constants in these expressions are<sup>13</sup>

$$C_E = \frac{1}{2} \left[ r^2 (g_E^\lambda')^2 \right]_{r_1}^{r_2} \quad (35)$$

$$C_B = \frac{1}{2} \left[ \left( r - \frac{\lambda}{\ell_{\lambda_B}} \right)^2 (g_B^\lambda)^2 \right]_{r_1}^{r_2} \quad (36)$$

Accurate solutions of Eqs. (13)-(36) clearly must be obtained numerically. However, a qualitative picture of instability scaling can be developed with surprising ease.

## B. Approximate Scalings of Instability Growth Rates

The negative mass and related instabilities typically occur at frequencies approximated by  $\Omega \approx 0$ . Thus, provided  $\ell\omega_0$  is well below the electromagnetic cutoff for toroidal mode  $\ell$  of the betatron cavity, which is usually the case, we can safely replace  $\omega$  by  $\ell\omega_0$  in the denominators of the field contributions (the sums) in Eqs. (14)-(17). Making the same substitution in the numerators of the field contributions in Eqs. (14)-(16) is

$$\ell_{\lambda_B} = \begin{cases} \frac{\lambda}{R} & n = 0 \\ \frac{2\pi}{r_2 - r_1} n & n > 0 \end{cases} \quad (26)$$

(The lowest electric eigenvalue is, of course, not included in the sums.) However, as  $\lambda$  increases and the magnitude of the lowest magnetic eigenvalue approaches that of the second lowest, the values of the low-lying electric and magnetic eigenvalues are pushed up.

The radial form factors are expressed as integrals over the vacuum eigenfunctions, because simpler expressions do not, in general, exist.

$$\rho_E^\lambda = \int_{w_1}^{w_2} g_E^\lambda r dr \quad (27)$$

$$\hat{\rho}_E^\lambda = - \ell_{\lambda_E} \int_{w_1}^{w_2} g_E^{\lambda'} r dr \quad (28)$$

$$\rho_B^\lambda = \int_{w_1}^{w_2} g_B^\lambda \frac{r}{R} r dr \quad (29)$$

$$\hat{\rho}_B^\lambda = - \ell_{\lambda_E} \int_{w_1}^{w_2} g_B^{\lambda'} \frac{r}{R} r dr \quad (30)$$

$$\tilde{\rho}_B^\lambda = \int_{w_1}^{w_2} g_B^\lambda \frac{R}{r} r dr \quad (31)$$

and

$$\alpha = \left[ g_\lambda^E - r \ell_{\lambda_E} g_\lambda^{E'} \right]_{w_1}^{w_2} / \rho_E^\lambda \quad (32)$$

with, from Eq. (6),

$$\beta = \gamma^3 \omega_0 - \frac{\rho}{V_\theta A} \sum_{k, \lambda_E} \frac{(\rho_B)^2 \rho_E^\lambda \hat{\rho}_E^\lambda}{k^2 + \omega_{\lambda_E}^2} \quad (19)$$

Sums in the preceding six equations are performed over the axial and radial eigenvalues of the vacuum electromagnetic fields in the toroidal cavity. The axial eigenvalues are given by

$$k = \frac{2\pi}{a} n \quad n = [0, \infty) \quad (20)$$

The axial form factors  $\rho_E^k$  and  $\rho_B^k$  are obtained by integrating the corresponding eigenfunctions, sines and cosines, over the beam cross section.

$$\rho_E^k = \begin{cases} \frac{2b}{\sqrt{2a}} & n = 0 \\ 0 & n \text{ odd} \\ \frac{2}{\sqrt{a}} \frac{\sin(kb)}{k} & n \text{ even } (n > 0) \end{cases} \quad (21)$$

$$\rho_B^k = \begin{cases} \frac{2}{\sqrt{a}} \frac{\sin(kb)}{k} & n \text{ odd} \\ 0 & n \text{ even} \end{cases} \quad (22)$$

The radial eigenvalues satisfy the usual vacuum dispersion relations:

$$J_\lambda(\ell_{\lambda_E} r_1) Y_\lambda(\ell_{\lambda_E} r_2) - J_\lambda(\ell_{\lambda_E} r_2) Y_\lambda(\ell_{\lambda_E} r_1) = 0 \quad (23)$$

$$J_\lambda'(\ell_{\lambda_B} r_1) Y_\lambda'(\ell_{\lambda_B} r_2) - J_\lambda'(\ell_{\lambda_B} r_2) Y_\lambda'(\ell_{\lambda_B} r_1) = 0 \quad (24)$$

For low mode numbers,  $\lambda$ , these eigenvalues can be approximated as

$$\ell_{\lambda_E} = \begin{cases} 0 & n = 0 \\ \frac{2\pi}{r_2 - r_1} n & n > 0 \end{cases} \quad (25)$$

the longitudinal oscillation frequency (squared) by

$$\epsilon = - \frac{\rho}{\gamma^3 A} \left\{ \frac{\lambda^2}{R^2} \sum_{k, \lambda_E} \frac{(\rho_B k \hat{\rho}_E \lambda)^2}{(k^2 + \lambda_{\lambda_E}^2 - \omega^2) \lambda_{\lambda_E}^2} (\lambda_{\lambda_E}^2 - \omega^2) \right. \\ \left. - \omega^2 \sum_{k, \lambda_B} \frac{(\rho_B k \hat{\rho}_E \lambda)^2}{(k^2 + \lambda_{\lambda_B}^2 - \omega^2) \lambda_{\lambda_B}^2} \right\} \quad (16)$$

and the coupling coefficient by

$$\chi = \left\{ \frac{\beta}{\gamma^2} \Omega + \frac{\rho}{\gamma^2 A} \left[ \frac{\lambda}{R} \sum_{k, \lambda_E} \frac{(\rho_B k)^2 \hat{\rho}_E \lambda \hat{\rho}_E \lambda}{(k^2 + \lambda_{\lambda_E}^2 - \omega^2) \lambda_{\lambda_E}^2} \right. \right. \\ \left. \left. + \omega \sum_{k, \lambda_B} \frac{(\rho_B k)^2 [V_\theta \lambda_{\lambda_B}^2 \hat{\rho}_B \lambda - \frac{\lambda}{R} \omega \hat{\rho}_B \lambda] \hat{\rho}_B \lambda}{(k^2 + \lambda_{\lambda_B}^2 - \omega^2) \lambda_{\lambda_B}^2} \right] \right\}^2 \\ - \frac{\beta}{\gamma^2} (\Omega^2 - \epsilon) \quad (17)$$

$B_z^0$  is the applied vertical magnetic field, and  $n$  is the betatron index. The vertical field is determined from radial force balance, Eq. (1).

$$B_z^0 = -\beta - \frac{\rho V_\theta}{A} \sum_{k, \lambda_B} \frac{(\rho_B k)^2 \hat{\rho}_B \lambda \hat{\rho}_B \lambda}{k^2 + \lambda_{\lambda_B}^2} \quad (18)$$

$$\omega_z^2 = -n\omega_0 \frac{B_z^0}{\gamma}$$

$$- \frac{\rho}{\gamma A} \left\{ \sum_{k, \ell_{\lambda_E}} \frac{(\rho_E k \rho_E \lambda)^2}{(k^2 + \ell_{\lambda_E}^2 - \omega^2) \ell_{\lambda_E}^2} \left[ (k^2 - \Omega^2) \ell_{\lambda_E}^2 - (\ell \omega_0 k)^2 \right] \right.$$

$$- \sum_{k, \ell_{\lambda_E}} \frac{(\rho_B k \rho_E \lambda)^2 k^2}{k^2 + \ell_{\lambda_E}^2}$$

$$- v_\theta^2 \sum_{k, \ell_{\lambda_B}} \frac{(\rho_E k \rho_B \lambda)^2 k^2}{(k^2 + \ell_{\lambda_B}^2 - \omega^2) \ell_{\lambda_B}^2} + v_\theta^2 \sum_{k, \ell_{\lambda_B}} \frac{(\rho_B k \rho_B \lambda)^2 k^2}{(k^2 + \ell_{\lambda_B}^2) \ell_{\lambda_B}^2} \quad (14)$$

$$\omega_r^2 = n\omega_0 \frac{B_z^0}{\gamma} + \omega_0^2 - \frac{\beta}{\gamma} \omega_0 + \frac{\beta^2}{\gamma}$$

$$- \frac{\rho}{\gamma A} \left\{ \sum_{k, \ell_{\lambda_E}} \frac{(\rho_B k \rho_E \lambda)^2}{(k^2 + \ell_{\lambda_E}^2 - \omega^2) \ell_{\lambda_E}^2} (\ell_{\lambda_E}^2 - \omega^2) - \sum_{k, \ell_{\lambda_E}} \frac{(\rho_B k \rho_E \lambda)^2}{k^2 + \ell_{\lambda_E}^2} \right\}$$

$$- \sum_{k, \ell_{\lambda_B}} \frac{(\rho_B k [v_\theta \ell_{\lambda_B} \rho_B \lambda - \ell \omega / R \tilde{\rho}_B \lambda])^2}{(k^2 + \ell_{\lambda_B}^2 - \omega^2) \ell_{\lambda_B}^2} + v_\theta^2 \sum_{k, \ell_{\lambda_B}} \frac{(\rho_B k \rho_B \lambda)^2}{k^2 + \ell_{\lambda_B}^2} \quad (15)$$

For the calculations outlined below, it is convenient to express Maxwell's equations for the perturbed field quantities as a vector wave equation for the electric fields,

$$\left( \frac{\partial^2}{\partial t^2} - \nabla^2 \right) \delta E = - \frac{\partial}{\partial t} \delta J - \nabla \delta p \quad (11)$$

Once Eq. (11) is solved, the magnetic fields are determined simply from

$$\frac{\partial}{\partial t} \delta B = - \nabla \times \delta E \quad (12)$$

The solution of Eq. (1)-(12) is straightforward but very time-consuming. It proceeds as follows. The perturbed quantities are taken to have azimuthal and temporal variations of the usual form  $\exp[i(\ell\theta - \omega t)]$ . Eq. (11) together with its source terms, Eq. (7)-(10), are then solved for the perturbed electric fields using vector Green's functions in cylindrical coordinates.<sup>11</sup> Next, the perturbed magnetic fields are obtained by direct substitution in Eq. (12). The equilibrium fields are determined in a similar manner. (Note that the electric and magnetic fields also can be derived starting from scalar Green's functions for  $E_z$  and  $B_z$ . However, we have found the resulting infinite series to be more prone to numerical difficulties.) Eliminating the various field components from Eq. (3)-(5) then leaves a Hermitian matrix equation for the perturbed beam centroid location. Its determinant is the desired dispersion relation.

The dispersion relation, cast in the form used in our earlier work<sup>6,7</sup>, is

$$\left( \Omega^2 - \omega_z^2 \right) \left( \Omega^2 - \omega_r^2 - \frac{x}{\Omega^2 - \epsilon} \right) - \Omega^2 \frac{B_\theta^2}{\gamma^2} = 0 \quad (13)$$

where  $\Omega = \omega - \ell\omega_0$  and  $\omega_0 = V_\theta/R$ . The axial and radial oscillation frequencies are given by

$$\gamma^3 R \delta\ddot{\theta} = -\beta \delta\dot{r} + \frac{1}{A} \int \frac{r}{R} \delta E_\theta dA \quad (5)$$

with

$$\beta = \gamma^3 \frac{V_\theta}{R} - \frac{E_r}{V_\theta} \quad (6)$$

Perturbed quantities are preceded by a delta (e.g.,  $\delta z$ ), while unperturbed quantities are not. Total time derivatives of perturbed beam quantities are represented by dots above those quantities (e.g.,  $\delta\dot{z}$ ).  $B_\theta$  is the toroidal magnetic field, averaged over the beam cross section.

Perturbed beam current and charge densities arising from these motions are

$$\delta J_z = \rho \delta\dot{z} \quad (7)$$

$$\delta J_r = \rho \delta\dot{r} \quad (8)$$

$$\frac{1}{r} \delta J_\theta = \rho \delta\dot{\theta} + \frac{V_\theta}{R} \delta\rho \quad (9)$$

and

$$\delta\rho = -\frac{\partial}{\partial z} \rho \delta z - \frac{1}{r} \frac{\partial}{\partial r} r \rho \delta r - \frac{\partial}{\partial \theta} \rho \delta\theta \quad (10)$$

With the exception of Eq. (9), which has been modified to take account of the beam azimuthal velocity variation with radius, these equations are taken directly from Ref. 6. It is easy to show that they satisfy the continuity equation.

balance equation is given by

$$\frac{1}{A} \int \left( E_r + \frac{v_\theta}{R} r B_z \right) dA + \gamma \frac{v_\theta^2}{R} = 0 \quad (1)$$

In arriving at Eq. (1), we have taken the beam density to be constant and, consistent with the rigid-disk approximation, the beam velocity to vary linearly with radius.  $R$  is the charge-weighted equilibrium radius,  $v_\theta$  is the velocity at that location,  $A$  is the cross sectional area of the beam, and  $dA = r dr dz$ .

$$R = \frac{1}{A} \int r dA, \quad A = \int dA \quad (2)$$

Note that the speed of light and the electron charge and mass are scaled out of our equations. This has the effect of measuring distance and time relative to an arbitrary scale length, and potentials relative to the electron rest energy.

The linearized equations for beam motion about its equilibrium position are obtained in a similar manner.<sup>7,9</sup>

$$\begin{aligned} \gamma \delta \ddot{z} &= \frac{1}{A} \int \left( \delta E_z - \frac{v_\theta}{R} r \delta B_r \right) dA + B_\theta \delta \dot{r} \\ &+ \frac{1}{A} \int \left( \frac{\partial E_z}{\partial z} - \frac{v_\theta}{R} r \frac{\partial B_r}{\partial z} \right) dA \delta z \end{aligned} \quad (3)$$

$$\begin{aligned} \gamma \delta \ddot{r} &+ \frac{1}{A} \int \left( \delta E_r + \frac{v_\theta}{R} r \delta B_z \right) dA - B_\theta \delta \dot{z} \\ &+ \frac{1}{A} \int \left( \frac{\partial E_r}{\partial r} + \frac{v_\theta}{R} r \frac{\partial B_z}{\partial r} \right) dA \delta r \\ &+ \left( \beta \frac{v_\theta}{R} - \gamma \frac{v_\theta^2}{R^2} \right) \delta r + \beta R \delta \dot{\theta} \end{aligned} \quad (4)$$

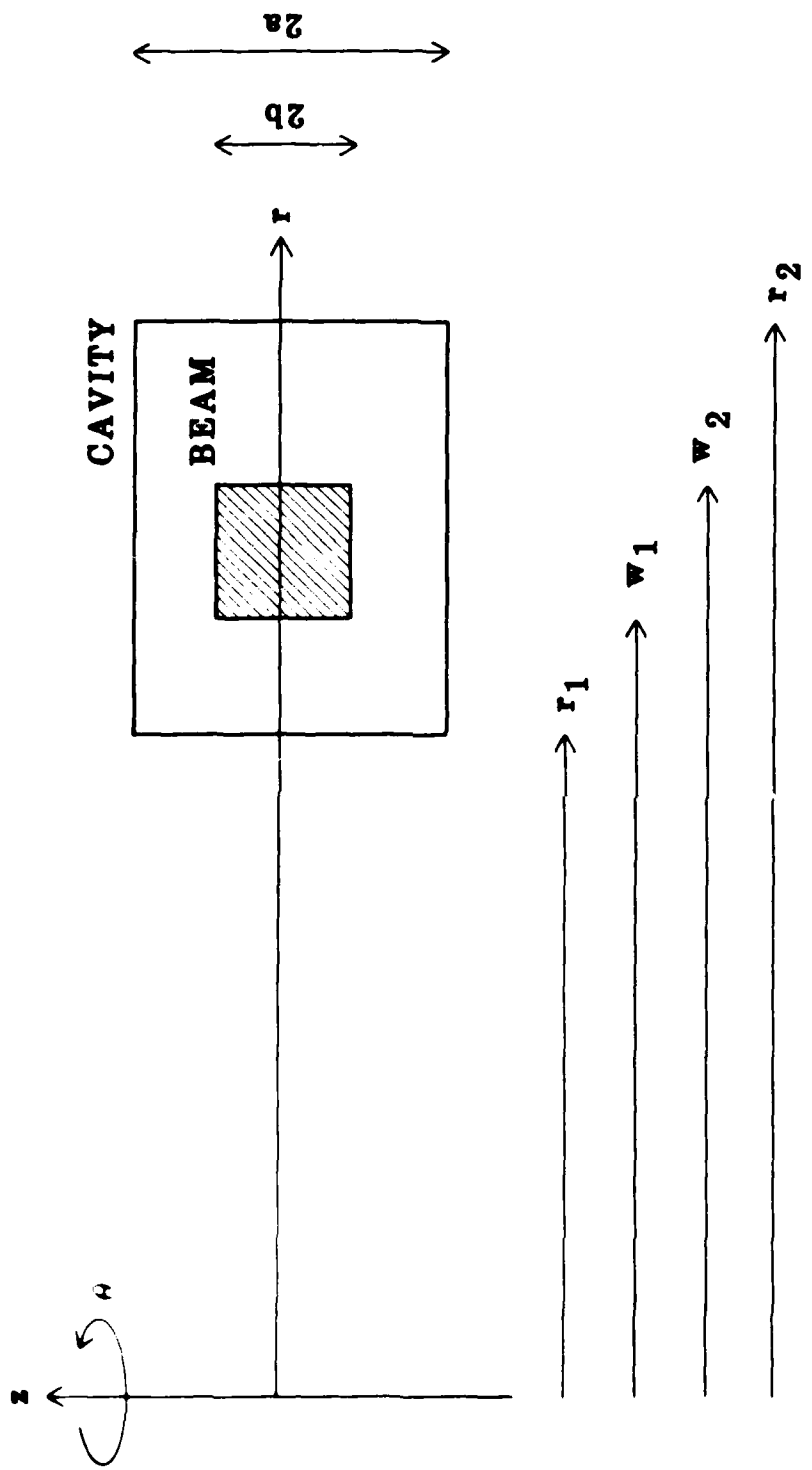


Figure 1. Cross section of rectangular beam in rectangular betatron cavity.

(including IVORY simulations) in the coming year. (The analogous, but much simpler, case of inductive effects in a fast rotating e-layer immersed in a strong azimuthal magnetic field is treated briefly in Appendix A. Besides providing a check on the betatron results, it permits more insight into the underlying physics.) High-frequency electromagnetic effects on betatron stability also were investigated but were found to be small for cavity cross sections of moderate size.

The remainder of this chapter is organized as follows. In Section A the beam equations of motion are specified, and the electromagnetic fields are evaluated by a Green's function expansion. Although the resulting dispersion relation is algebraically very complicated, useful analytical growth rate expressions can be derived in several limiting cases, described in Section B. The numerical results in Section C support and extend our analytic findings for 1 and 10 kA beams over a wide range of magnetic fields and mode numbers. IVORY comparisons also are provided. Our results are summarized, their implications discussed, and directions of further linear stability research suggested in Section D.

#### A. Derivation of the Linear Dispersion Relation

We consider a rectangular beam in a rectangular torus with dimensions as shown in Fig. 1. In general, the beam cross section need not be the same shape as that of the torus, and the beam need not be centered radially. Axial centering is, of course, required for a static equilibrium.

As in earlier works,<sup>6,7,9,10</sup> we treat the beam as a string of non-rotating rigid disks. Thus, the internal dynamics of the beam, and temperature effects in particular, are ignored. (Negative mass instability stabilization by an electron energy spread is discussed in Chapter III of this report, and elsewhere.<sup>5,7</sup>) Within this context the beam centroid equations of motion are obtained by integrating the single particle equations over the beam cross section. Thus, the beam equilibrium radial force

Note that the second root in Eq. (56) is identical to that in Eq. (49). Consequently, the toroidal magnetic field has no effect on the negative mass instability whenever

$$\frac{B_\theta^2}{R^2} \nu \frac{\ell^2}{R^2} < \gamma^5 \omega_z^2 \omega_r^2 / (g_3 - g_4 v_\theta^2) \quad (57)$$

Very large currents and applied fields are needed to violate this inequality, except at small  $\gamma$ .

In the opposite limit Eq. (55) simplifies to

$$\omega^2 \sim \epsilon_0 \frac{\omega_z^2 \chi / \epsilon_0}{B_\theta^2 / \gamma^2} \quad (58)$$

The second of these roots can be simplified by means of Eq. (44) to the usual negative mass instability growth rate expression for very large toroidal fields,<sup>18</sup>

$$\Gamma \sim (1 - n)^{-1/2} \gamma \omega_B \quad (59)$$

which is independent of both  $\ell$  and  $v$ . The first root in Eq. (58) is purely longitudinal. Instability results for  $\epsilon_0 < 0$ , i. e., for inductive electric fields dominating over electrostatic.

Returning to Eq. (54), we find that the large  $\chi$  limit corresponds to a strong coupling between longitudinal and transverse modes, just as in the conventional betatron. The growth rate here is simply that described by Eq. (51), reduced by of order  $(B_z/B_\theta)^{1/2}$ .

$$\Gamma \approx \left( \frac{\omega_z}{B_\theta/\gamma} \right)^{1/2} \frac{\epsilon^{1/2}}{R} \left[ \frac{v}{\gamma} \left( g_3 - g_4 v_\theta^2 \right) \right]^{1/4} \quad (60)$$

The various cases we have considered thus far for both the conventional and the modified betatron are categorized in Table 1 according to the magnitudes of  $w_B$  and  $\chi$ .

It is more difficult to obtain useful instability growth rate estimates for the modified betatron at low beam energies, because the ordering of most terms in the dispersion relation is not uniform. Replacing  $\epsilon$  by  $\epsilon_0$  often is particularly dubious. Nonetheless, some progress can be made for  $\omega_z^2$  near zero, provided  $\omega_r^2$  also is small there. In this case the dispersion relation reduces approximately to

$$\Omega^4 - \Omega^2 \epsilon \left( 1 - \frac{\chi/\epsilon}{B_\theta^2/\gamma^2} \right) - \frac{\chi \omega_z^2}{B_\theta^2/\gamma^2} = 0 \quad (61)$$

which has as a formal solution

$$\Omega^2 \approx \frac{\epsilon}{2} \left( 1 - \frac{\chi/\epsilon}{B_\theta^2/\gamma^2} \right) \pm \left[ \left( \frac{\epsilon}{2} \right)^2 \left( 1 - \frac{\chi/\epsilon}{B_\theta^2/\gamma^2} \right)^2 + \frac{\chi \omega_z^2}{B_\theta^2/\gamma^2} \right]^{1/2} \quad (62)$$

As  $\omega_z^2$  goes to zero, so does one root of Eq. (62), and replacing  $\epsilon$  by  $\epsilon_0$  becomes permissible.

$$\Omega^2 \approx - \frac{\gamma^2 \omega_0^2 \omega_z^2}{B_\theta^2/\gamma^2} / \left( 1 - \frac{\gamma^2 \omega_0^2}{B_\theta^2/\gamma^2} \right) \quad (63)$$

TABLE 1. Approximate solutions to the dispersion relation, Eq. (13), for conventional betatrons and for modified betatrons well above the transition energy. Solutions are categorized by the toroidal field strength  $B_\theta$  and the coupling coefficient  $\chi$ .

| $B_\theta$                               | $\chi$   | $\Omega^2 =$   | CASE |
|--|--|--|------|
| $\omega_B^2 \gg \omega_0^2$              | $ \chi  \ll \left(\frac{\omega_r^2}{2}\right)^2$                         | $\omega_r^2, -\frac{\chi}{\omega_r^2}$                           | 1A   |
|  | $ \chi  \gg \left(\frac{\omega_r^2}{2}\right)^2$                         | $\pm \chi^{1/2}$   | 2A   |
| $\omega_0^2 \gg \omega_B^2 \gg \epsilon$ | $ \chi  \ll \left(\frac{\omega_r \omega_B}{2}\right)^2$                  | $\omega_B^2, -\frac{\chi}{\omega_r^2}$                           | 1B   |
|  | $ \chi  \gg \left(\frac{\omega_r \omega_B}{2}\right)^2$                  | $\pm \left(\chi \frac{\omega_B^2}{\omega_r^2}\right)^{1/2}$      | 2B   |
| $\epsilon \gg \omega_B^2$                | $ \chi  \ll \left(\frac{\epsilon}{2} \frac{\omega_r}{\omega_B}\right)^2$ | $\epsilon, -\frac{\chi}{\epsilon} \frac{\omega_B^2}{\omega_r^2}$ | 1C   |
|  | $ \chi  \gg \left(\frac{\epsilon}{2} \frac{\omega_r}{\omega_B}\right)^2$ | $\pm \left(\chi \frac{\omega_B^2}{\omega_r^2}\right)^{1/2}$      | 2C   |

Eq. (63) is similar to the strong magnetic field expression, Eq. (58), but with a correction term in the denominator. When the denominator is positive, Eq. (63) predicts instability above the transition energy ( $\omega_z^2 > 0$ ) and stability below. Note, however, that further below the transition energy the second term in the square root in Eq. (62) may dominate the first, i. e.,

$$-\frac{x\omega_z^2}{B_\theta^2/\gamma^2} > \left(\frac{\epsilon}{2}\right)^2 \left(1 - \frac{x/\epsilon}{B_\theta^2/\gamma^2}\right)^2 \quad (64)$$

causing the two unstable modes often found numerically at low energies (Refs. 6, 7, 9, 10). A large enough magnetic field eliminates the instability there.

$$B_\theta > \gamma_{tr}^2 \omega_0 \quad (65)$$

Incidentally, such a small toroidal magnetic field that the denominator of Eq. (63) becomes negative causes the root described by this equation to be stable above the transition energy but unstable below. The other root in Eq. (62) is unstable throughout.

### C. Numerical Solutions of the Linear Dispersion Relation

A computer program, BTRSQ, has been written to evaluate numerically the roots of the dispersion relation. Sums appearing in Eq. (13) are performed over the first twenty to forty axial and radial eigenvalues and generally converge rapidly. Good accuracy for  $\omega_z^2$  and  $\omega_r^2$ , however, is achieved for a moderate number of terms only when the numbers of axial and radial eigenvalues used are approximate integer multiples of twice the cavity-to-beam ratios of the axial and radial cross sectional dimensions,

respectively. The roots themselves of the dispersion relation are determined by Muller's method.<sup>19</sup> Typically, five seconds of CDC-7600 computer time is needed to initialize an equilibrium configuration, after which roots can be obtained at the rate of about one per second.

Calculations were, for the most part, performed using the equilibrium parameters listed in Table 2 and toroidal mode numbers in the range one to forty. The parameters were chosen to bracket those of the modified betatron under development at the Naval Research Laboratory.<sup>20</sup>

Preliminary insight can be developed by observing the scaling with beam and cavity dimensions and with toroidal mode number  $\ell$  of the geometrical factors  $g_1$  through  $g_5$  introduced by Eqs. (37) - (40). For simplicity, we eliminate  $\omega$  from the sums in Eqs. (14) - (17), replacing it by  $\lambda/R$  in the denominators and by  $\ell\omega_0$  in the numerators of the terms in the sums. The resulting expressions for  $g_3$ ,  $g_4$ , and  $g_5$  are approximately independent of beam energy, and the energy dependence of  $g_1$  and  $g_2$  can be made explicit as

$$g_1 = \gamma^2 \left( g_1^a - g_1^b v_\theta^2 \right) \quad (66)$$

$$g_2 = \gamma^2 \left( g_2^a - g_2^b v_\theta^2 \right) \quad (67)$$

Note that in deriving Eq. (67) we have dropped an extremely small term proportional to  $E_r^2$ , because it is inconsistent with the scaling shown.

Table 3 lists geometrical factors for a range of  $\ell$  values, based on the configuration in Table 2. Their magnitudes are approximately as expected, namely unity in the first four columns, and Eq. (42), here 3.72, in the last three columns. More importantly, relative differences among related factors are small. The few percent difference between  $g_1^a$  and  $g_1^b$ , for instance, indicates that  $g_1$  is essentially independent of  $\gamma$  for  $\gamma < 10$ . At much higher energies  $g_1$  increases as  $\gamma^2$ , but at such energies

TABLE 2. Typical betatron parameters used in numerical solutions of the dispersion relation, Eq. (13).

|                                |                  |
|--------------------------------|------------------|
| Beam Current                   | 1, 10 kA         |
| Beam Energy                    | 1-30 MeV         |
| Toroidal Magnetic Field        | 0, 1, 10, 100 kG |
| Index ( $n$ )                  | 0.5              |
| Beam Inner Radius ( $w_1$ )    | 98.24 cm         |
| Beam Outer Radius ( $w_2$ )    | 101.76 cm        |
| Beam Axial Half-Width ( $b$ )  | 1.76 cm          |
| Torus Inner Radius ( $r_1$ )   | 91.2 cm          |
| Torus Outer Radius ( $r_2$ )   | 108.8 cm         |
| Torus Axial Half-Width ( $a$ ) | 8.8 cm           |

TABLE 3. Approximate geometrical factors computed for the parameters in Table 2 at various toroidal mode numbers.

| $\lambda$ | $g_1^a$ | $g_1^b$ | $g_2^a$ | $g_2^b$ | $g_3$ | $g_4$ | $g_5$ |
|-----------|---------|---------|---------|---------|-------|-------|-------|
| 1         | 1.094   | 1.090   | 1.094   | 1.093   | 3.543 | 3.538 | 3.571 |
| 5         | 1.094   | 1.090   | 1.095   | 1.093   | 3.542 | 3.539 | 3.570 |
| 10        | 1.095   | 1.090   | 1.097   | 1.091   | 3.542 | 3.541 | 3.568 |
| 15        | 1.095   | 1.089   | 1.100   | 1.089   | 3.541 | 3.545 | 3.567 |
| 20        | 1.096   | 1.088   | 1.103   | 1.084   | 3.540 | 3.551 | 3.572 |
| 25        | 1.097   | 1.086   | 1.104   | 1.075   | 3.540 | 3.559 | 3.589 |
| 30        | 1.098   | 1.084   | 1.104   | 1.062   | 3.540 | 3.570 | 3.627 |
| 35        | 1.098   | 1.080   | 1.098   | 1.041   | 3.542 | 3.586 | 3.700 |
| 40        | 1.097   | 1.075   | 1.086   | 1.009   | 3.546 | 3.607 | 3.828 |

self-fields have no effect on  $\omega_z^2$ . Likewise, the small differences between  $g_5$  and  $g_4$  justifies our earlier approximation that the term in Eq. (43) linear in  $\Omega$  usually can be ignored.

Differences between  $g_3$  and  $g_4$ , on the other hand, have a strong impact on the beam stability, because they can affect the magnitude and even the sign of  $\epsilon$  and  $x$ . At small  $\lambda$ ,  $g_3$  slightly exceeds  $g_4$ , and as a consequence negative mass growth rates fall off at high energies as  $\gamma^{-1/2}$  rather than the usually cited  $\gamma^{-3/2}$ . The difference between the two geometry factors decreases with increasing toroidal mode number, so that at  $\lambda = 11$  they are equal. At higher  $\lambda$ ,  $g_4$  exceeds  $g_3$ , stabilizing the beam at sufficiently large energies. As we shall soon see, this reprieve from the negative mass instability is short-lived. For still larger  $\lambda$  the beam encounters the large  $x$  regime indicated by the second, fourth, and sixth cases in Table 1, and the hybrid instability discussed in the preceding section occurs.

The coefficients  $g_3$  and  $g_4$  represent the electrostatic and inductive electric self-field contributions to the beam longitudinal dielectric function. Electrostatic forces always exceed inductive in a straight drift tube, if no slow-wave structure is present. Evidently, the larger inductive field in a betatron is due to curvature of the beam and cavity. Ordinarily, one would expect a dominant inductive field to cause unstable longitudinal bunching, as in a Cherenkov maser.<sup>21</sup> The reverse, however, is true of a beam particle with effectively negative mass, for which excess electrostatic fields cause instability. To corroborate this picture, we have compared the stability of beams in betatrons to that of rotating electron layers, a simpler problem. Both were immersed in very strong azimuthal guide fields to suppress negative mass effects. Inductive fields were found to dominate electrostatic in both cases at high  $\lambda$  values. Behavior of the electron layer is described more fully in Appendix A.

Table 4 illustrates the changes in the geometrical coefficients for  $\lambda = 1$  as the position of the beam centroid is varied. When the beam is near either the inner or the outer wall of the cavity,  $g_1$  is much reduced due to shorting of the axial self-field restoring forces, and  $g_2$  is correspondingly increased.

TABLE 4. Approximate  $\lambda = 1$  geometrical factors computed for the parameters in Table 2 but with the beam offset radially by various amounts.

| R(cm) | $g_1^a$ | $g_1^b$ | $g_2^a$ | $g_2^b$ | $g_3$ | $g_4$ | $g_5$ |
|-------|---------|---------|---------|---------|-------|-------|-------|
| 107   | 0.136   | 0.134   | 12.768  | 13.282  | 1.567 | 1.557 | 1.326 |
| 103   | 0.851   | 0.847   | 1.796   | 1.875   | 3.326 | 3.319 | 3.357 |
| 100   | 1.094   | 1.090   | 1.094   | 1.093   | 3.543 | 3.538 | 3.571 |
| 97    | 0.905   | 0.903   | 1.901   | 1.810   | 3.326 | 3.324 | 3.314 |
| 95.67 | 0.684   | 0.684   | 3.133   | 2.962   | 3.037 | 3.037 | 2.986 |
| 93    | 0.158   | 0.159   | 14.601  | 13.936  | 1.577 | 1.587 | 1.260 |

Hence, beam stability at low energies can be affected strongly by the centering of the beam. In addition,  $g_4$  grows relative to  $g_3$  as  $R$  is decreased. The two become equal at  $R = 95.67$  cm, and for smaller radii the inductive field dominates. This suggests that improved stability at low  $\lambda$  can be achieved for a high energy beam by placing it near the inner wall of the torus.

Figures 2-5 depict  $\lambda = 1, 10, 20$ , and  $30$  negative mass instability growth rates for  $10$  kA and  $1$  kA beams in  $1$  kG guide fields, determined directly from Eq. (13). Results for  $\lambda = 1$  and  $10$  with  $\gamma > 10$  agree well with Eq. (50). The growth rate scales linearly with  $\lambda$  and  $\sqrt{v}$ . As predicted above, the growth rates at high energies vary roughly as  $\gamma^{-1/2}$  for  $\lambda = 1$  and as  $\gamma^{-3/2}$  for  $\lambda = 10$ . Scaling of growth rates at low energies is not so clean but appears to go as  $(\lambda\sqrt{v})^{1/2}$ . Although the two unstable modes below  $\gamma_{tr}$  appear to join directly onto the one unstable mode above  $\gamma_{tr}$ , a closer examination indicates that a tiny gap exists, consistent with the discussion accompanying Eq. (63).

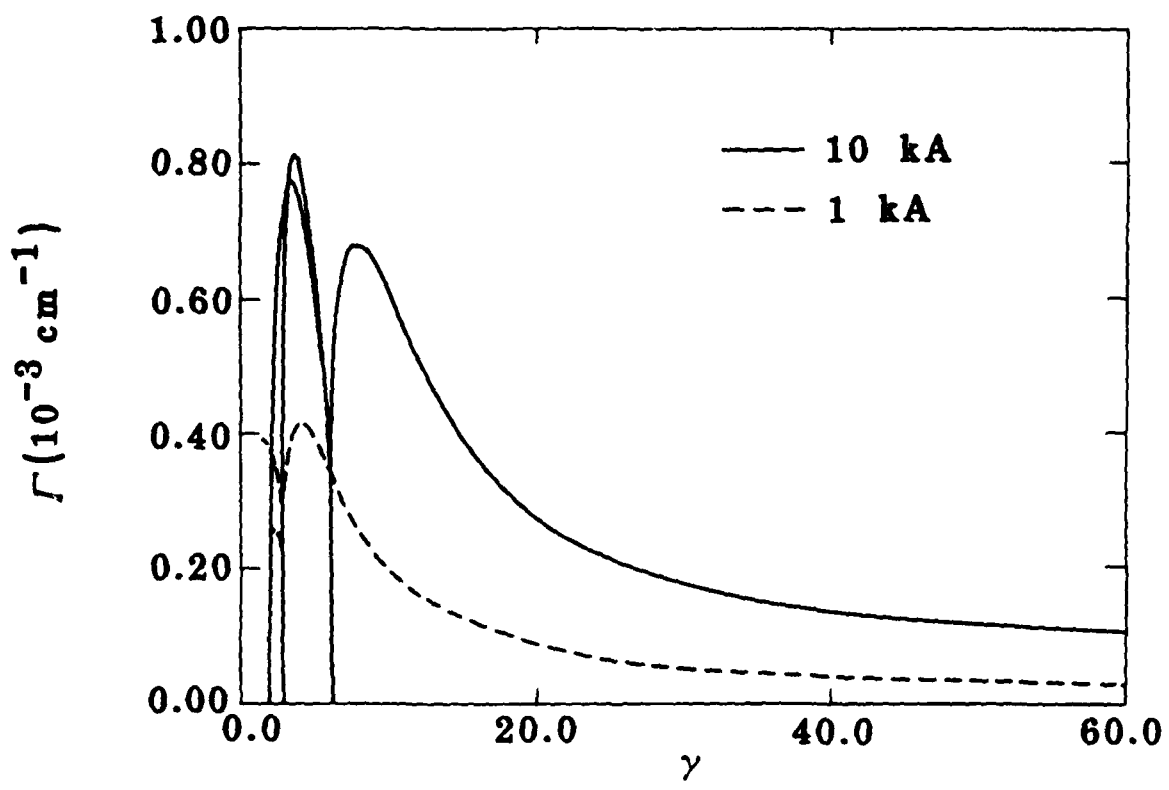


Figure 2. Growth rates of the  $l = 1$  negative mass instability versus energy for 10 kA and 1 kA beams in 1 kG guide fields.

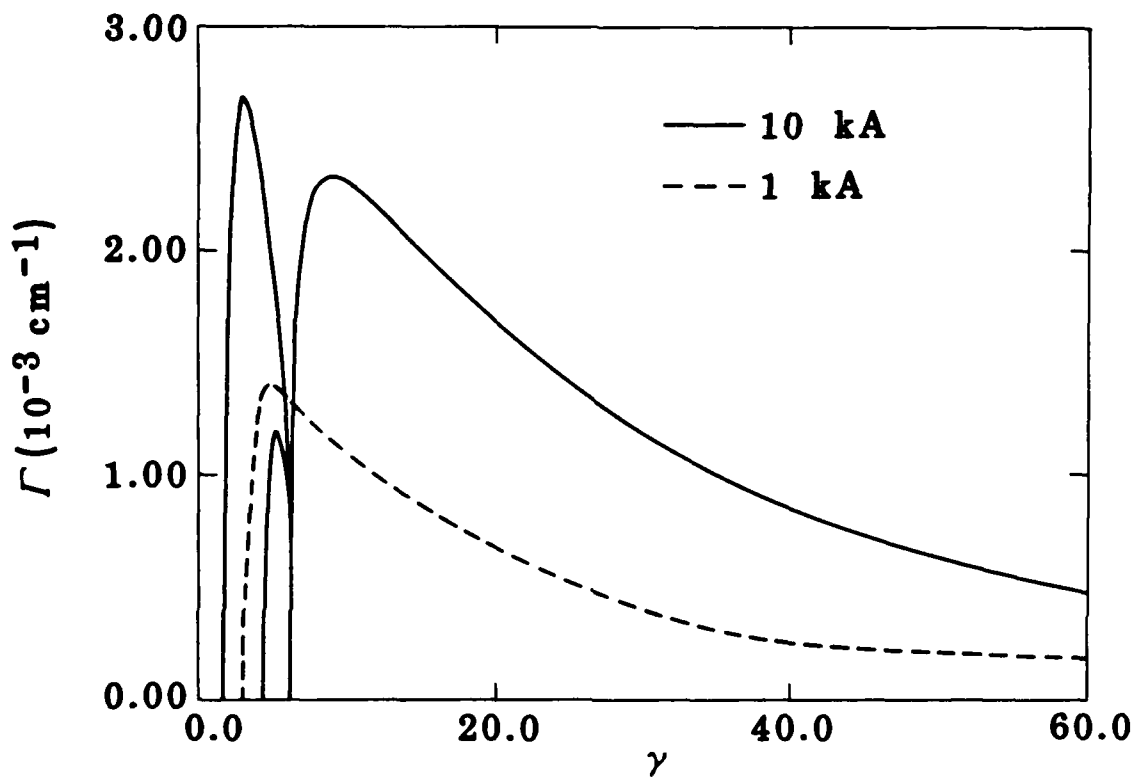


Figure 3. Growth rates of the  $\ell = 10$  negative mass instability versus energy for 10 kA and 1 kA beams in 1 kG guide fields.

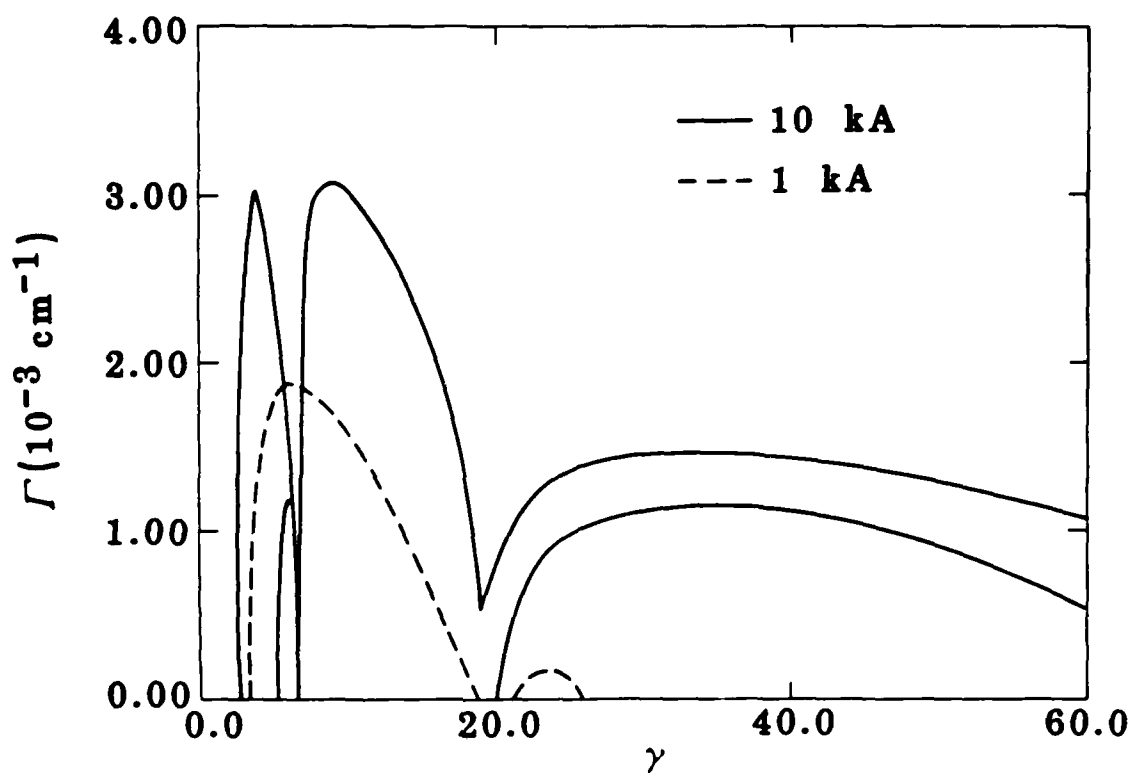


Figure 4. Growth rates of the  $\lambda = 20$  negative mass instability versus energy for 10 kA and 1 kA beams in 1 kG guide fields.

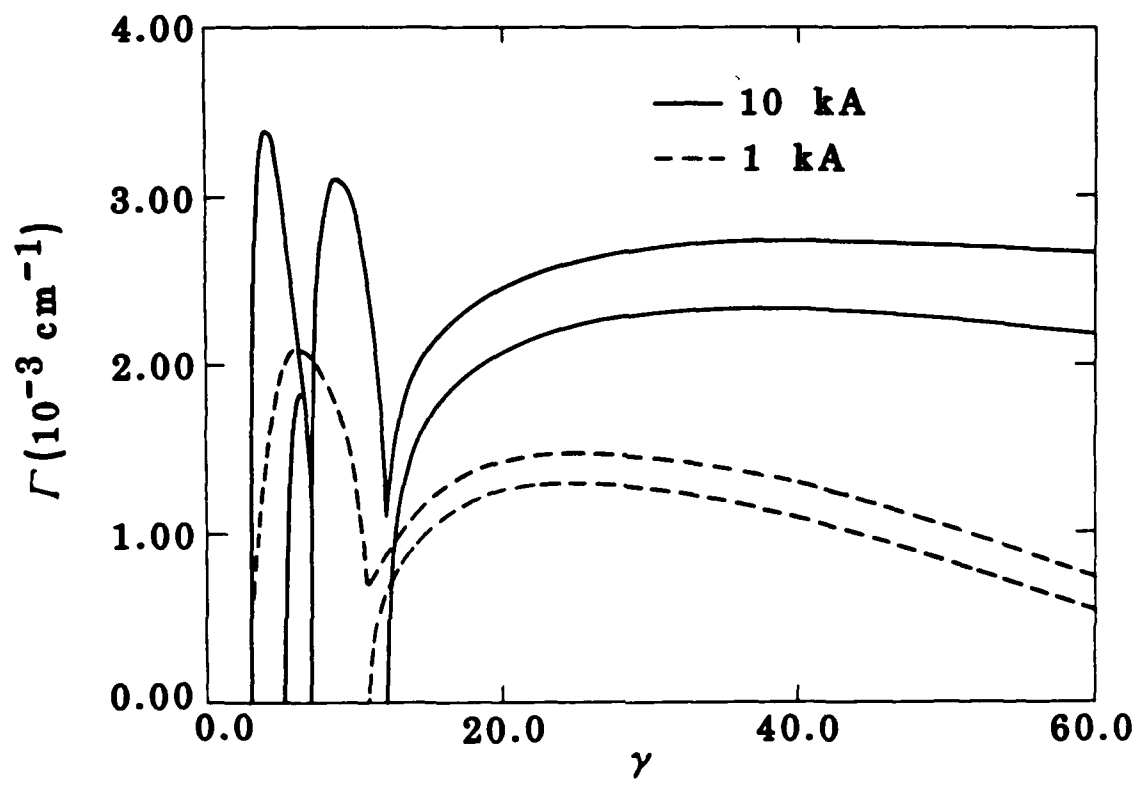


Figure 5. Growth rates of the  $\ell = 30$  negative mass instability versus energy for 10 kA and 1 kA beams in 1 kG guide fields.

When  $\lambda > 11$  the standard negative mass instability is cut off by inductive effects for  $\chi$  negative, i. e.,  $\gamma$  greater than

$$\gamma_{co} \approx \left(1 - g_3/g_4\right)^{-1/2} \quad (68)$$

The cutoff shown for the 1 kA beam at  $\lambda = 20$  in Fig. 4 satisfies Eq. (68) well. Note also the first appearance of the hybrid negative mass instability in a narrow band around  $\gamma = 24$ . The hybrid mode is much stronger in the 10 kA beam and merges directly into the usual branch of the instability at  $\gamma_{co}$ . The growth rates are described accurately by Eq. (54), but not yet by Eq. (60) because  $\chi$  is not sufficiently large. In Fig. 5 for  $\lambda = 30$ ,  $\gamma_{co} \approx 12$ ; the hybrid negative mass instability is well developed for both 10 kA and 1 kA.

Figure 6 is intended to illustrate the mode couplings that give rise to the different branches of the negative mass instability. It presents the Doppler-shifted real frequencies  $\Omega$  corresponding to the growth rates of the 10 kA beam in Fig. 4. Below  $\gamma_{tr}$  and above  $\gamma_{co}$  the longitudinal and transverse modes are strongly coupled, and two unstable branches with comparable growth rates typically exist. The standard negative mass instability occurs within the intervening energy range, resulting from a non-resonant distortion of the longitudinal modes by curvature effects.

Instability growth rate scaling with  $B_\theta$  is depicted in Fig. 7 and 8 for the 10 kA beam at  $\lambda = 1$  and 20. Results for 1 kG, 10 kG, and 100 kG guide fields are shown. Corresponding data for the conventional betatron are not given for  $\lambda = 1$ , and for  $\lambda = 20$  below  $\gamma_{co}$ , because they are indistinguishable from the 1 kG results at energies for which an equilibrium exists (above about 13 MeV). The conventional betatron is stable above  $\gamma_{co}$  for  $\lambda = 20$ , because inequality (48) is not yet strongly reversed. In general, we expect the guide field to have negligible influence on beam stability for low  $\lambda$  (e. g., Fig. 7) so long as Eq. (57) is

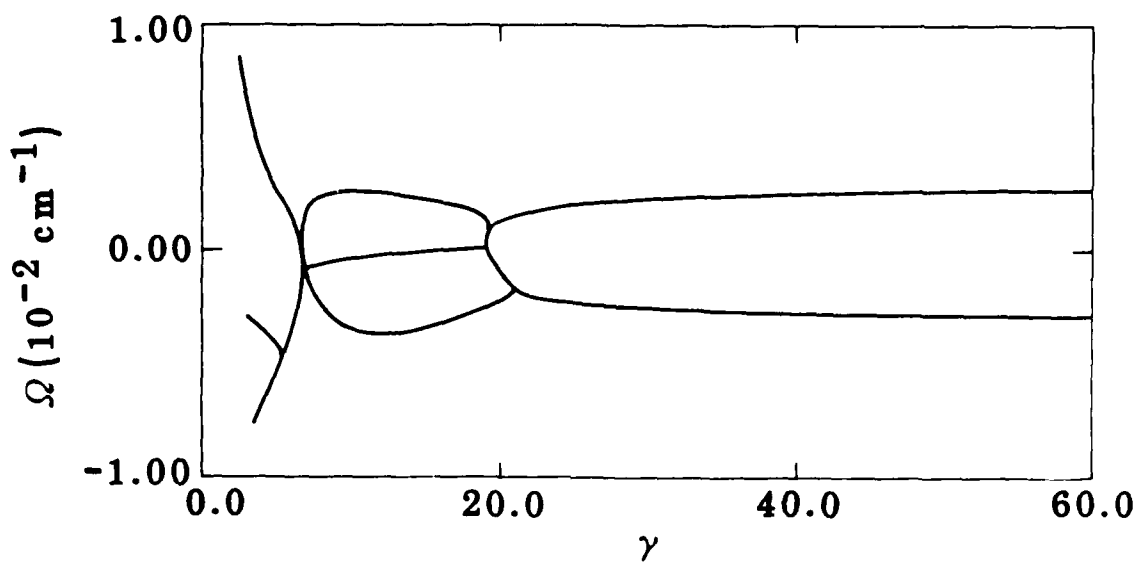


Figure 6. Doppler-shifted frequencies  $\Omega$  of the modes associated with the  $\gamma = 20$  negative mass instability of a 10 kA beam in a 1 kG guide field (Fig. 4).

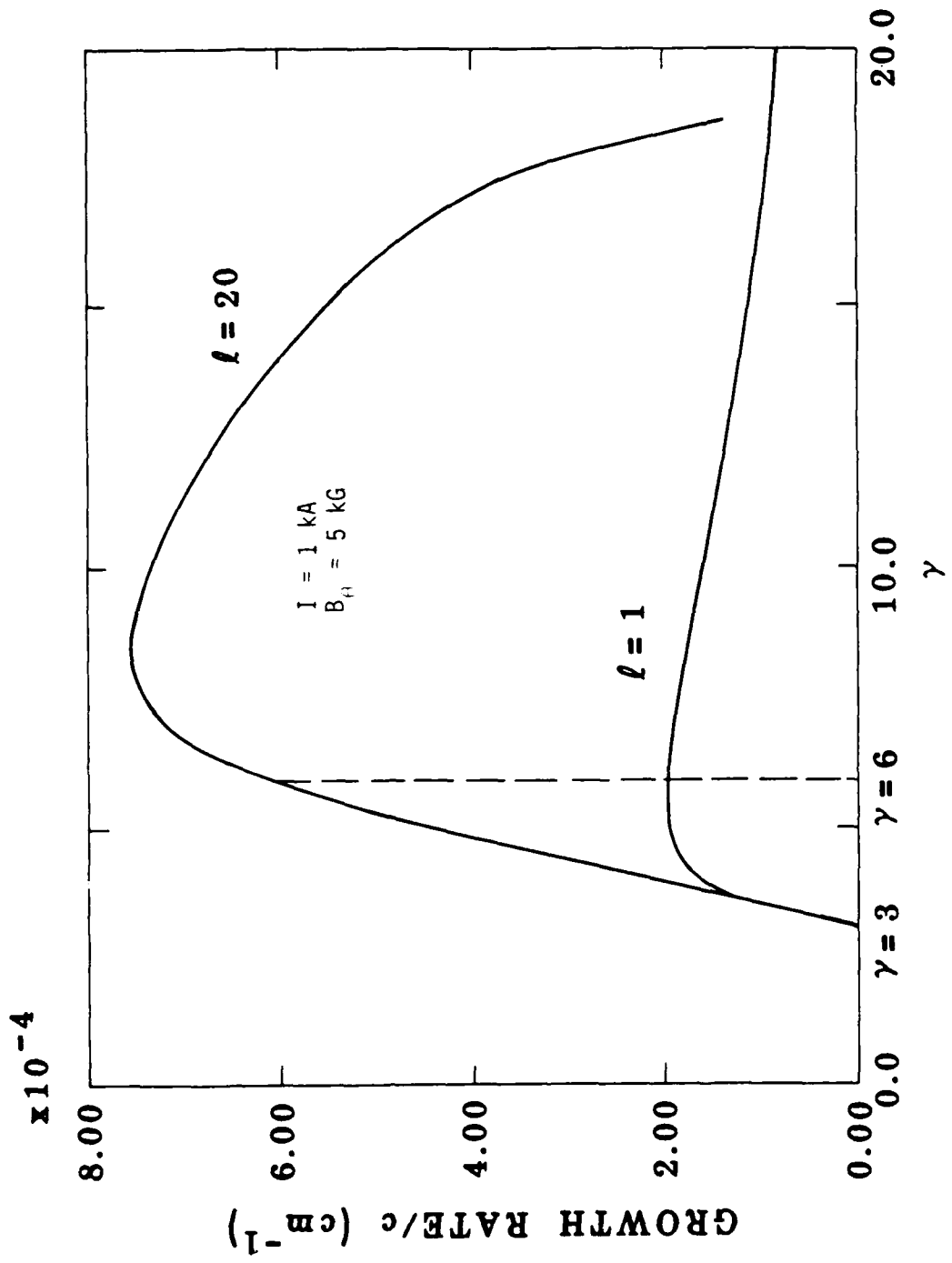


Figure 14. Cold beam growth rates of negative mass instability on a 1 kA beam versus beam energy.

It is important to note that the upper bound on the frequency spread given by case (a) applies regardless of the type of equilibrium with which one is dealing. There are various ways of trying to achieve this upper bound. One way, as we have just pointed out, is to have a Finn-Manheimer equilibrium with sufficiently small  $\omega_{pr}$ . Alternatively, one can use the RSL configuration, which as we shall see in Chap. VII, gives a beam which has maximum frequency spread at all energies. Finally, one may introduce an energy spread on the beam.<sup>5,9</sup> However, self-consistent modified betatron equilibria which include an energy spread have not been adequately studied to date. Limited simulations<sup>7</sup> indicate that it may be difficult to achieve an equilibrium whose radius is determined by energy spread rather than by betatron oscillations. Analytic calculations of beam stability in the presence of an energy spread generally assume that the beam radius is determined solely by the energy spread.<sup>5</sup> This is a very optimistic assumption.

We now look at some IVORY simulations which illustrate the effect of frequency spread on beam stability. For all the examples considered,  $\Delta_0 \approx 8 \times 10^{-5} \text{ cm}^{-1}$ , since  $a = 2 \text{ cm}$ ,  $R = 100 \text{ cm}$ . First, we look at a 1 kA beam at  $\gamma = 6$  in a 5 kG toroidal field, other parameters being given in Table 5. The diamagnetic-paramagnetic transition for this beam occurs approximately at  $\gamma = 8$ . We simulated the  $\lambda = 20$  mode on this beam using IVORY. The cold-beam growth rate for this mode, from Fig. 14, is  $6 \times 10^{-4} \text{ cm}^{-1}$ , while the simulation growth was much smaller, at  $\leq 1 \times 10^{-5} \text{ cm}^{-1}$ . From a computer movie of the simulation, the poloidal rotation frequency was measured to be  $5 \times 10^{-4} \text{ cm}^{-1}$ , which is significantly smaller than  $\lambda\Delta_0 \approx 1.6 \times 10^{-3} \text{ cm}^{-1}$ . One would therefore expect case a) above to apply, so that the growth rate is reduced by the amount  $\lambda\Delta_0$ , which is more than enough to stabilize the mode, as observed. The  $\lambda = 1$  mode on this beam is predicted to be unstable, however. The cold beam growth rate from Fig. 14 is  $1.8 \times 10^{-4} \text{ cm}^{-1}$ , which is greater than  $\Delta_0$ . We have not verified with IVORY that the beam is, in fact, unstable, because the code would have to be run a rather long time to give a good estimate of the small expected growth rate,  $1.0 \times 10^{-4} \text{ cm}^{-1}$ . As an aside which is relevant to experimental efforts going on at NRL and elsewhere, we note from Fig. 14 that the growth rates

rate of the instability on this beam is accurately given by the cold-beam growth rate, as we shall see below.) In Fig. 13(c),  $\gamma = 20$ , so that the beam is near the transition, and therefore is rotating more slowly. In this case, we see that the spreading-out of the bunches in the toroidal direction is much larger. This figure shows clearly that the spreading-out occurs because particles at smaller radius, with a shorter distance to travel, move ahead relative to those at larger radius.

Let us now proceed with the calculation of an effective value of  $\Delta$  for the two cases mentioned. For case a), a particle at radius  $r = R + \delta r$  has circulation frequency  $\Omega = \omega_0(1+\delta r/R)$ . Assuming that the beam has uniform density profile, the distribution of frequencies is then  $f_b \propto ((\Omega - \omega_0)^2 - \omega_0^2 a^2/R^2)^{1/2}$ , where  $a$  is the beam radius. Unlike  $f_L$  above, this distribution has a sharp cutoff, resulting from the finite extent of the beam. Nevertheless, we can compute an effective  $\Delta$  for the beam by, for example, demanding that the half-widths of the cumulative distributions be the same for  $f_L$  and  $f_b$ . In physical space, this means that one is specifying a radial interval  $R - \delta r_{1/2}$  to  $R + \delta r_{1/2}$  and requiring that half the beam particles be within this band. This criterion leads to the relation  $\Delta \approx 0.4\omega_0 a/R \equiv \Delta_0$ . If one applies a similar criterion to compute an effective width for case b), one finds that the cumulative distribution corresponding to the Lorentzian is divergent, i.e., a finite beam width cannot be defined for  $f_L$ . We will not dwell on this difficulty here but simply note that for those simulations we have performed where case b) applies, the frequency spread present has a negligible effect on the growth rate. Presumably the effect of the small frequency spread would become important only at  $\lambda$  values significantly higher than those we have considered to date (viz.  $\lambda = 1-20$ ).

For the Finn-Manheimer equilibria, the beam has some poloidal rotation unless one is right at the transition energy. It is therefore reasonable to ask how we decide whether a particular simulation run falls under case (a) or case (b) above. It is easy to show that if  $\lambda\Delta_0 > \omega_{pr}$  where  $\omega_{pr}$  is the poloidal rotation frequency, and  $\lambda$  is the mode number we are simulating, then the beam falls under case (a). In the opposite limit, case (b) applies.

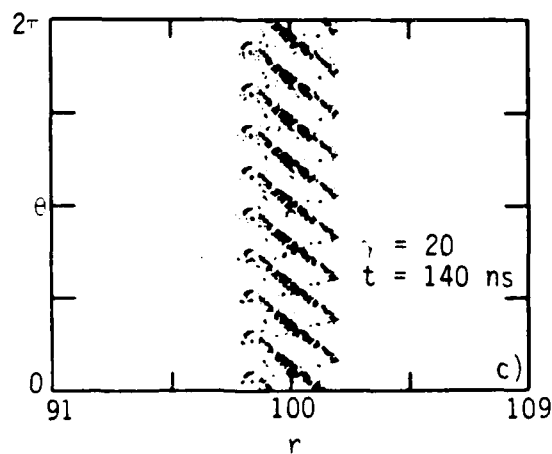
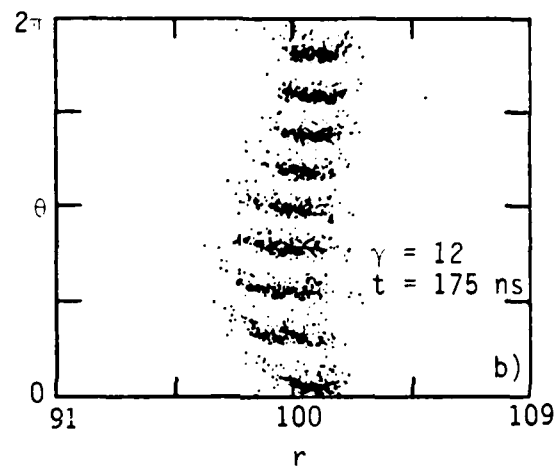
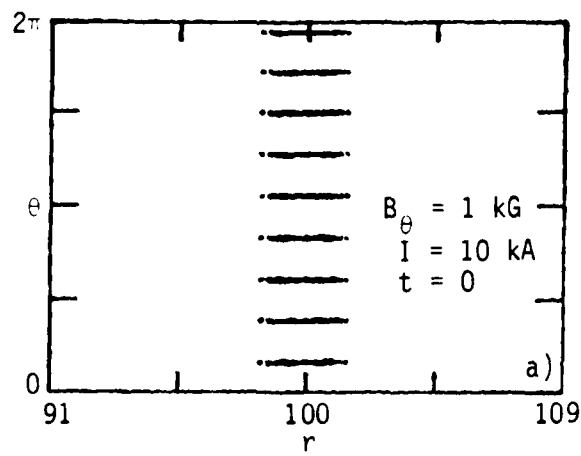


Figure 13. Illustration of dependence of toroidal rotation frequency-spread on beam energy. Initial particle positions are shown in (a). The beam in (c) is close to the transition energy  $\gamma_T = 18$ , so the toroidal mixing is faster than in (b).

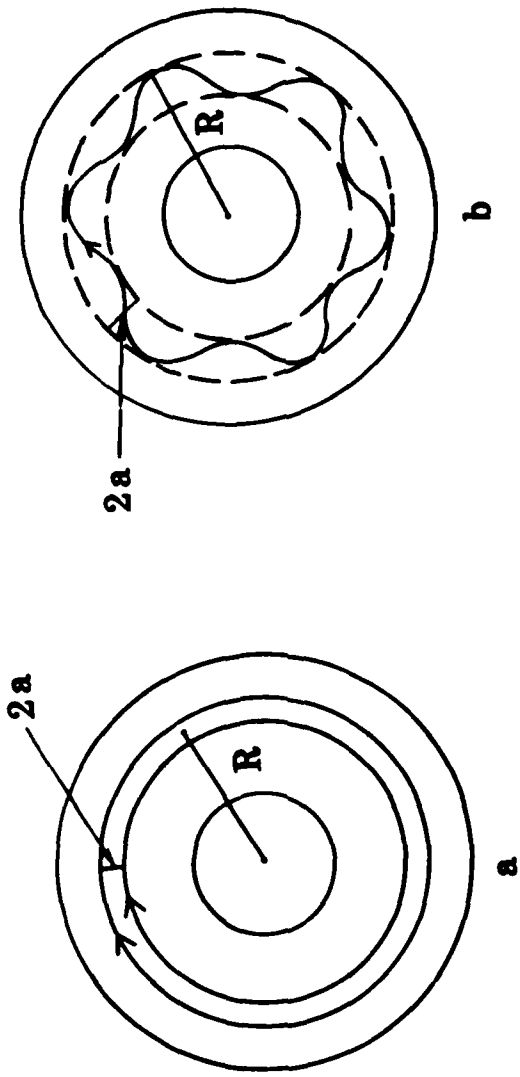


Figure 12. In (a) particles have no transverse motion while in (b) particles oscillate about the beam center.

### III. UPPER BOUNDS ON STABLE CURRENTS IN THE MODIFIED BETATRON

In the analytic model of Chap. II, all particles have the same circulation frequency about the major axis since the beam is assumed to be made up of rigid disks. One would expect a spread in circulation frequencies of the particles to lead to a reduction in growth rates through Landau damping.<sup>5,9</sup> If one assumes that the frequency distribution is Lorentzian,  $f_L(\Omega) \propto 1/((\Omega - \omega_0)^2 + \Delta^2)$ , where  $\omega_0$  is the average (matched) circulation frequency, and  $\Delta$  is a constant, then a simple calculation<sup>5</sup> shows that the growth rate of an instability with toroidal mode-number  $\lambda$  should be reduced by  $\lambda\Delta$ . A Lorentzian is a somewhat unrealistic distribution, having long tails, but more realistic distributions are much more difficult to treat analytically. The Lorentzian is, therefore, used to give rough estimates. We now look at how one can make a reasonable choice of the value of  $\Delta$  for the types of equilibria we have been simulating with IVORY. Since we are concerned for the most part with relativistic beams, all the particles have about the same speed. A spread in circulation frequencies can therefore result only from a spread in path lengths of the particles. Consider the cases shown in Fig. 12, where in a) the particles have no transverse motion and in b) they oscillate about the centroid of the beam. For case a) the spread in circulation frequencies is clearly first order in  $a/R$ , while for b) the averaging over major radius leads to a spread of order  $(a/R)^2$ . For the Finn-Manheimer type of equilibrium,<sup>23</sup> which is the equilibrium we have predominantly used in IVORY, the beam behaves as in case b) except near the diamagnetic-paramagnetic transition, where poloidal rotation ceases. The contrast between these two cases can be seen from the IVORY simulation results in Fig. 13. In Fig. 13 (b) and (c), all parameters are the same except for the energy. The diamagnetic-paramagnetic transition energy<sup>23</sup> for the beam is  $\gamma = 18$ . In the simulations, the frequency spread of the particles shows up as the spreading out of particle bunches in the toroidal direction, starting from the initial positions shown in Fig. 13 (a). The faster the bunches spread out, the higher the circulation frequency spread. For Fig. 13(b),  $\gamma = 12$ , so that the beam is far from the transition, and the poloidal rotation leads to the small  $O(a/R)^2$  frequency spread seen in the figure. (Not surprisingly, the growth

be proven, of course.) Thin dielectric linings or weak slow-wave structures in the cavity<sup>16,17</sup> should have similar effects but must not significantly decrease the electromagnetic cutoff frequency. Although reducing growth for low toroidal modes tends to increase it for high modes, beam temperature is expected to control the latter. Implementing any of these ideas does pose serious technical problems, however. Far off-center beams may quickly strike the wall, dielectrics outgas and flash over, and slow-wave structures are easily damaged by high power beams. Nonetheless, additional thought given to such speculative approaches may prove fruitful.

Our theoretical model of negative mass instabilities can be extended in at least three attractive directions. Properly treating periodic, strong focusing devices, including the stellatron and alternating-solenoid betatron, involves coupling different toroidal modes through the particle equations of motion. This has already been done for beam-breakup instabilities in a racetrack induction accelerator,<sup>22</sup> and applying similar methods to the present model should not prove difficult. Secondly, solving the field equations by boundary integrals over Green's functions rather than by fitting the Green's functions to the boundary, as done here, may allow us to accommodate more general geometries. Also, the massive cancellations observed numerically in several terms of the dispersion relation perhaps could be performed analytically within an integral formulation. Adding temperature effects to the model is the third, and most difficult, extension. Whether the advantages to be gained by replacing the existing useful but ad hoc methods for estimating stabilization due to temperature by a more nearly self-consistent description justifies the effort entailed is uncertain.

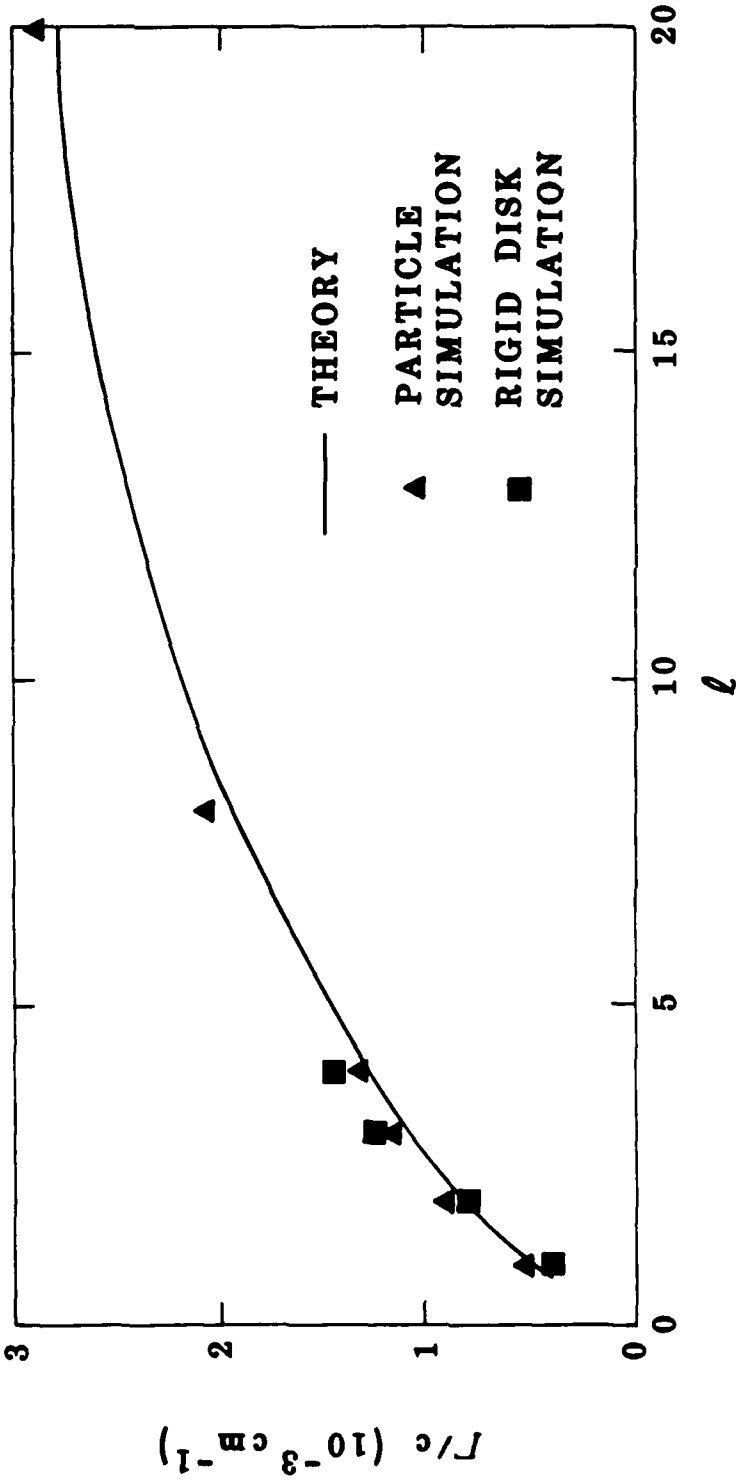


Figure 11. Negative mass growth rates at various  $\xi$  values for a 10 kA beam in a 1 kg guide field determined from IVORY simulations compared to dispersion relation results. Some simulations employed rigid disks instead of discrete particles.

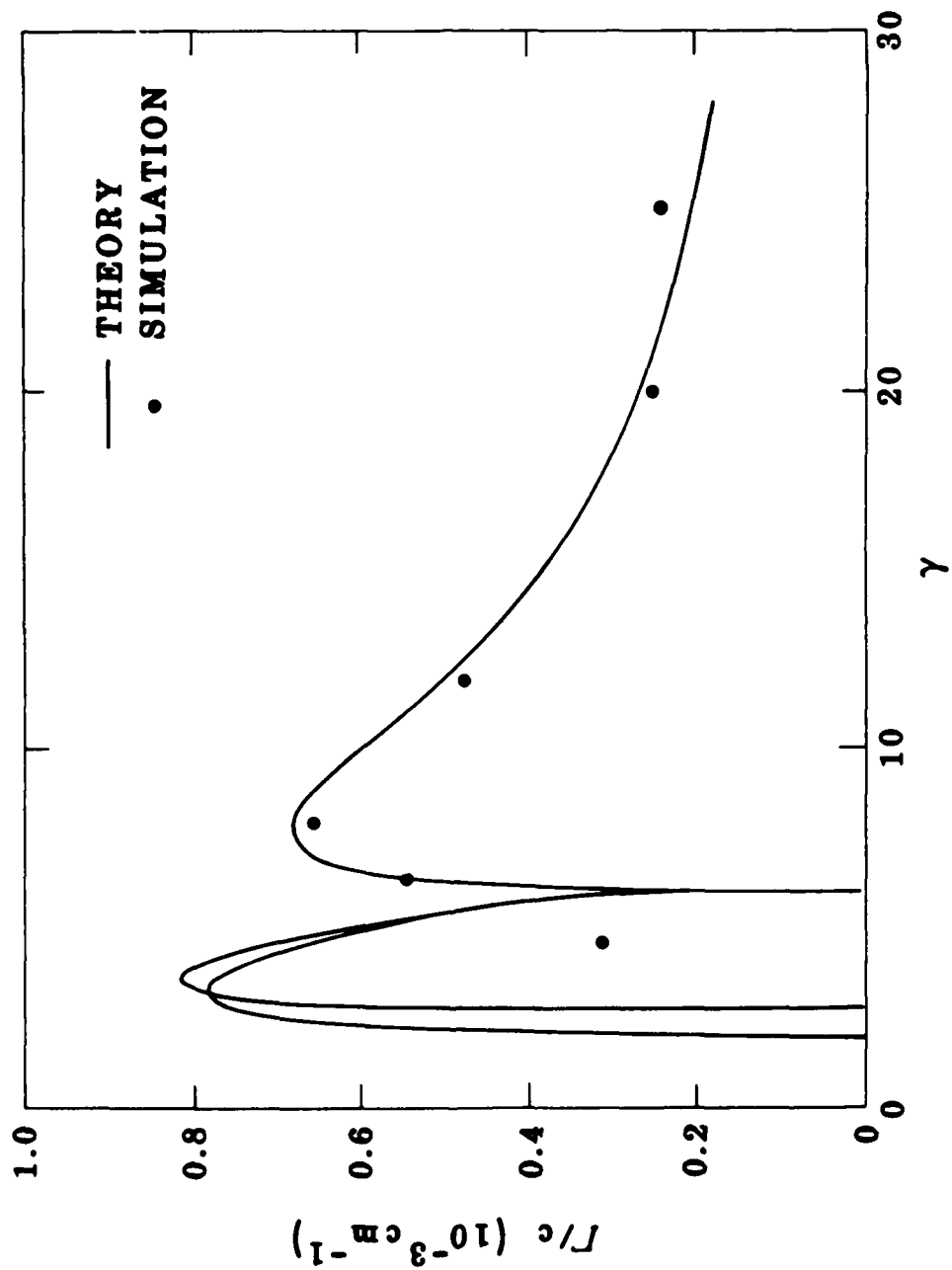


Figure 10. Negative mass  $\lambda = 1$  growth rates for a 10 kA beam in a 1 kg guide field determined from IVORY simulations compared to dispersion relation results.

We conclude this Section with a brief comparison of dispersion relation curves with growth rates determined by the computer simulation code IVORY. The simulation data points were, for the most part, already reported in Ref. 6 and 7. Figure 10 gives results for  $\lambda = 1$  for a 10 kA beam in a 1 kG guide field. Agreement is excellent except for the  $\gamma = 5$  data point. The discrepancy probably is due to beam temperature in the simulation. Figure 11 treats the same beam but with  $\gamma$  held fixed at 12 and  $\lambda$  varied from 1 to 20. Again, agreement between theory and simulation is excellent. The few simulations performed with rigid disks instead of discrete particles further vindicate the rigid disk approximation made in our model.

#### D. Summary and Discussion

We have developed an improved rigid disk model for high current, low temperature beams in conventional and modified betatrons. The resulting dispersion relation, although quite complicated, has been solved analytically in several useful limiting cases and numerically over a wide range of parameters. A novel result of this work is the dominance of inductive over electrostatic fields at high toroidal mode numbers, which stabilizes the negative mass effect at high energies for some toroidal modes and couples with it for other toroidal modes to give a hybrid instability of reduced growth rate. The limited utility of a toroidal magnetic field for slowing instability growth also is noteworthy. Model predictions agree well with most available simulation data, but additional comparisons are desirable.

Several possible techniques based on inductive coupling between the beam and the accelerator cavity suggest themselves for reducing or eliminating the negative mass instability at low toroidal mode numbers and moderate to high beam energies. We have already seen that positioning the beam near the inner wall of the torus kills the  $\lambda = 1$  negative mass instability of a 10 kA beam above 16 MeV. (That this result for a far off-center beam carries over to beams and cavities with circular cross sections remains to

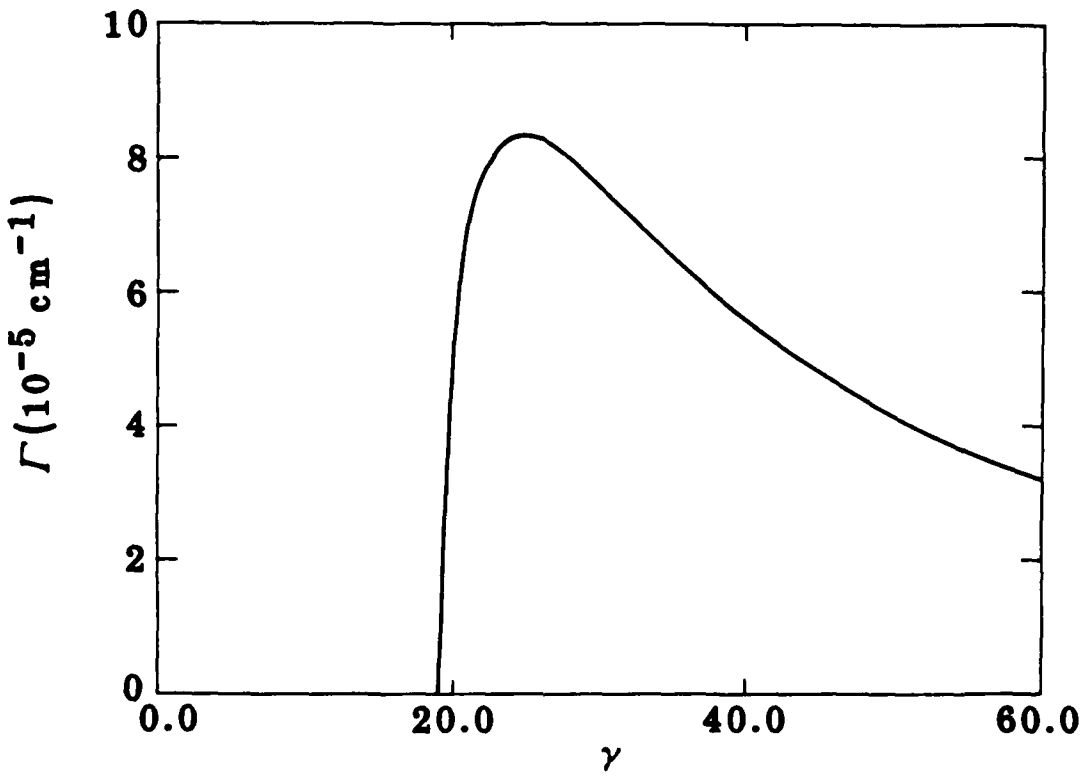


Figure 9. Growth rate of the  $\lambda = 20$  inductive instability versus energy of a 10 kA beam in an infinite guide field.

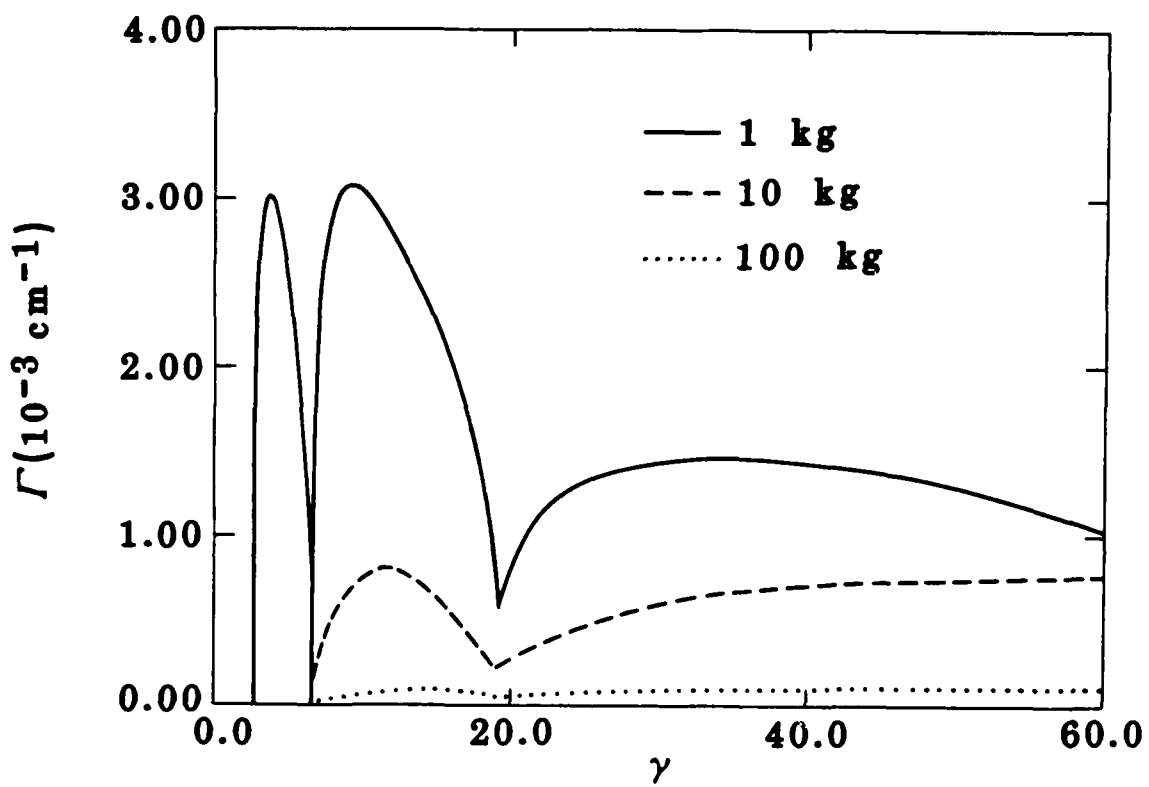


Figure 8. Growth rates of the  $\lambda = 20$  negative mass instability versus energy for 10 kA beams in 1kG, 10 kG, and 100 kG guide fields.

satisfied. For the present parameters this is true for  $B_\theta$  less than a few kG at  $\gamma = 10$  and a few thousand kG at  $\gamma = 50$ . Hence, we see a steady drop in the peak of the growth rate curve as  $B_\theta$  is increased above 1 kG until it obeys Eq. (59) at 100 kG. Note that growth below  $\gamma_{tr}$  also is eliminated. In contrast, growth rates at the highest energies shown in the plot are little reduced.

Below  $\gamma_{co}$  instability behavior at  $\lambda = 20$ , displayed in Fig. 8, is qualitatively similar to that at  $\lambda = 1$ . Growth rates above the inductive transition energy are expected, based on Table 1, to fall off with magnetic field as  $B_\theta^{-1/2}$  once  $B_\theta$  somewhat exceeds  $\omega_0$ . This happens above a few kG for energies of interest in Fig. 8. At very high guide fields, probably several thousand kG, the negative mass instability ought to be eliminated, leaving the inductive instability mentioned earlier in this Section. Figure 9 gives the growth rate at infinite field strength, for which Eq. (13) collapses to

$$\Omega^2 = \epsilon \quad (69)$$

The instability sets in abruptly at  $\gamma_{co}$ . Growth scales as  $\lambda/R$  and, for high energies,  $(v/\gamma^3)^{1/2}$ . As a test of our work, we also solved the dispersion relation in Appendix A with  $k = \pi/b$  and obtained remarkably similar curves.

Parameters differing from those in Table 2 were run in a few instances. A 10 kA beam in a 1 kG guide field at  $\lambda = 1$  and 20 was considered. Changing the vertical field index  $n$  from 0.5 to 0.25 or 0.75 modified the overall magnitudes of growth rates by no more than 20%, although details were somewhat different at low energies. Likewise, increasing or decreasing the beam dimensions by a factor of two caused no differences not accountable in terms of a rescaling of  $g_3$ ,  $g_4$ , and  $g_5$ . Small changes in  $R$  also had negligible effects. Moving the beam all the way to the inner wall, on the other hand, eliminated all  $\lambda = 1$  instabilities above  $\gamma = 34$  but increased growth rates by a factor of 2.5 at low energies. Growth rates at  $\lambda = 20$  were approximately doubled.

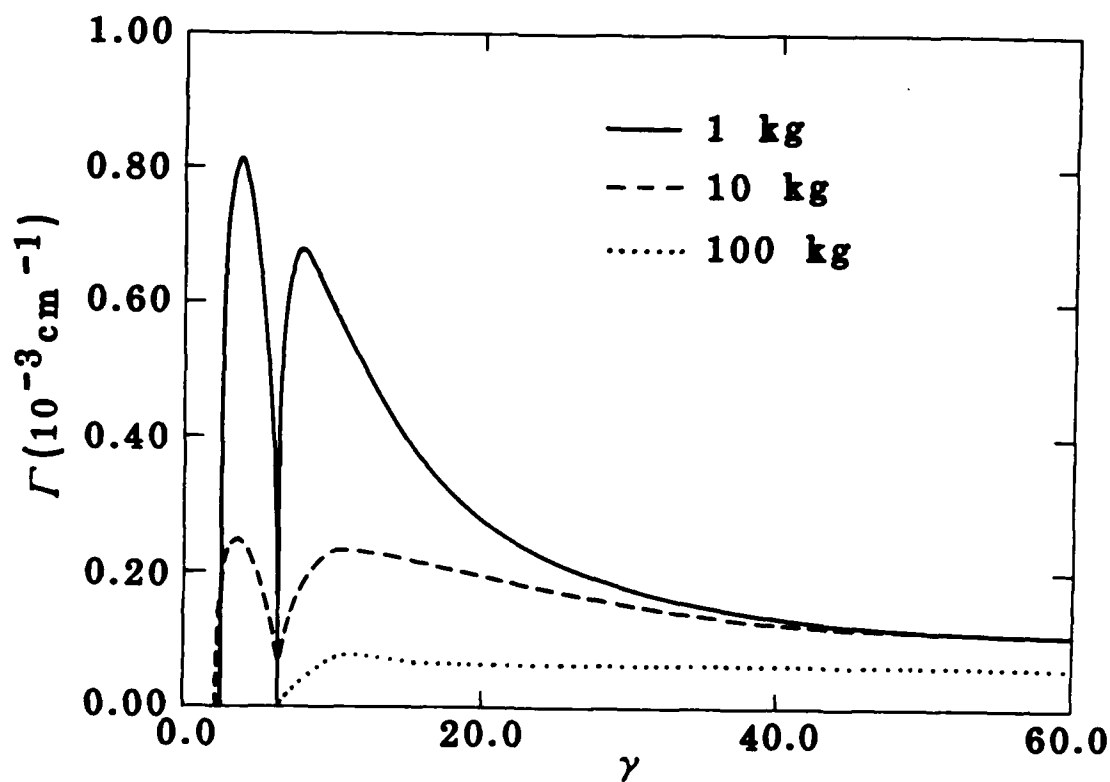


Figure 7. Growth rates of the  $\lambda = 1$  negative mass instability versus energy for 10 kA beams in 1 kG, 10 kG, and 100 kG guide fields.

for a cold beam go to zero at  $\gamma = 3$ , and there are no unstable modes below this energy. Therefore, injection experiments at 1 MeV or less, and 1 kA beam current should not encounter the negative mass instability. This assumes however, that the beam is injected in one turn with the parameters in Fig. 14. The cutoff at  $\gamma = 3$  is a function of the self-fields of the beam. At lower currents, this point moves to smaller  $\gamma$ , so that if injection takes place over many turns, the intermediate values of the current may be unstable.

TABLE 5. Modified Betatron Parameters in IVORY Simulations

|                              |            |                                    |
|------------------------------|------------|------------------------------------|
| Torus Major Radius           | R          | 1 m                                |
| Torus Minor Radius           | b          | 9 cm                               |
| Beam Radius                  | a          | 2 cm                               |
| Beam Current                 | I          | 1-10 kA                            |
| Beam Energy                  | $\gamma$   | 3-50                               |
| Toroidal Field               | $B_\theta$ | 1-5 kG                             |
| External Field Index         |            | 1/2                                |
| Upper Bound Frequency Spread | $\Delta_0$ | $8 \times 10^{-5} \text{ cm}^{-1}$ |

The second case we look at is for a 10 kA beam with  $\gamma = 12$  in a 1 kG toroidal magnetic field and with Table 5 parameters. This is the beam in Fig. 13(b) above. We simulated the  $\ell = 1$  instability, which has a predicted growth rate of  $5 \times 10^{-4} \text{ cm}^{-1}$  for a cold beam. The poloidal rotation frequency is  $\omega_{pr} = 5.7 \times 10^{-3} \text{ cm}^{-1}$ , which exceeds  $\Delta_0$ , so that the beam falls under case (b). The simulation results verify that the small frequency spread seen in Fig. 13(b), has a negligible effect on the growth rate. The simulation gives  $\Gamma = 5 \times 10^{-4} \text{ cm}^{-1}$ , the cold beam growth rate, and the beam is strongly disrupted in less than 1  $\mu\text{sec}$ .<sup>7</sup>

As a third example, we consider the beam in Fig. 13(c), with 10 kA and  $\gamma = 20$ . For this case, the poloidal rotation frequency is  $\omega_{pr} = 1.5 \times 10^{-3} \text{ cm}^{-1}$ , which is rather slower than for  $\gamma = 12$ . However, for  $\ell = 1$ , the beam still falls under case (b), since  $\Delta_0 < \omega_{pr}$ . Thus, the simulation gives  $\Gamma = 2.5 \times 10^{-4} \text{ cm}^{-1}$ , compared to the cold-beam theoretical growth rate of  $2.7 \times 10^{-4} \text{ cm}^{-1}$ . We note that even if this beam had the maximum possible

frequency spread consistent with its radius, namely  $\Delta_0 = 8 \times 10^{-5} \text{ cm}^{-1}$ , it would still be unstable. In order to make  $\Delta_0$  sufficiently large to kill the instability, the beam radius must be increased.

We briefly mention an anomalous result encountered for this last set of parameters. Since at  $\gamma = 20$  the beam is above the transition energy, no toroidal magnetic is needed to confine it. Theory indicates that for  $B_\theta = 0$ , the growth of the instability should be slightly larger than that for  $B_\theta = 1 \text{ kG}$ . However, a simulation of the  $\lambda = 1$  mode with  $B_\theta = 0$  shows a much smaller growth rate, namely  $\Gamma < 3 \times 10^{-5} \text{ cm}^{-1}$ . The amount of frequency spread seen is not sufficient to explain this stability. As can be seen by comparing Fig. 15 with Fig. 13(c), the frequency spread for  $B_\theta = 0$  is in fact significantly smaller than for  $B_\theta = 1 \text{ kG}$ . It may be that our theoretical model is inaccurate for some reason when  $B_\theta$  goes to zero. Since the present efforts in betatron research are concentrating on machines with substantial toroidal magnetic fields, we have not yet given much attention to this problem. We hope to be able to return to it in the near future. The examples we have discussed are summarized in Table 6.

TABLE 6. Summary of Examples Discussed in Text.

| I (kA) | Energy (MeV) | $\lambda$ | Stability                                |
|--------|--------------|-----------|--|
| 1      | 1            | 1         | Stable*                                  |
|        |              | 20        | Stable } $\Gamma = 0$ from Fig. 14       |
| 2.5    | 2.5          | 1         | Unstable*, Insufficient Frequency Spread |
|        |              | 20        | Stabilized By Frequency Spread           |
| 10     | 5.5          | 1         | Unstable, Insufficient Frequency Spread  |
|        |              | 9.5       | Unstable, Insufficient Frequency Spread  |

\*Analytic prediction not verified with IVORY.

The above comparisons between theory and simulations establish some credibility for our method of calculating the effective frequency spread on a beam. We can now compute upper bounds on the stable current,  $v_{\max}$ ,

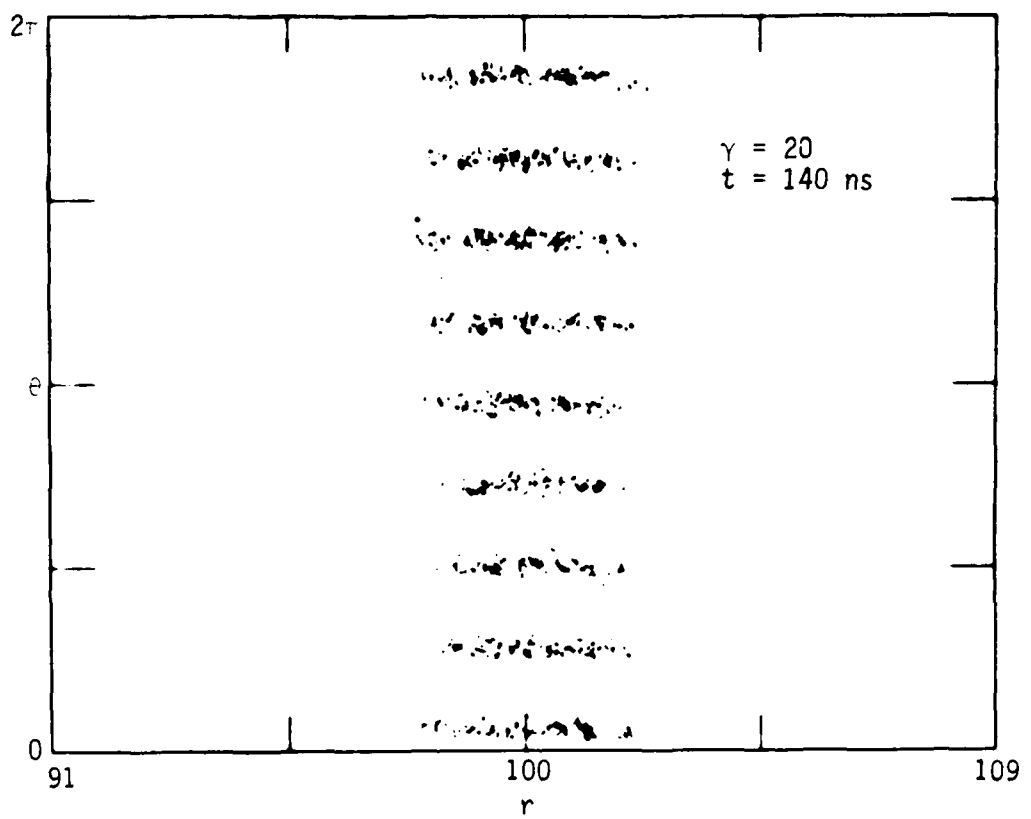


Figure 15. Particle positions after 140 ns for  $\gamma = 20$  beam in zero toroidal magnetic field. Compare with Fig. 13(c).

(current divided by 17 kA) once all the other parameters are specified. We do this by assuming that the beam has the maximum circulation spread,  $\Delta_0$ , regardless of its energy. Results are shown in Fig. 16. Note that since the growth varies as  $v^\alpha$ , where  $\alpha < 1/2$ , whereas  $\Delta_0$  varies linearly with beam radius  $a$ , a small change in radius can produce a large change in  $v_{\max}$ . Also, for small  $v_{\max}$ , the current is most limited at injection (assuming  $\gamma_{\text{inj}} = 3$ ), because, as the beam accelerates, its stability improves. For larger  $v_{\max}$ , the beam may be more unstable at energies higher than the injection energy. This leads to the crossing of the lines in Fig. 16(b). This behavior is due to the humped shape of the growth curve, and is related to the multi-valued nature of the limiting current as a function of beam energy spread found by Sprangle and Chernin.<sup>5</sup> This multi-valuedness can occur even when there is no energy spread. As an example, compare Fig. 16(b) with Fig. 14. Figure 14 shows that for  $\gamma \leq 3$ , a 1 kA beam is stable, while Fig. 16(b) claims that  $I < 100$  A is necessary for stability (assuming a 2 cm beam radius). The paradox arises from the fact that the growth-rate cutoff in Fig. 14 is a function of beam current. Thus, lower currents are unstable for  $\gamma < 3$ .

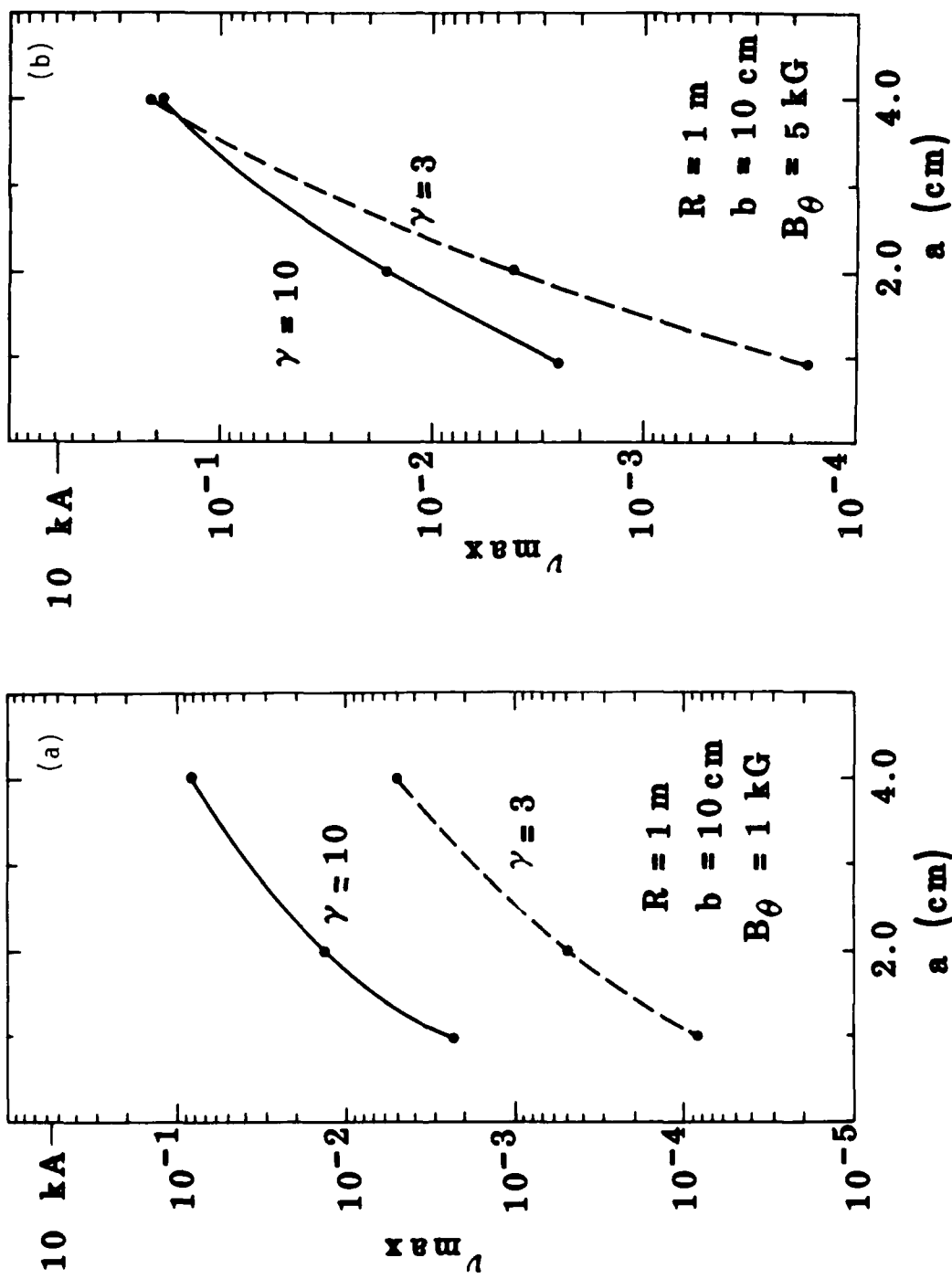


Figure 16. Upper bounds on stable currents in the modified betatron for (a) 1 kG and (b) 5 kG toroidal magnetic fields.

#### IV. STELLATRON ACCELERATOR: EQUILIBRIUM PROPERTIES

##### A. Particle Orbits In The Stellatron.

The stellatron accelerator<sup>3</sup> adds strong focusing to the modified betatron device through the use of a helical quadrupole field, as shown in Fig. 17. This results in major improvement in the tolerance of the device to mismatch between the vertical field and the beam energy [see Refs. 3, 24 and Chapter IVB]. The work we describe here arose out of some IVORY simulations of the negative mass instability in this device. It was observed that for some parameters the beam developed large envelope oscillations, with a few particles striking the wall (see Fig. 18). This was puzzling because previous results seemed to indicated that the particles should be confined for these parameters.<sup>3</sup> When we reduced the current by orders of magnitude, we found the same behavior, indicating that collective effects were not involved. We then went back to the single particle equations in the stellarator fields,<sup>3</sup> and studied the orbits they predicted both analytically and numerically. For the numerical work, we used a single particle orbit code. The details of this investigation are given in Appendix B. Here we summarize the main results.

The toroidally averaged effect of the quadrupole fields is a focusing one. At any given toroidal location, however, the field is focusing in one transverse direction and defocusing in the other. Because of this, the orbit of a particle can be quite sensitive to where it starts out. Note that the stability of the orbit is independent of the initial conditions, and so is not in question here. The effect of the initial conditions on the amplitude of the particle orbit is shown in Fig. 19. The orbits shown are limiting cases in that for one, the particle is started in the focusing plane and for the other, the particle is started in the defocusing plane.

The particle orbits can be computed analytically from the linearized single particle equations. The general orbit has the following character: in a frame which rotates as  $\exp(im\theta/2)$ , where  $m$  is the mode number of the quadrupole field, the orbit is the sum of two right ellipses whose

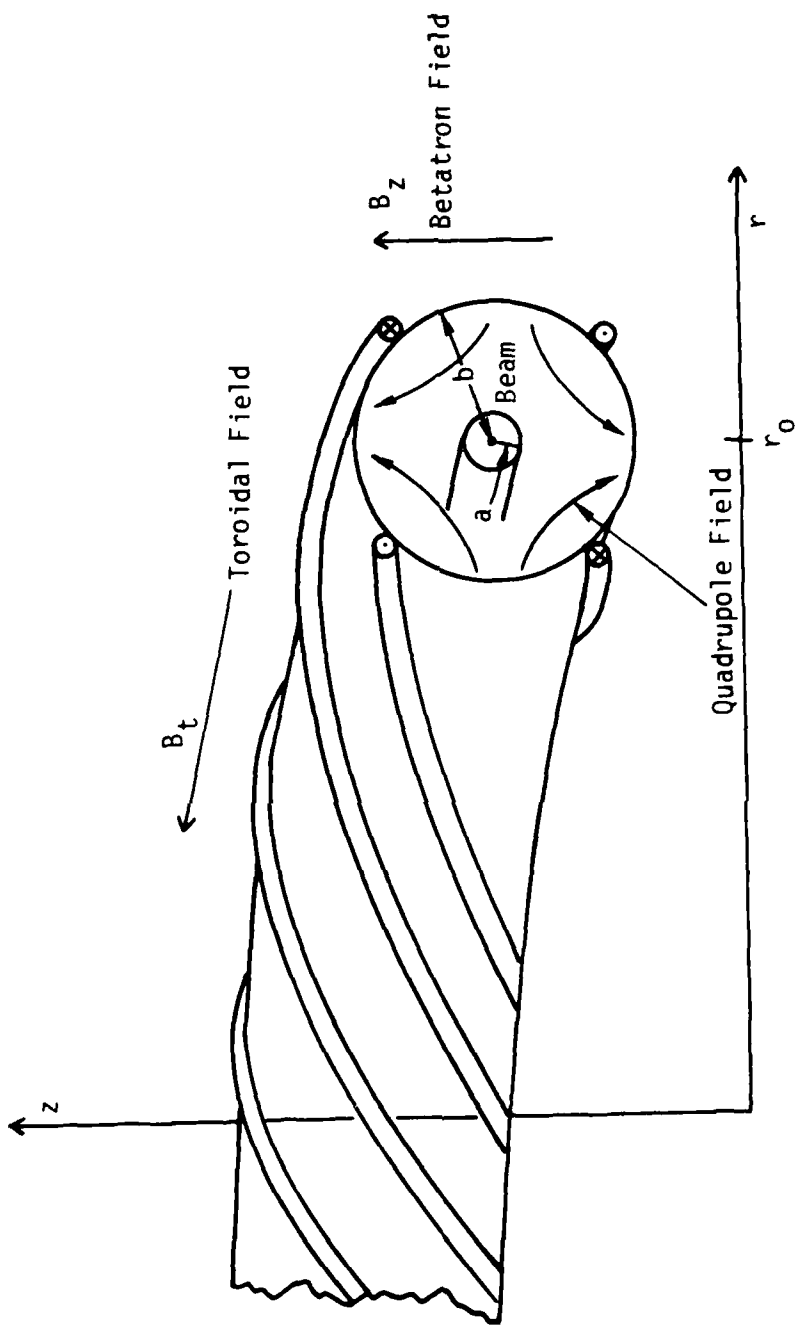


Figure 17. Magnetic field configuration in the stellatron device, showing the superposition of a vertical mirror field, a toroidal field, and a helical quadrupole field.

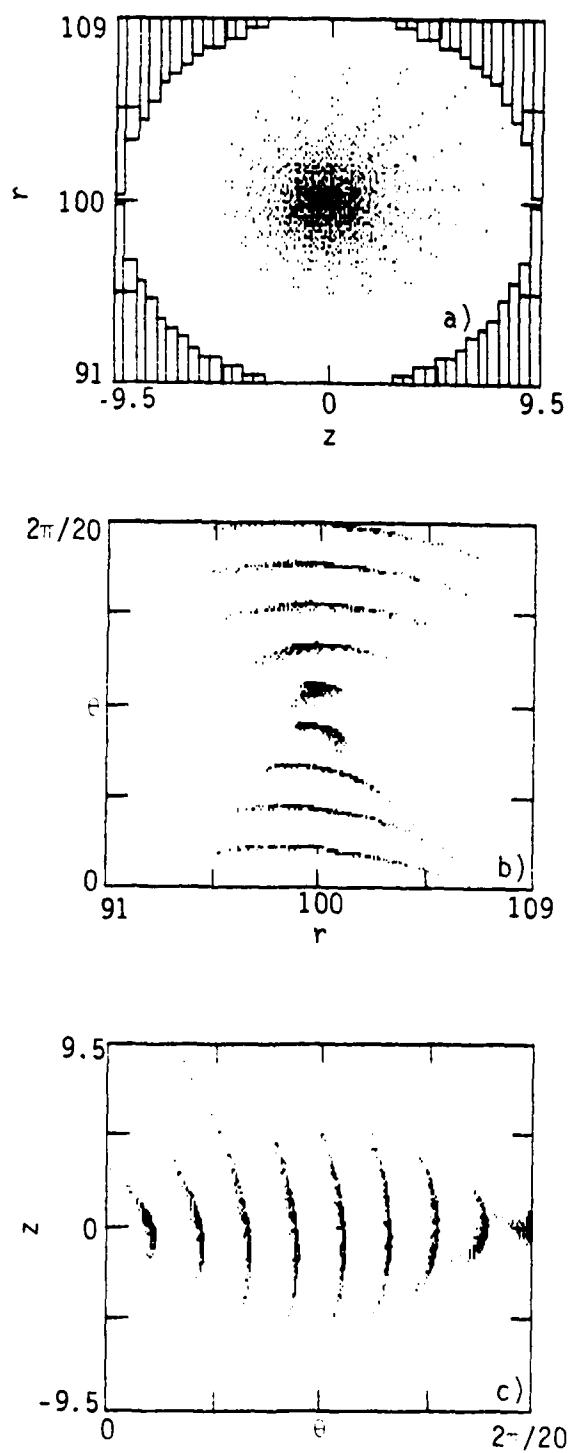
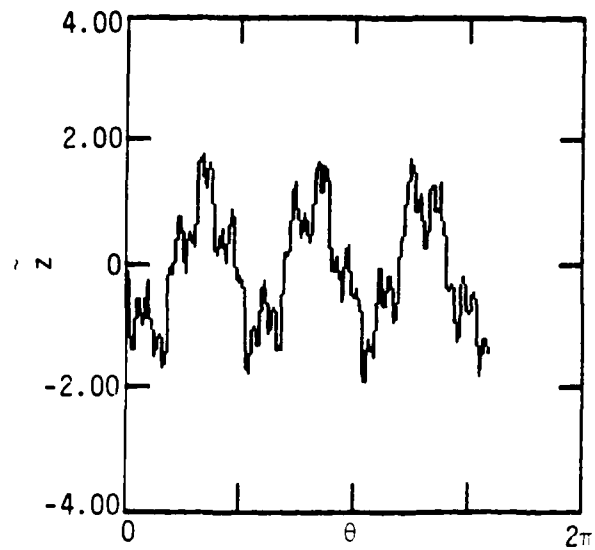
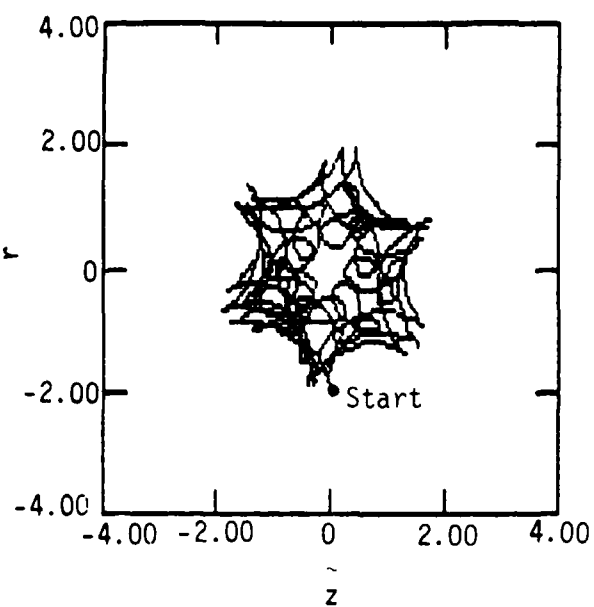
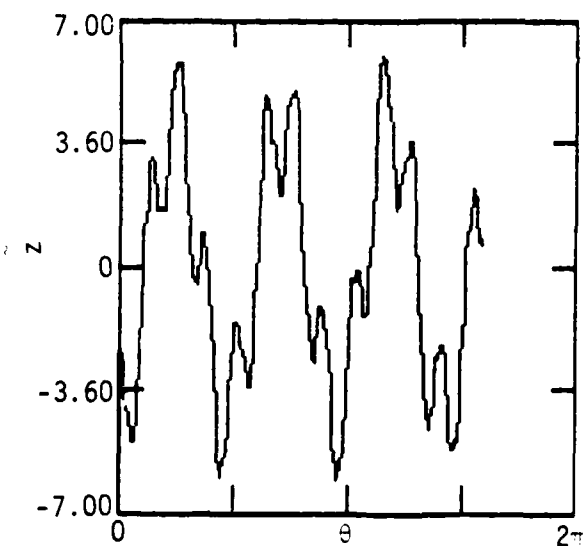
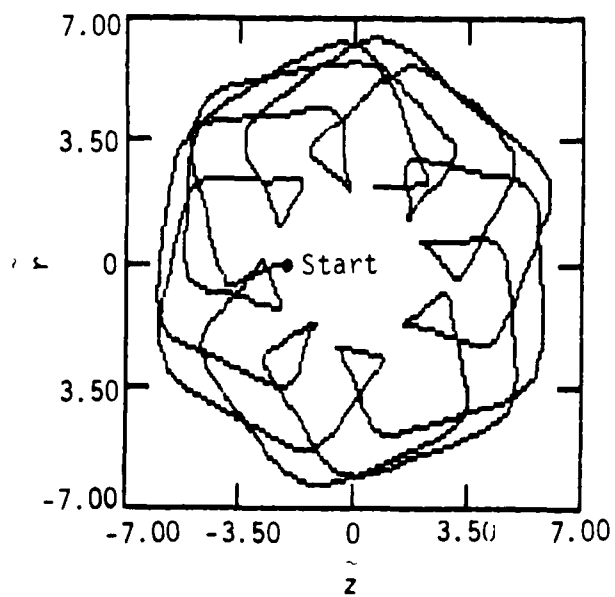


Figure 18. Large envelope oscillations excited in the stellatron by strong quadrupole fields. ( $I = 10$  kA,  $\gamma = 7$ ,  $B_e = 5$  kG,  $m = 20$ ,  $\varepsilon = 1.0$ ).



a)



b)

Figure 19. Numerically integrated orbits of particles which start at a)  
 $r = -2 \text{ cm}, z = 0, \dot{\theta} = 0$ , b)  $z = -2 \text{ cm}, \dot{r} = 0, \theta = 0$ . Note  
 that the dimensions of the boxes are different for a) and b).  
 $(R = 1 \text{ m}, B_0 = 5 \text{ kG}, \gamma = 7, m = 20, \epsilon = 1)$

amplitudes and phases are determined from the initial conditions. The simplest initial conditions to analyse are those of Fig. 19, where the particles are started off with zero transverse velocity. One can then show that for the particle in the focusing (defocusing) plane, its initial position is at an outer (inner) turning point of its poloidal motion. A plot of the amplitude of the particle orbits versus the quadrupole field strength is given in Fig. 20. Thus, the smallest amplitude betatron oscillations occur for particles started in the focusing plane.

We note that it is possible to take advantage of the mismatch properties of the stellatron without creating large envelope oscillations. Thus Ref. 3 shows that for the parameters in Fig. 18 and  $\epsilon = 0.5$ , the beam can easily withstand a 50% energy mismatch. Figure 20 shows that the maximum excursion due to the defocusing of the quadrupole field is about 1.6 times the initial displacement, for this value of  $\epsilon$ .

One practical implication of these results is that a particle injector, e.g., of the type used in the U.C. Irvine experiment, should be located in a focusing plane to ensure the smallest beam oscillations.

The above calculations assume  $m > 0$ , which means that the field-lines twist anti-clockwise as one goes in the positive  $\theta$  direction around the torus. As pointed out in Ref. 3,  $m < 0$  is an undesirable state from the point of view of stability. Even when the orbits for  $m \geq 0$  are both stable, however,  $m < 0$  gives larger amplitude orbits than  $m > 0$ , as can be seen from Fig. 21. Thus,  $m < 0$  is also undesirable from the point of view of keeping the orbit amplitudes small.

#### B. Numerical Simulations of Mismatched Equilibria Including Self-Fields.

In order to investigate the self-consistent behavior of a high current beam in a highly mismatched condition, we performed some IVORY simulations. We chose a current of 1 kA,  $B_\theta = 5$  kG, and stellarator windings

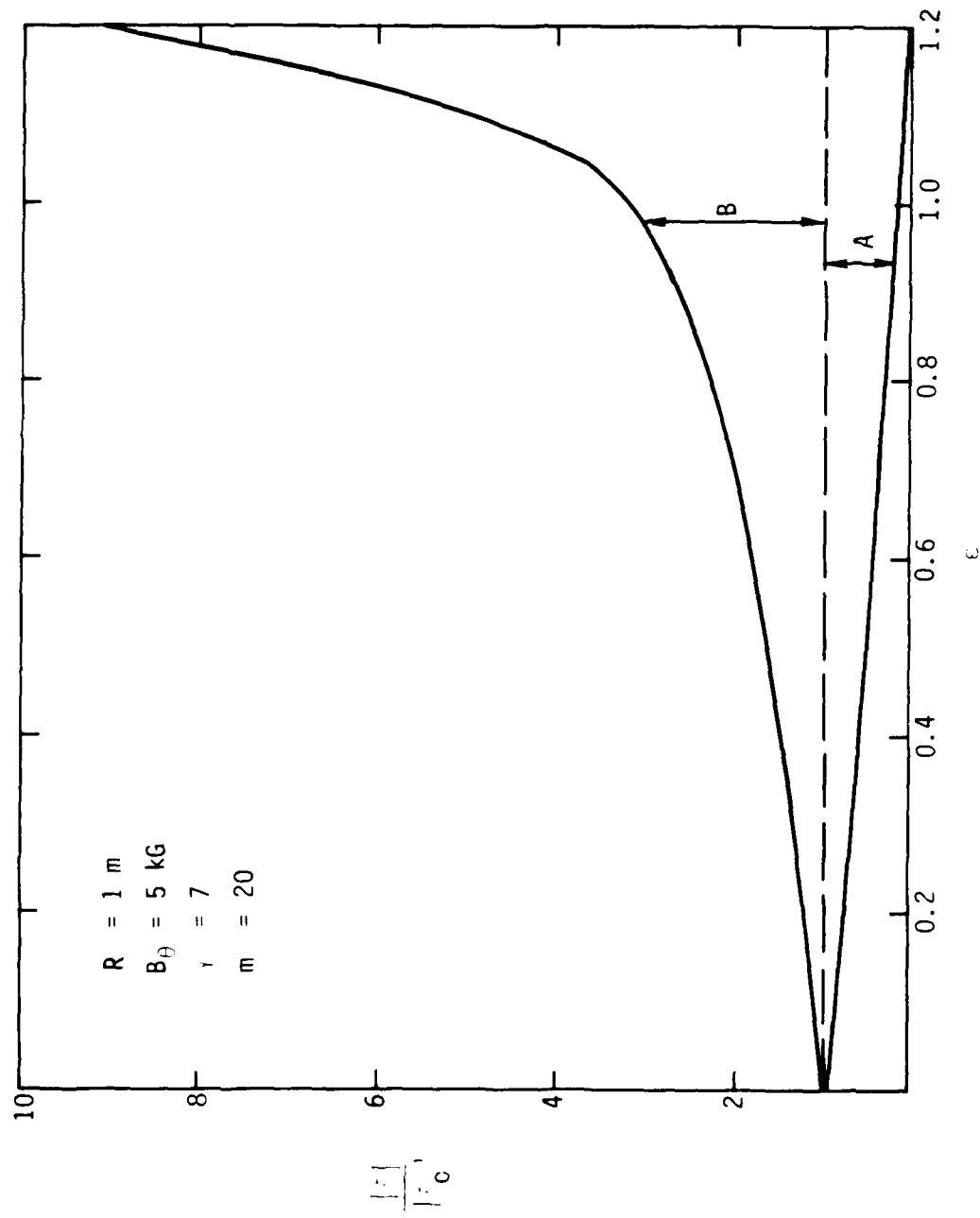


Figure 20. Dependence of amplitude of particle orbits  $|\xi|$  on strength of quadrupole field, as measured by  $\epsilon$ . For initial conditions of case (a) (see text), the particle oscillates over the range denoted by A, for case (b) the particle oscillates over the range B.

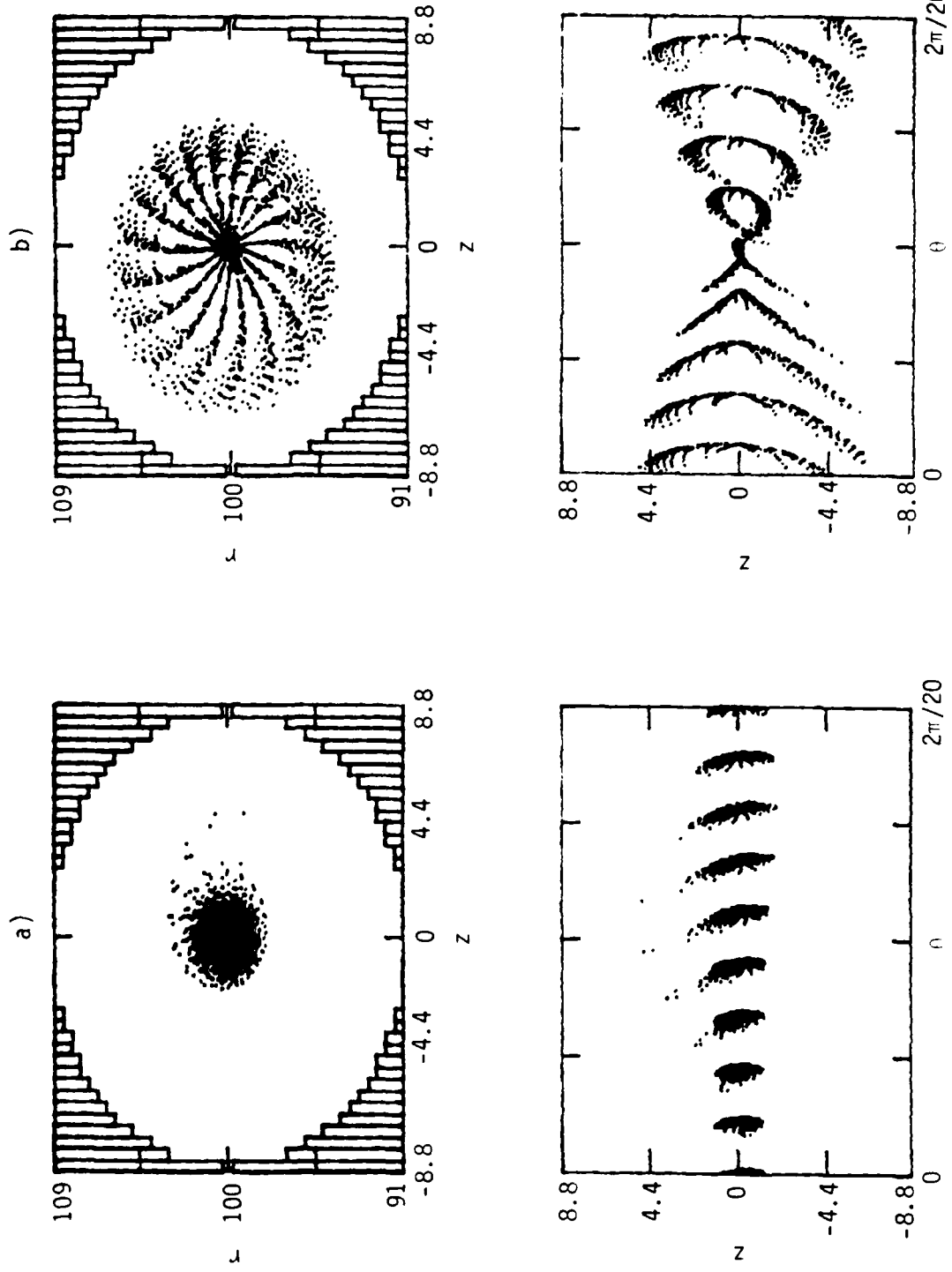


Figure 21. Contrast between effect of (a)  $m > 0$  and (b)  $m < 0$  helical windings on particle orbits in the stellatron. ( $I = 10$  kA,  $r_i = 7$ ,  $B_{\phi} = 5$  kG,  $|m| = 20$ ,  $\epsilon = 0.7$ )

with  $m = 20$  and  $\epsilon = 0.7$ . The beam was initialized as shown in Fig. 22. Field components with toroidal mode-numbers  $\lambda = 0, \pm 20$  were kept in the calculations. The nine groups of particles shown in Fig. 22 were sufficient to resolve the shortest wavelength i.e.,  $2\pi r_0/20$ . The value of the vertical field was chosen such that a beam with  $\gamma = 3.0$  would be matched. Two cases were looked at, one with  $\gamma = 10$ , and one with  $\gamma = 1.5$ . A snapshot of the beam with  $\gamma = 10$  after about seven revolutions around the torus is shown in Fig. 23. It can be seen that even with this huge mismatch, the beam is offset by only about 1 cm, which is consistent with the theoretical prediction obtained from Eq. (7) of Ref. 2. The latter predicts that if the beam starts off at  $r = R$ , with  $\gamma = 10$ , it should oscillate about the position  $r = R + 0.7$  cm with amplitude of 0.7 cm.

Figure 20 predicts that for  $\epsilon = 0.7$ , some particles should reach twice their initial displacement from the beam centroid. In Fig. 23, particles are found at larger displacements than this, probably due to the energy mismatch and self-field effects.

The results for  $\gamma = 1.5$  after approximately two major revolutions are shown in Fig. 24. The beam offset due to the mismatch is imperceptible. However, some degree of bunching is starting to occur in the toroidal direction with wavelength  $2\pi R/m$ . This may be due to a stable longitudinal oscillation of the low energy ring excited by the stellarator windings, or it could be an instability. These simulations were not run long enough to distinguish between these two possibilities.

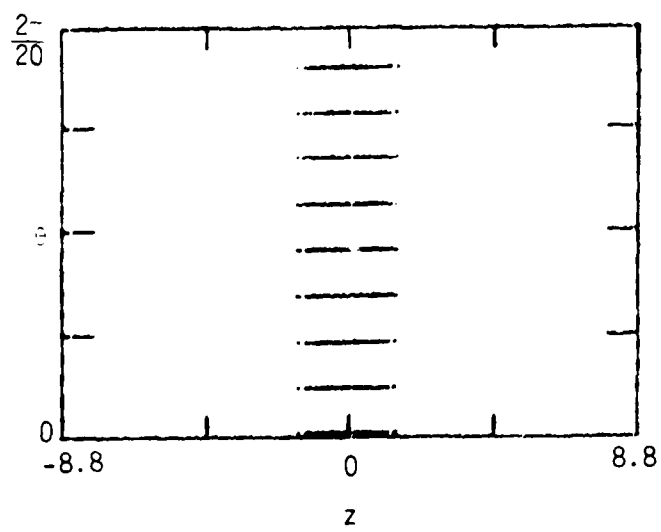
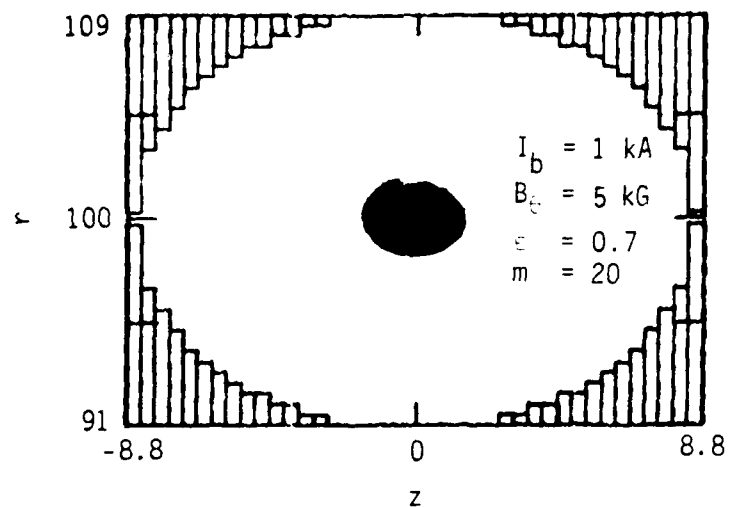


Figure 22. Initialization of simulation code for energy mismatch runs. The beam is placed at the center of the minor cross-section ( $r = 100$  cm,  $z = 0$ ). Nine groups of particles are used to resolve a segment of  $2\pi/m$  radians of the beam.

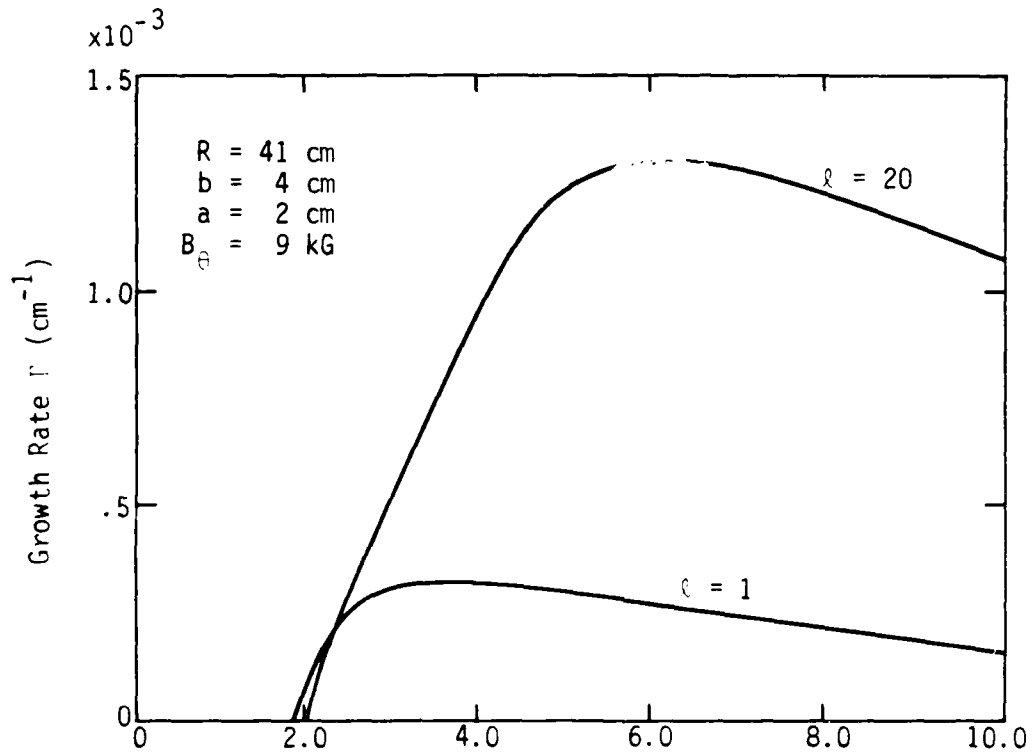


Figure 30. Cold beam growth rates for the UCI betatron parameters versus beam energy.

#### (D) Negative Mass Instability

As seen in Chap. V, the simulations we have performed of the negative mass instability in the stellatron show growth rates similar to those in the modified betatron at the same parameter values. We have therefore computed the growth rates of the negative mass instability for the UCI parameters in the absence of the stellatron windings in order to give a rough estimate of the magnitudes involved. The results, which assume zero frequency spread, are shown in Fig. 30. The growth rate of the  $\ell = 1$  instability is sufficient to make the instability nonlinear in 1  $\mu$ sec. We can estimate an effective frequency spread on the beam based on the results in Chap. III. From the single particle orbits in Fig. 28, we compute a poloidal rotation frequency of  $\omega_{pr} \approx 4 \times 10^{-3}$  cm $^{-1}$ . Assuming a 2 cm beam radius, we have  $\Delta_0 \approx 5 \times 10^{-4}$  cm $^{-1}$ . Thus, for  $\ell = 1$ , we have  $\ell\Delta_0 < \omega_{pr}$  so that the effective frequency spread of the particles is of order  $(a/R)^2 = 6 \times 10^{-5}$  cm $^{-1}$ . This is insufficient to stabilize the mode, since the cold beam growth rate is  $\Gamma \approx 2 \times 10^{-4}$  cm $^{-1}$ . For  $\ell = 20$ , on the other hand,  $\ell\Delta_0 > \omega_{pr}$ , so the frequency spread approaches the upper-bound result i.e.  $\Delta \approx \Delta_0 = 5 \times 10^{-4}$  cm $^{-1}$ . The latter value easily stabilizes the  $\ell = 20$  mode for which  $\Gamma = 1.1 \times 10^{-3}$  cm $^{-1}$  (from Fig. 30). Our calculations, therefore, based on the assumption of a beam radius of about 2 cm, predict that low  $\ell$ -numbers are unstable and high  $\ell$ -numbers are stable. Additional work is necessary to confirm these predictions, such as, for example, an analytic model which includes the stellatron fields, and IVORY simulations. What is clear from the experiment is that if the negative mass instability is occurring, it is not causing any major disruption of the beam since acceleration takes place over  $\sim 100$   $\mu$ sec. It may be that the strong focusing of the stellatron windings is sufficient to contain the beam in spite of the nonlinear development of the instability [cf. Fig. 25].

The above calculations assume a monoenergetic beam. An alternative explanation of beam stability is possible if one assumes a significant (~ 10%) energy spread on the beam and that the beam radius is determined solely by this spread. In this case, there is no net poloidal rotation and the effective frequency spread is  $\Delta_0$ , independent of  $\ell$ . For a 2 cm radius beam, this spread is sufficient to stabilize all  $\ell$ -numbers.

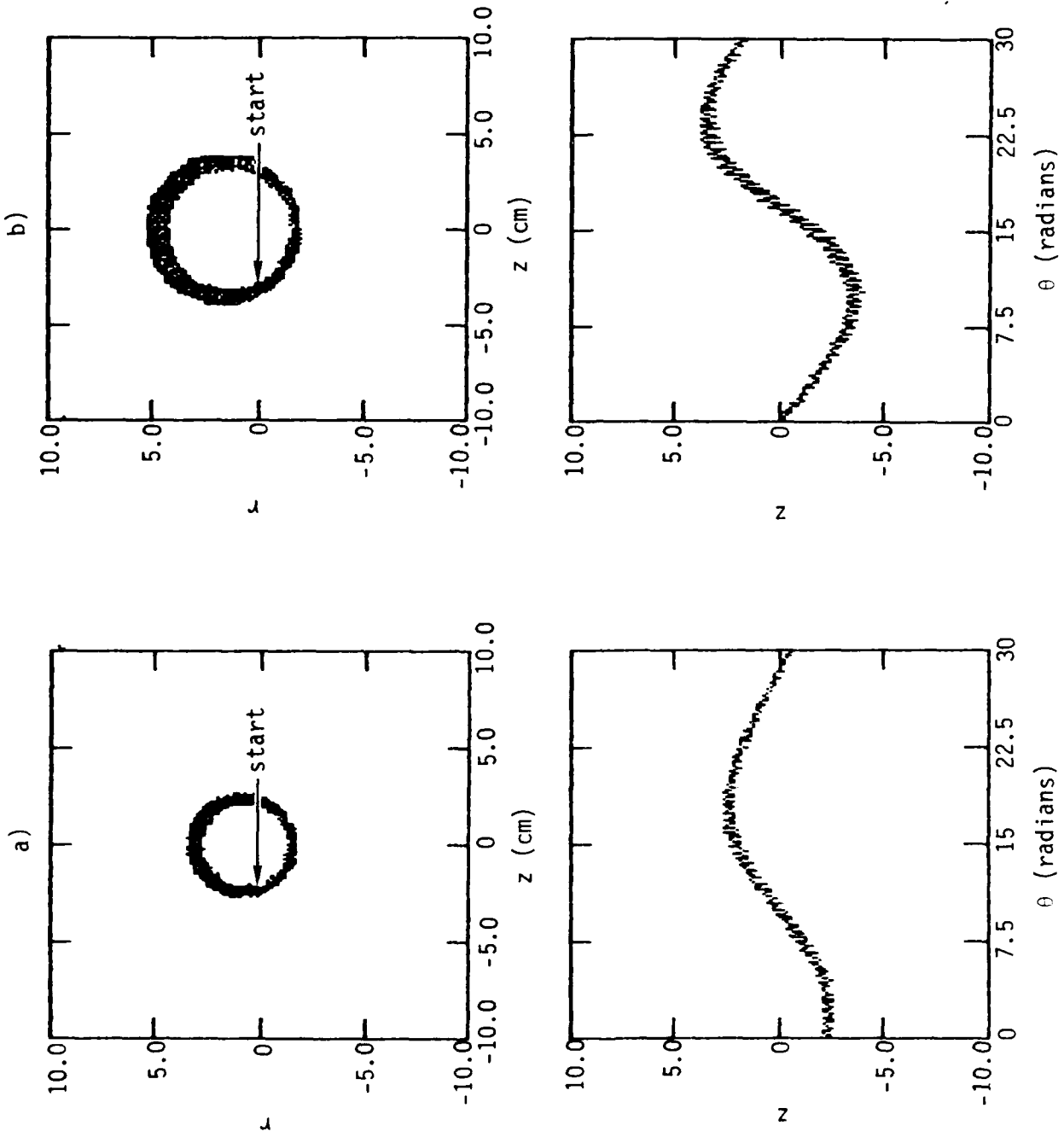


Figure 29. Orbits in the UCI stellatron at  $\gamma = 9$  with (a) 10% and (b) 20% energy mismatch.

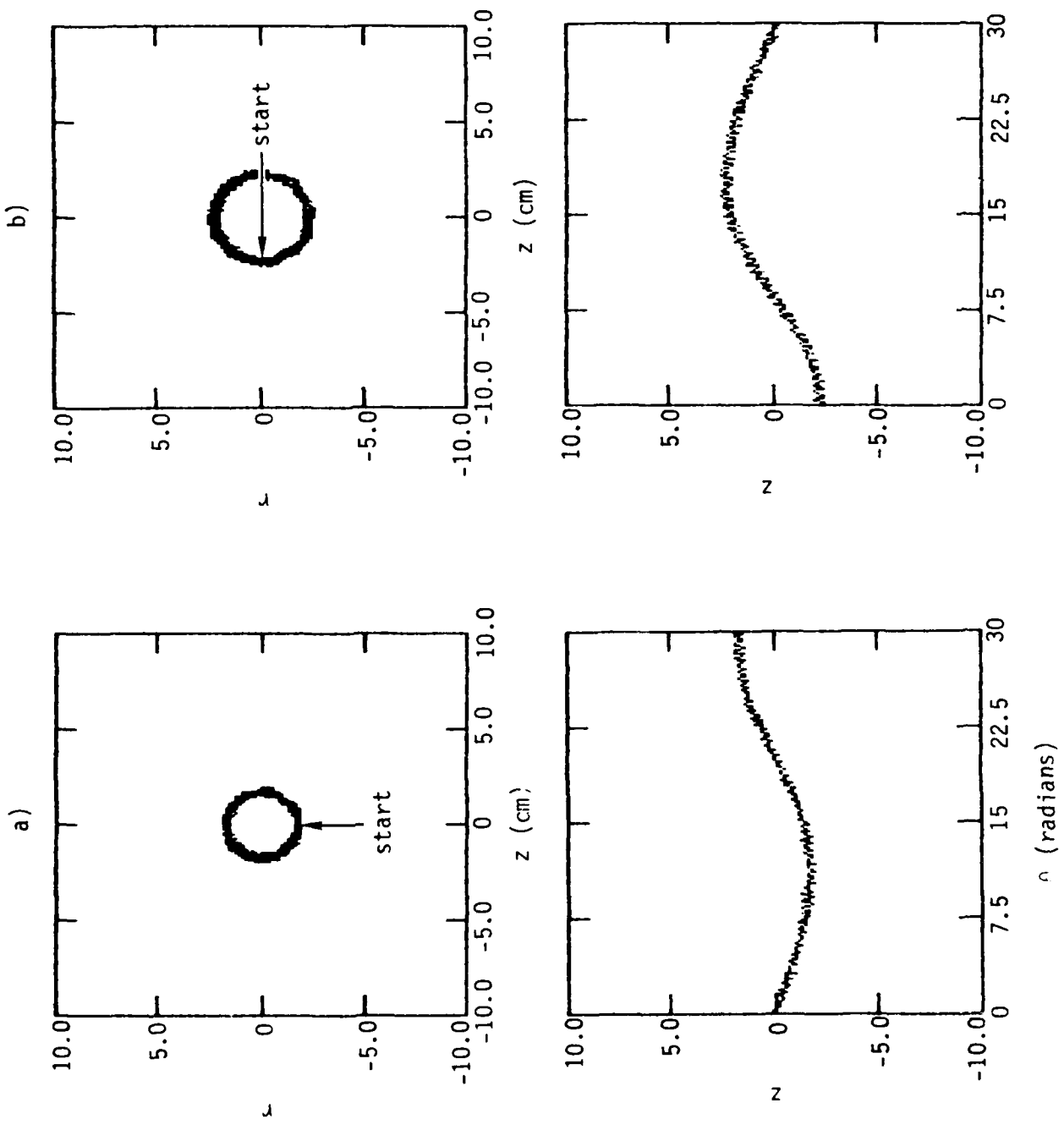


Figure 28. Orbits in the UCI stellatron at  $\gamma = 9$  for energy-matched particles started in the (a) focusing and (b) defocusing planes.

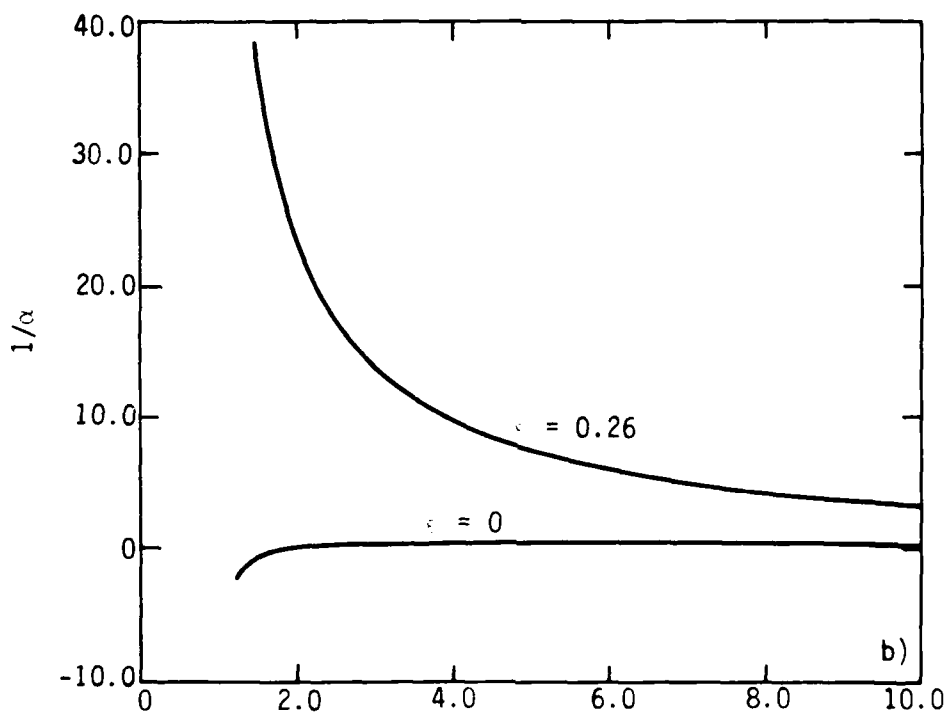
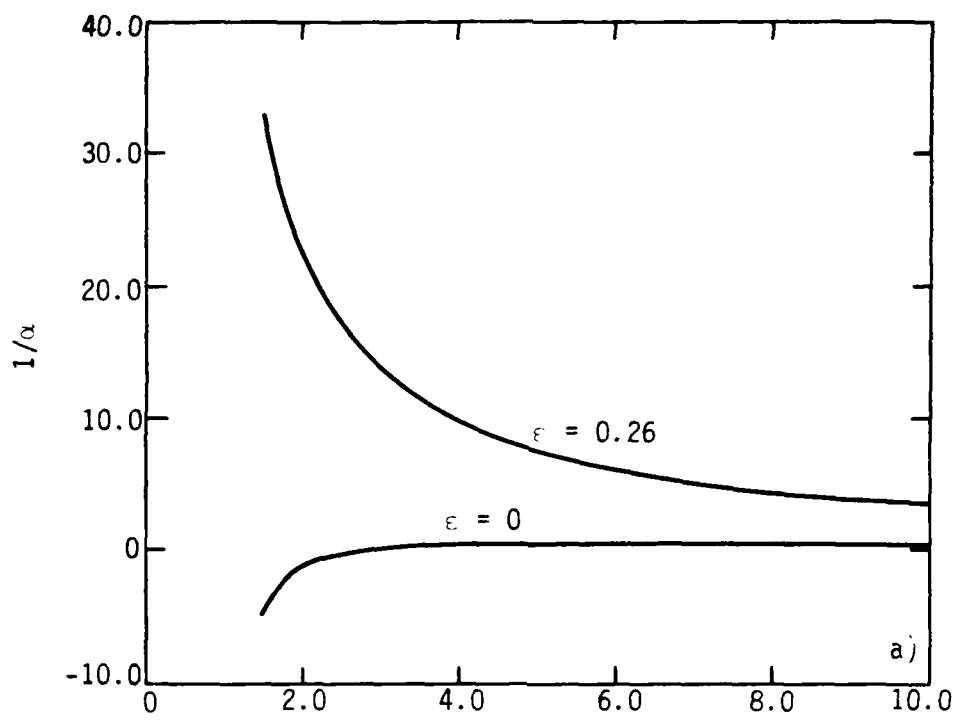


Figure 27. Inverse of momentum compaction,  $1/\alpha$ , versus beam energy in the UCI stellatron, for (a) single particles and (b) the beam centroid.

in Fig. 27. The difference is greatest at low energies. Even at  $\gamma = 9$ , which is the final energy of the UCI beam, the stellatron configuration tolerates about seven times more mismatch than the modified betatron.

### (B) Transition From Positive to Negative Mass

The stellarator windings give rise to a transition energy at which the effective toroidal particle inertia changes sign.<sup>25</sup> This is in contrast to the modified betatron, where, in the absence of self-field effects, the particle mass is negative at all energies. The equation for the transition energy is

$$\gamma_{st} \sim \left( \frac{1}{2} + \frac{\mu^2}{\mu^2 + m_p - 1/2} \right)^{1/2} \quad (71)$$

This equation is implicit, since  $\gamma$  appears on each side. To compute  $\gamma_{st}$  we rationalized Eq. (71) to obtain a fifth order polynomial in  $\gamma$ . There is only one physically meaningful root in general, which gives the transition energy. For the UCI parameters,  $\gamma_{st} = 3.4$ . The beam is therefore in the negative mass regime over most of the acceleration cycle.

### (C) Single-Particle Orbits

A single-particle code was used to generate the orbits shown in Figs. 28-29. The parameters used correspond to near the end of the acceleration cycle. The orbits in Fig. 28 are for a particle with matched energy. The strong toroidal field keeps the particle confined to a thin annulus in the transverse plane regardless of whether it starts off in the focusing or defocusing plane. It also gives rise to the slow precessional motion of the particle about the center (cf. Fig. 19, where the particles precess about the center much faster). This slow precessional frequency is roughly one sixth of the toroidal frequency. The effect of 10% and 20% mismatch in the energy is seen in Fig. 29. These results agree well with Eq. (70) and Fig. 27, which predict radial shifts in the orbit of 1.35 cm and 2.7 cm for the 10% and 20% mismatches, respectively.

## VI. CALCULATIONS FOR THE UCI STELLATRON

In this chapter we describe some calculations carried out specifically for the stellatron experiment at the University of California at Irvine. The most recent results from this experiment<sup>8</sup> indicate that a beam of about 200 A is accelerated from the injection energy of 20 kV up to an energy of 4 MeV. Other parameters for the machine are given in Table 7. For these parameters, we have calculated the momentum compaction, evaluated the transition energy from positive to negative mass, looked at single particle orbits, and generated some growth rate curves for the negative mass instability.

Table 7. UCI Stellatron Parameters.

|                      |                           |
|----------------------|---------------------------|
| Torus Major Radius   | 41 cm                     |
| Torus Minor Radius   | 4 cm                      |
| Beam Radius $a$      | 2 cm (assumed)            |
| Beam Current         | 200 A                     |
| Beam Energy          | 20 kV - 4 MeV             |
| Toroidal Field       | 0 - 9 kG                  |
| External Field Index | $\approx 1/2$             |
| Stellarator Fields   | $\epsilon = 0.26, m = 12$ |
| Acceleration Time    | 100 $\mu$ sec             |

### (A) Momentum Compaction

We define the momentum compaction factor  $\alpha$  through

$$\frac{\Delta r}{R} = \frac{\alpha \Delta \gamma}{\gamma} \quad (70)$$

where  $\Delta \gamma$  is the energy mismatch, and  $\Delta r$  is the resulting radial shift of the particle orbit. For the modified betatron,  $1/\alpha = 1/2 - n_s$ , while for the stellatron,<sup>3</sup>  $1/\alpha = 1/2 - n_s + \mu^2 (m^2 + mp - 1/2 + n_s)^{-1}$ , where  $n_s$  is the self-field index,  $\mu$  is the amplitude of the quadrupole field index and  $p$  is the ratio  $B_\theta/B_z$ . The above definition of  $\alpha$  is for a single particle. One can define a compaction factor for the beam as a whole by replacing  $n_s$  by  $n_s a^2/b^2$ . We compare the stellatron compaction factors to those of the modified betatron configuration, for the UCI parameters,

as before at approximately the same growth-rate. This behavior is suggestive of a resonant interaction between the beam and a wave-guide mode. The analytic work performed for the modified betatron, however, indicates that in that device, such an interaction can never occur, because the wave-guide modes always have higher frequency than the beam modes. The growth rate predicted in the absence of the helical windings (i.e., for the modified betatron) is just  $\Gamma = 1 \times 10^{-3} \text{ cm}^{-1}$ , and this value is not sensitive to the cross section. At this point, we only speculate that one of the transverse modes in the stellatron has a frequency high enough to interact with the wave-guide modes (i.e., a gyrotron-type resonance).

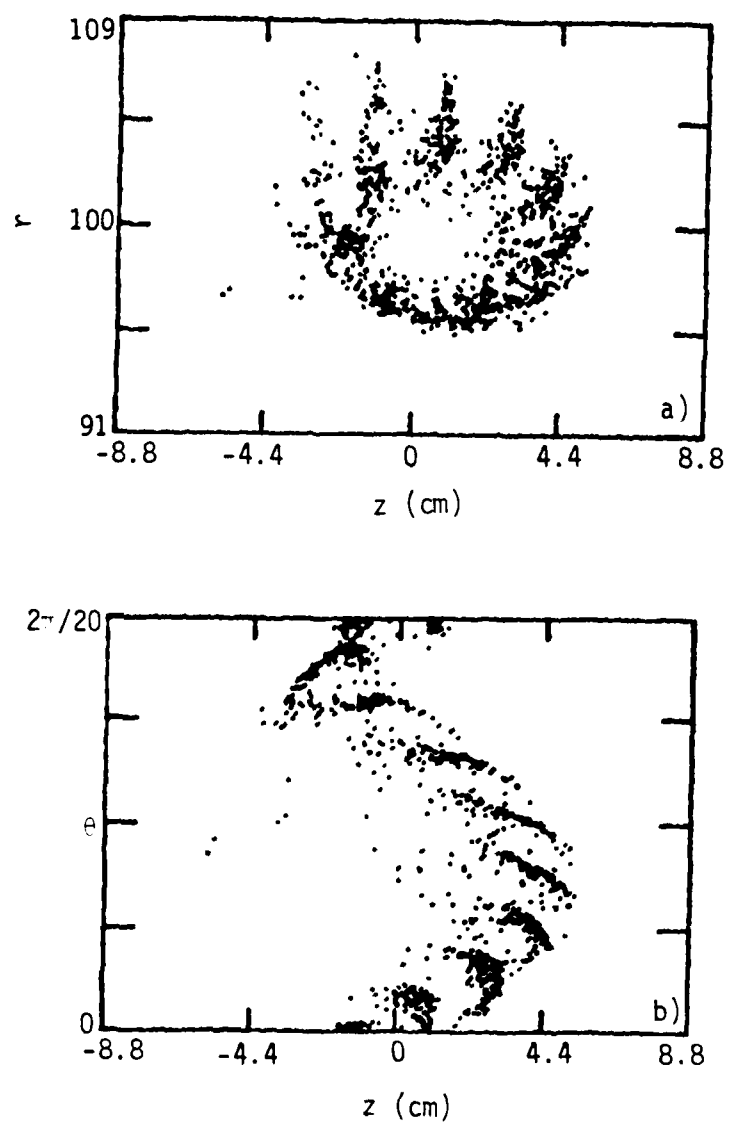


Figure 26.  $\ell = 20$  instability of a 10 kA,  $\gamma = 7$  beam in a stellatron.  
This may be a gyrotron-type instability.

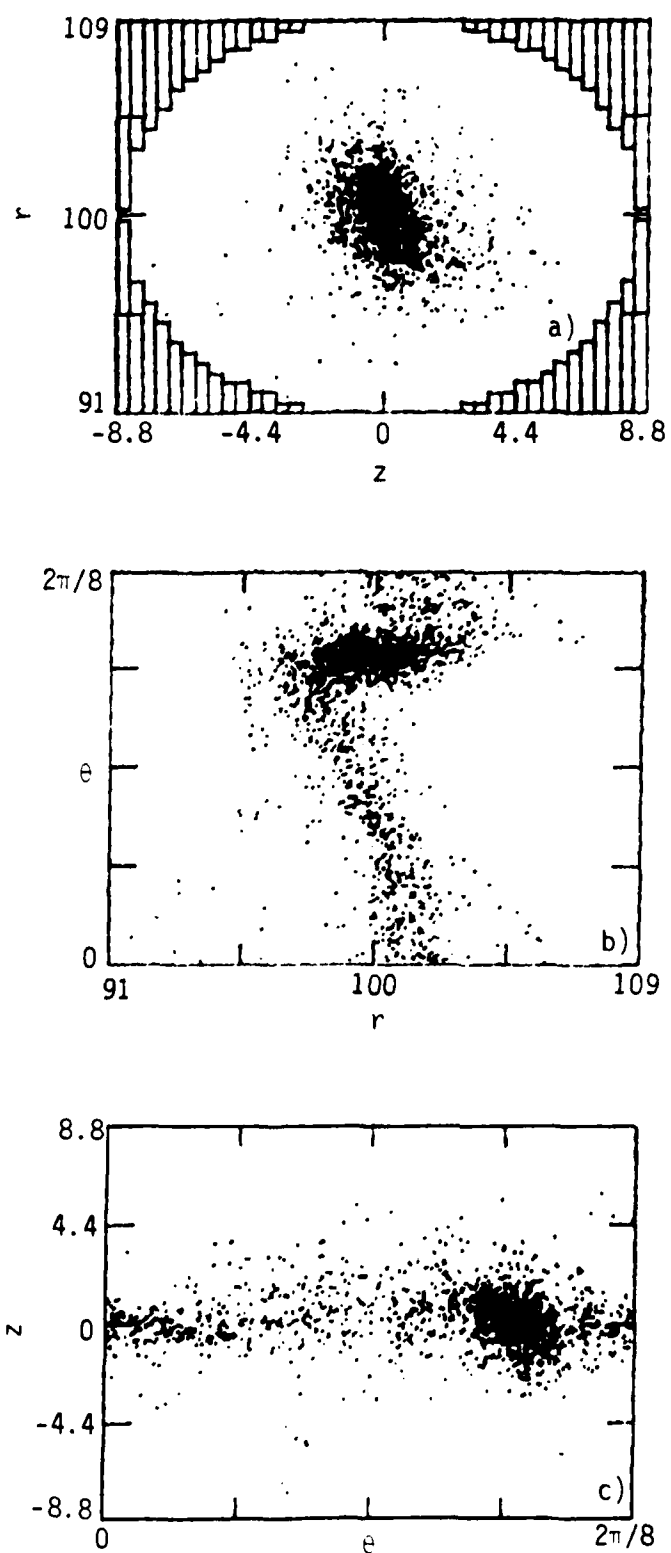


Figure 25. Nonlinear development of  $\ell = 8$  negative mass instability in the presence of strong stellatron fields ( $\varepsilon = 1.4$ ). Little radial particle loss is observed.

the absence of self-field effects.<sup>25</sup> For the parameters in the simulations just described, the transition occurs at  $\gamma_{st} = 7.9$  (see Chap. VIB). Below this energy, one would not expect to see any negative mass instability. (At high currents, other instabilities may exist below this threshold.)

We now present some results for high current ( $\sim 10$  kA) beams above the negative mass transition energy and see how the results depend on the strength of the strong focusing. We consider an energy of 5.5 MeV, with a toroidal field of 1 kG, and stellatron windings with  $m = 8$ . The first run we perform is for  $\epsilon = 0.35$ , for which  $\gamma_{st} = 2.3$ . The simulation shows that development of the  $\lambda = 8$  negative mass instability is hardly affected by the strong focusing. The growth rate is  $\Gamma = 1.7 \times 10^{-3}$  cm $^{-1}$ , compared to the modified betatron result of  $2 \times 10^{-3}$  cm $^{-1}$ . In the nonlinear stage, about three-quarters of the particles are lost to the wall. When  $\epsilon$  is increased to 1.4, ( $\gamma_{st} = 5.2$ ) the results are somewhat different. The linear growth rate is reduced to about  $7.5 \times 10^{-4}$  cm $^{-1}$ , and while the beam becomes highly bunched in the toroidal direction, little particle loss occurs, due to the strength of the focusing (see Fig. 25).

We report finally on some stellatron simulations which are not clearly understood at this time. These were for a 10 kA,  $\gamma = 7$  beam in a 5 kG toroidal field. The stellarator windings had  $\epsilon = 0.7$  and  $m = 20$ . In the first run, the torus was assumed to have a square cross-section, 17.6 x 17.6 cm. We found that the  $\lambda = 20$  mode on the beam had a large growth rate  $\Gamma = 5 \times 10^{-3}$  cm $^{-1}$ , and the beam was disrupted in just one major turn, as shown in Fig. 26. A subsequent run with a round cross section with radius  $b = 8.8$  cm, and everything else unchanged, showed no growth in 8 major revolutions. It was suspected that since the  $\lambda = 20$  mode has a frequency near the electromagnetic cutoff the torus,  $\omega_c = \sqrt{2} \pi/L$ , where  $L$  is the length of the side in the square cross section case, the beam behavior might be sensitive to the transverse dimensions at this frequency. We therefore increased the radius of the round cross section case to give it the same cut-off as the square cross section case, namely  $b = 2.4 L/\sqrt{2\pi} = 9.5$  cm. With this radius, the beam again exhibited the same strong growth

## V. STELLATRON ACCELERATOR: STABILITY

As we saw in the previous chapter, the stellatron has an energy-mismatch tolerance much superior to that of the modified betatron. We now attempt to discover whether this strong focusing has an effect on beam stability. In this work, we rely heavily on IVORY simulations, lacking an analytic theory of stellatron stability. It must be stated that the addition of stellarator windings to the modified betatron adds two new parameters,  $m$  and  $\mu$ , to an already large parameter space. A large simulation code like IVORY is clearly not the tool to use in optimizing the choice of parameters in the stellatron. Therefore, we confine ourselves to running simulations at beam parameters for which we already know and understand the results in the modified betatron.

The first simulations we describe are for the  $l = 20$  modes on a moderate-current (1kA) beam at low energy (1-2.5 MeV). The other parameters for these runs are  $B_0 = 5$  kG,  $R = 1$  m,  $b = 10$  cm,  $a = 2$  cm, and  $m = 20$  windings with  $\epsilon = 0.7$ . It is interesting to compare the results with those described for the modified betatron in Chap. III. At 1 MeV, we find that the stellatron, like the betatron, is stable through 15 major revolutions (the length of the simulation). This result is not surprising, since at this energy the cold-beam dispersion relation for the modified betatron predicts stability. At 2.5 MeV, we again find stability in both machines, while the cold beam modified betatron theory of Chap. II predicts instability (Fig. 14). The reasons for stability are different in the two cases, however. As argued in Chap. III, the modified betatron run is stable because of the frequency spread on the beam. The graphical output from the stellatron run, however, shows a frequency spread which is almost an order of magnitude smaller. This allows us to put an upper bound of  $\leq 2.0 \times 10^{-4}$   $\text{cm}^{-1}$  on the cold-beam growth rate of the instability in the stellatron. This value is significantly less than the growth rate predicted for the modified betatron case, namely  $\Gamma = 6 \times 10^{-4}$   $\text{cm}^{-1}$  as seen in Fig. 14. This finding is consistent with the fact that the stellatron has a transition energy below which the effective mass of the particles is positive, even in

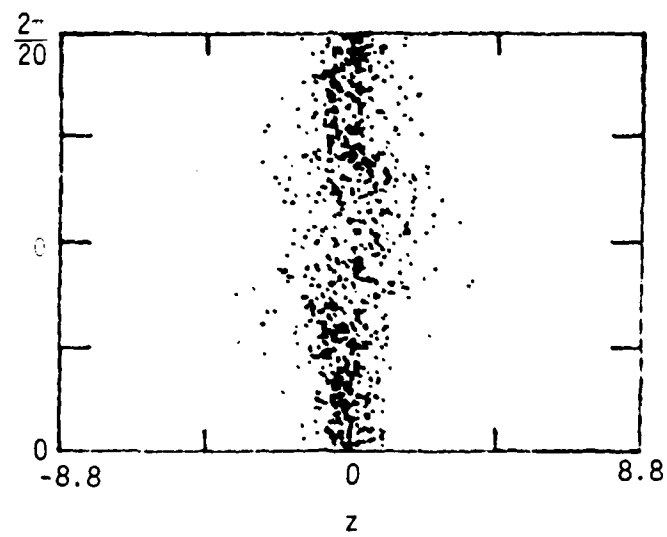
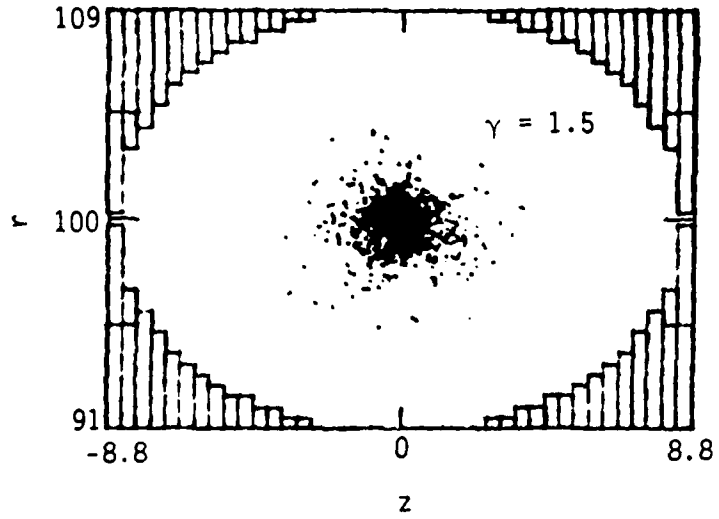


Figure 24. Snapshot of beam with  $\gamma = 1.5$  after 42 ns ( $\approx 2$  major revolutions).

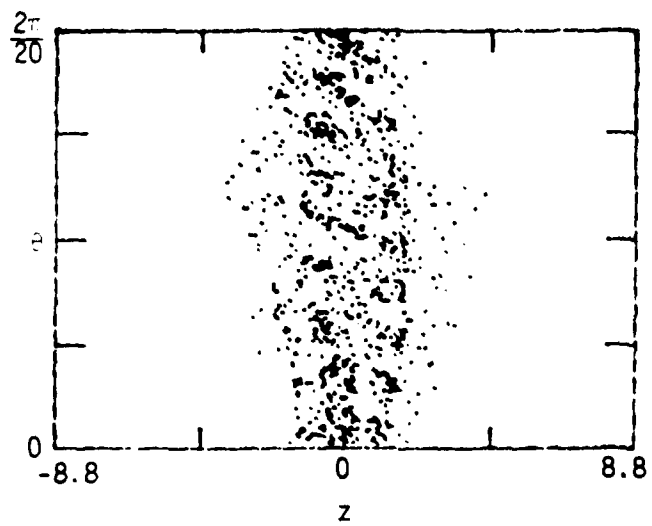
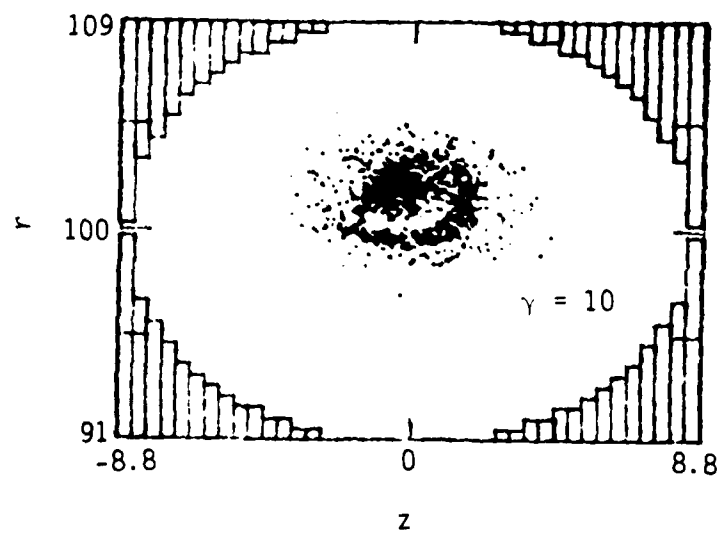


Figure 23. Snapshot of beam with  $\gamma = 10$  after 145 ns ( $\approx 7$  major revolutions).

## VII. CALCULATIONS FOR THE REVERSING SOLENOIDAL LENS BETATRON

The reversing solenoidal lens (RSL) betatron<sup>4</sup> [Fig. 31], uses a series of alternating-direction solenoids to provide strong focusing of the beam. An experimental machine is under construction at the University of New Mexico. Unlike the modified betatron and stellatron, the average toroidal field in this device is zero. It is proposed to inject the beam into the toroidal drift-tube from a shielded cathode, i.e., so that the beam has zero canonical angular momentum. This means that when it enters the magnetic field, the beam rotates poloidally at the Larmor frequency  $\Omega_L = \Omega_0/2\gamma$ . As the beam travels from one lens to the next, the direction of rotation alternates. Thin lens theory<sup>26</sup> shows that in order for the orbit to be stable, the "phase-advance per cell"  $\Omega_L d/V_0$ , where  $d$  is the length of one solenoid, must be less than  $\pi$ . In practice, it is advisable to be well within this constraint. For the experimental injection parameters,  $\gamma = 2.0$ ,  $B_0 = 80$  Gauss, and  $d = 30$  cm, we obtain  $\Omega_L d/V_0 = 0.4$ . Note that since the poloidal rotation of the beam keeps alternating direction, and the phase-advance is small, the particle orbits are essentially like those of Fig. 12(a). The RSL therefore provides the maximum possible amount of frequency spread for a given beam radius, which is very favorable for beam stability.

The RSL betatron bears a resemblance to the bumpy-torus betatron looked at by Chernin et. al.<sup>27</sup> The latter device consists of a modified betatron with a sinusoidal modulation of the toroidal field. As the modulation increases the bumpy torus becomes like a solenoidal lens device with very thick lenses. Stability calculations for the bumpy torus show that the beam is unstable in the vicinity of points where  $p^2 + 2 - 4 n_s = m^2 q^2$ , where  $q$  is an integer and  $p$  is the ratio of the solenoidal field to the vertical field. Now, if the canonical poloidal angular momentum of the beam is zero, as it is in the solenoidal lens device (since magnetic flux is excluded from the cathode), it automatically satisfies  $p^2 + 2 - 4 n_s = 0$ , assuming that the emittance of the beam is small. This implies that the beam lies at or near the boundary of an unstable region at all times, i.e.,

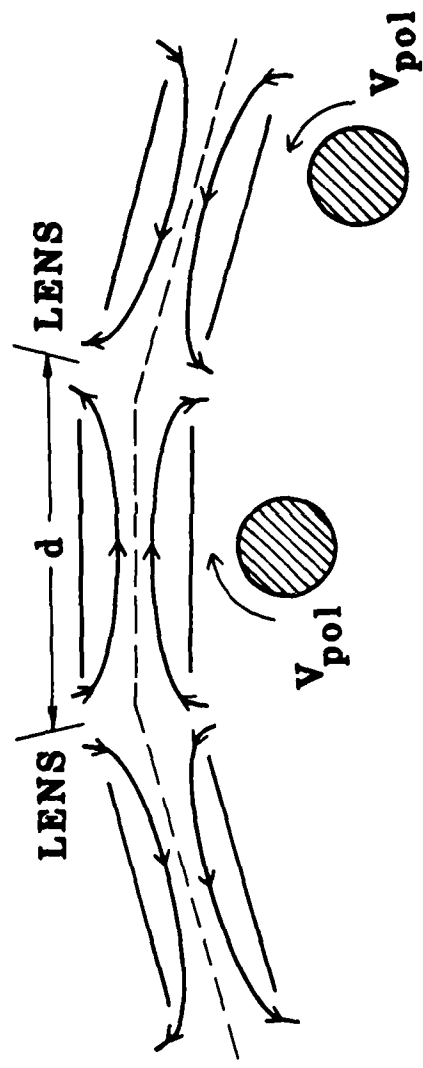


Figure 31. Reversing Solenoidal Lens Betatron configuration. The poloidal beam velocity  $v_{pol}$  reverses direction from one solenoid to the next.

the beam is marginally stable. This is not surprising, since  $p^2 + 2 - 4n_s = 0$  is the condition for Brillouin flow, and therefore specifies the maximum current density that can be transported for a given value of  $B_\theta$ . If  $B_\theta$  drops below this value, then the beam becomes unstable. However, all that happens is that the beam radius increases until the current density drops enough to make the beam stable. If the change in  $B_\theta$  is non-adiabatic, then, in addition, envelope oscillations, with frequency  $\Omega_L$ , are excited. This is what is observed in IVORY simulations of the beam as it travels around the torus. In these simulations, the solenoidal magnetic fields used are the exact, numerically computed values for finite-length straight solenoids. The solenoids are 21 cm in length, 6 cm in radius, and spaced 10.5 cm apart. There are thus 20 solenoids around the 1 m radius torus. The value of the solenoidal magnetic field for which the envelope oscillations are smallest is found to be about 100 Gauss for a 100 A, 1 MeV beam with a 2 cm radius. As the solenoidal field is varied about this value, the envelope oscillations increase in amplitude. Runs at 120 and 50 Gauss show significant oscillations (the beam envelope reaches twice its initial radius for the latter case), but the orbits are stable through one major turn (i.e., through 20 lenses), which is as far as we ran the code.

In addition to simulations at the low currents with which the initial experiments will be carried out, we have performed a number of runs at high current. We find that a solenoidal field of 600 Gauss can transport a 10 kA, 5.5 MeV, 2 cm radius beam with minimal (< 10%) envelope modulation. Note that because of the strong-focusing nature of the solenoidal lenses, the toroidal field contributes to the energy-mismatch tolerance of the device. We can compute the momentum-compaction factor by noting that in the thin-lens, small phase-advance limit, the solenoidal lenses act like a continuous radial focusing force on the beam. The linearized radial force equation is, in normalized units,

$$\Delta \ddot{r} + \Delta r (1/2 - n_s + p^2) \Omega^2 z / \gamma^2 = \Delta \gamma / \gamma R \quad (72)$$

where  $\Delta r$  is the perturbed radial displacement from the matched orbit,  $\Delta \gamma$  is

the perturbed particle energy, and other parameters are as defined in Chap. VI. Thus, the momentum compaction factor is given by

$$\alpha^{-1} = 1/2 - n_s + p^2 \quad (73)$$

for single particles. For the beam as a whole, one replaces  $n_s$  by  $n_s a^2/b^2$  to get the momentum-compaction. Comparing these expressions with those for the modified betatron in Sec. VI, one finds that for the 10 kA beam, the energy tolerance in the solenoidal lenses is greater by about a factor of four than that in a uniform toroidal field.

Having obtained an equilibrium for the 10 kA beam with  $\gamma = 12$ , we proceed to perturb it slightly, and look at the  $\ell = 20$  mode on the beam. We find that this mode grows rapidly with  $\Gamma = 5.4 \times 10^{-3} \text{ cm}^{-1}$ . With a growth rate this large, the frequency-spread damping  $\ell\Delta_0 = 1.6 \times 10^{-3} \text{ cm}^{-1}$  is insufficient to give stability. The effect of the instability on the beam is shown in Fig. 32. Classic negative mass ( $B_\theta = 0$ ) behavior is exhibited, with the radial motion of the beam leading to toroidal bunching. The linear growth rate is, in fact, very close to that for a conventional ( $B_\theta = 0$ ) betatron with the same beam parameters. Now, since  $n_s > 1/2$  for the beam, a self-consistent equilibrium does not exist when  $B_\theta = 0$  (the negative mass growth rate is nevertheless obtainable from the rigid-disk model). Therefore it would appear from this result that at  $\gamma = 12$ , the beam equilibrium is held together by the solenoidal lenses, but instabilities behave as if the toroidal field were zero. If this is so, then the advantage of the large frequency spread in the RSL must be weighed against the enhanced growth rates for  $B_\theta = 0$ . These conclusions are speculative at this point, and we hope to perform additional analytic and numerical work to clarify the linear behavior of the solenoidal lens betatron.

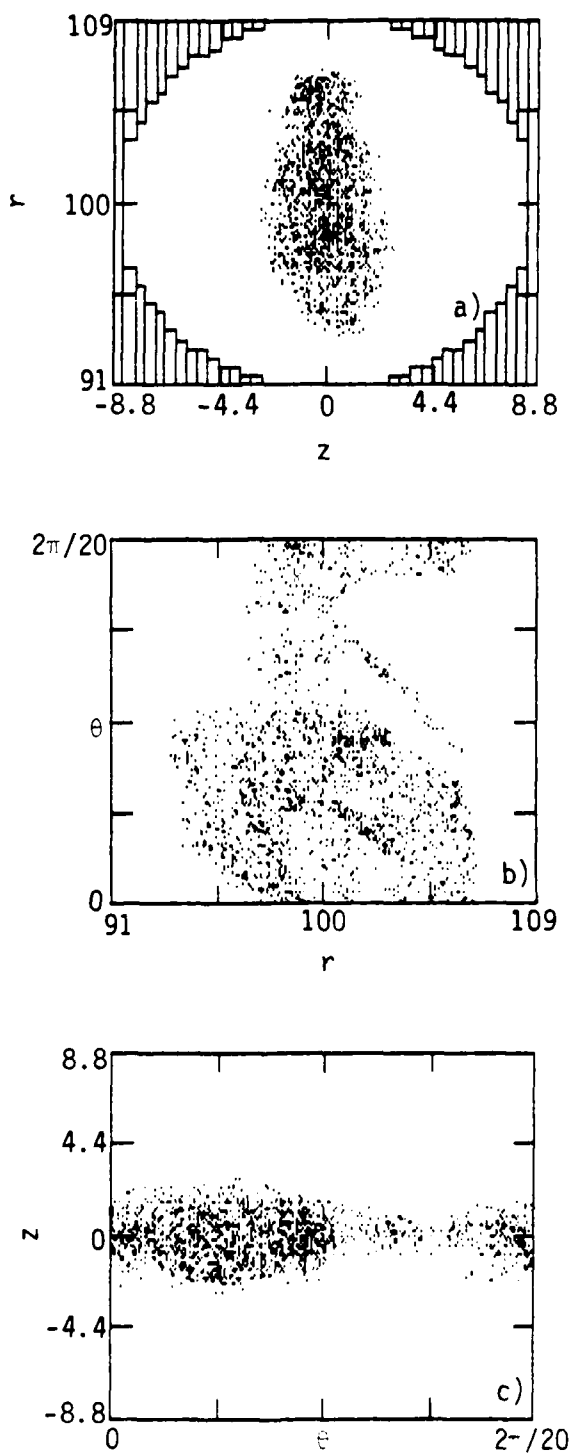


Figure 32. Development of  $\xi = 20$  negative mass instability in the RSL. The radial elongation in (a) is accompanied by the toroidal bunching in (c). ( $I = 10$  kA,  $\gamma = 12$ )

## REFERENCES

1. P. Sprangle, C. A. Kapetanakos, and S. J. Marsh, Proc. 4th International Conf. on High Power Electron and Ion Beams (Palaiseau, France, 1981).
2. G. Barak and N. Rostoker, Phys. Fluids 26, 856 (1983).
3. C. W. Roberson, A. Mondelli and D. Chernin, Phys. Rev. Lett. 50, 507 (1983).
4. S. Humphries, Jr. and D. M. Woodall, Bull. Am. Phys. Soc. 28, 1054 (1983).
5. P. Sprangle and D. Chernin, "Beam Current Limitations Due to Instabilities in Modified and Conventional Betatrons," NRL-5176 (Naval Research Laboratory, Washington, 1983); Part. Accel. 15, 35 (1984).
6. B. B. Godfrey and T. P. Hughes, Phys. Fluids, to be published (1985).
7. T. P. Hughes, B. B. Godfrey, and M. M. Campbell, "Modified Betatron Accelerator Studies," AMRC-R-524 (Mission Research Corporation, Albuquerque, 1983).
8. H. Ishizuka, B. Mandelbaum, A. Fisher, and N. Rostoker, Bull. Am. Phys. Soc. 29, 1430 (1984).
9. P. Sprangle and J. L. Vomvoridis, "Longitudinal and Transverse Instabilities in a High Current Modified Betatron Electron Accelerator," NRL-4688 (Naval Research Laboratory, Washington, 1982).
10. T. P. Hughes, M. M. Campbell, and B. B. Godfrey, IEEE Nuc. Sci. NS-30, 2528 (1983).
11. P. M. Morse and H. Feshbach, Methods of Theoretical Physics (McGraw-Hill, New York, 1953), Part II, Ch. 10.3.
12. M. Abramowitz and I. A. Stegun (eds.), Handbook of Mathematical Functions (U. S. Government Printing Office, Washington, 1964), Ch. 9 and 11.
13. Ref. 12, Eq. 11.4.2.
14. V. K. Neil and A. M. Sessler, Rev. Sci. Instr. 36, 429 (1965).
15. R. W. Landau and V. K. Neil, Phys. Fluids 9, 2412 (1966).
16. R. J. Briggs and V. K. Neil, Plas. Phys. 8, 255 (1966).
17. R. J. Briggs and V. K. Neil, Plas. Phys. 9, 209 (1967).

## REFERENCES

18. R. W. Landau, Phys. Fluids 11, 205 (1968).
19. J. F. Traub, Iterative Methods for the Solutions of Equations (Prentice-Hall, Englewood Cliffs, 1964), Ch. 10.
20. C. A. Kapetanakos, P. Sprangle, D. P. Chernin, S. J. Marsh, and I. Haber, Phys. Fluids 26, 1634 (1984).
21. J. Walsh, B. Johnson, G. Dattoli, and A. Renieri, Phys. Rev. Letters 53, 779 (1984).
22. B. B. Godfrey and T. P. Hughes, IEEE Trans. Nuc. Sci. NS-30, 2531 (1983).
23. J. M. Finn and W. M. Manheimer, Phys. Fluids 26, 3400 (1983).
24. A. Mondelli, D. Chernin, and C. W. Roberson, Proc. Beams '83 Conf., p. 442 (San Francisco, 1983).
25. C. W. Roberson, A. Mondelli and D. Chernin, IEEE Trans. Nuc. Sci. NS-30, 3162 (1983).
26. S. Humphries, Jr., private communication.
27. D. Chernin, A. Mondelli, and C. W. Roberson, Phys. Fluids 27, 2378 (1984).

APPENDIX A

INSTABILITY IN A RELATIVISTIC ELECTRON LAYER  
WITH A STRONG AZIMUTHAL MAGNETIC FIELD

## APPENDIX A

### Instability In A Relativistic Electron Layer With A Strong Azimuthal Magnetic Field

T. P. Hughes and B. B. Godfrey

Mission Research Corporation

Albuquerque NM 87106

#### Abstract

A thin relativistic electron layer immersed in a strong azimuthal magnetic field between two concentric cylindrical conductors is shown to be unstable. The instability is caused by the curvature of the walls, which modifies the interaction between particles in such a way that the inductive (attractive) forces are greater than the electrostatic (repulsive) forces. The growth rate of the instability peaks at long axial wavelengths.

A number of instabilities are known to occur in relativistic, rotating electron layers (Fig. 1), among them the diocotron,<sup>1,2</sup> cyclotron maser,<sup>3</sup> and negative-mass<sup>4-6</sup> instabilities. For these instabilities to occur, it is essential for particles in the layer to be able to move in the radial direction. The instability discussed here differs from those mentioned in that it occurs even in the presence of an infinitely strong azimuthal magnetic field, which prevents any radial motion.

The idealized system we consider consists of an infinitely thin electron layer of radius  $r_b$ , rotating with velocity  $v_0$  between two cylindrical perfectly conducting walls, as shown in Fig. 1. The layer has infinite axial extent, and is immersed in an azimuthal magnetic field which is strong enough to restrict particles to motion along the field lines. No other external fields are applied. The assumption that particles can move only along the magnetic field lines implies that only those forces which act along the field lines need to be considered in the analysis. Thus, the layer's selffields, and immobile neutralizing ions, if present, have no effect on the dynamics. If we let the radius of the layer become infinite while keeping the wall separation  $r_2 - r_1$  constant, so that the geometry becomes planar, then the space-charge oscillations of the electrons along the field-lines are stable. For finite  $r_b$ , however, we show in the following that under certain conditions the space-charge oscillations are unstable. The curvature corrections to the field equations play an essential role in causing the instability.

While the geometry of Fig. 1 is of interest from the point of view of microwave-producing devices and magnetic insulation, our primary motivation in studying it comes from present interest in high current circular accelerators, where a strong magnetic guide field is used to counter the space-charge repulsion of the beam and to suppress negative-mass instabilities.<sup>7</sup> The 2-D geometry of Fig. 1 provides a readily analyzable model of beam dynamics in a strong circular guide field.

We first derive the dispersion relation for the simplest case,  $k=0$ , where  $k$  is the wavenumber along the cylindrical axis, and later state the result for finite  $k$ . We use units in which the electronic charge,  $e$ , and mass,  $m$ , and the velocity of light,  $c$ , have been scaled out. (Velocities are normalized to  $c$ , lengths are normalized to  $c/\omega_0 \equiv 1$  cm, frequencies are normalized to  $\omega_0$ , densities to  $\omega_0^2 m / 4\pi e^2$ , etc.). We use the fluid equations for the density  $n$  and the azimuthal velocity  $v$  to describe the beam dynamics,

$$\frac{\partial n}{\partial t} + \frac{1}{r} \frac{\partial}{\partial \theta} nv = 0, \quad (1)$$

$$\left( \frac{\partial}{\partial t} + \frac{v}{r} \frac{\partial}{\partial \theta} \right) \gamma v = - E_\theta, \quad (2)$$

where  $E_\theta$  is the azimuthal electric field and  $\gamma = (1 - v^2)^{1/2}$ .

For  $k=0$ , transverse-electric (TE) and transverse-magnetic (TM) field components decouple, and we can write down a field equation in which only the  $E_\theta$  field appears. Combining this equation with the perturbed azimuthal current density computed from Eqs. (1) and (2), we obtain the eigenvalue equation

$$\frac{d}{dr} \left[ \frac{1}{\omega^2 - \ell^2/r^2} \frac{1}{r} \frac{d}{dr} \right] r E_\theta + \left( 1 - \frac{n_0}{\gamma_0^3 (\omega - \ell v_0/r)^2} \right) E_\theta = 0, \quad (3)$$

where  $n_0(r)$ ,  $v_0(r)$  denote the beam density and velocity profiles,  $\gamma_0 = (1 - v_0^2)^{-1/2}$ , and we have assumed  $E_\theta \propto \exp(i\ell\theta - i\omega t)$ . We solve this equation by assuming a density profile of the form  $n_0(r) = (2v/r_b) \delta(r - r_b)$  where  $v$  is Budker's parameter (number of particles per unit length times the classical electron radius). Integrating over  $r$ , we obtain a jump condition on  $dE_\theta/dr$ .  $E_\theta$  is continuous across the layer, because there is no radial displacement. Combining this with the boundary conditions on  $E_\theta$ , we obtain the following dispersion relation.

$$(\omega - \ell v_0/r_b)^2 + \pi v \omega^2 / \gamma_0 W_\theta(\omega) = 0 \quad (4)$$

where

$$W_\theta(\omega) = \frac{J'_\ell(\omega r_2) Y'_\ell(\omega r_1) - Y'_\ell(\omega r_1) J'_\ell(\omega r_2)}{\left[ J'_\ell(\omega r_b) Y'_\ell(\omega r_1) - Y'_\ell(\omega r_b) J'_\ell(\omega r_1) \right] \left[ J'_\ell(\omega r_b) Y'_\ell(\omega r_2) - Y'_\ell(\omega r_b) J'_\ell(\omega r_2) \right]}$$

$J_\ell$ ,  $Y_\ell$  are Bessel functions of order  $\ell$ , and primes denote differentiation with respect to the argument. An approximate solution of this equation is obtainable by expanding  $W_0$  about  $r = r_b$ , and using some Bessel function identities.<sup>8</sup> Letting  $r_b - r_1 = a$ ,  $r_2 - r_b = b$ , we expand  $W_0$  to second order in  $wa$ ,  $wb$ , and substitute  $\omega \approx \ell v_0/r_b + i\Gamma$  into the resulting expression. Keeping terms to order  $\Gamma^2$ , we obtain the approximate growth rate,

$$\Gamma^2 = \frac{2vab\ell^2}{r_0^5(a+b)r_b^4} \frac{(r_0^2 b - r_b)(r_0^2 a + r_b)}{r_b - r_0^2(b-a)} \quad (5)$$

In the planar geometry limit,  $r_b \rightarrow \infty$ , keeping  $a, b, \ell/r_b, v/r_b$  fixed, Eq. (5) predicts stability. To get instability, the right side must be positive, which yields the following criterion,

$$r_b/b < r_0^2 < r_b/(b-a). \quad (6)$$

The first half of this inequality is very similar to one derived by Briggs and Neil as the criterion for inductive (as opposed to capacitive) coupling between the beam and the outer wall.<sup>6</sup> The second half of the inequality is approximate, because at  $r_0^2 = r_b/(b-a)$ , the denominator in Eq. (5) vanishes, due to a resonance between the beam and the lowest TE mode. The correct growth rate in the vicinity of this resonance, obtained by keeping terms to order  $\Gamma^3$  in expanding Eq. (4), is

$$\Gamma \approx \sqrt{3} \ell (a^2 b^2 v / (a+b))^{1/3} / 2r_0 r_b^2. \quad (7)$$

As  $\gamma_0^2$  becomes larger than  $r_b/(b-a)$ , Eq. (5) again becomes valid, and the beam is predicted to be stable. The criteria in Eq. (6) imply that for  $a < b$ , the beam is unstable only over a finite range of  $\gamma_0$ , as shown in Fig. 2. The parameters in this figure are  $r_b = 10$  cm,  $a + b = 2$  cm, and  $v = 0.059$ , corresponding to an azimuthal current of 1 kA per cm (for  $v_0 \approx 1$ ). These values are chosen to illustrate the magnitude of the growth rates one would observe in a table-top size experiment. For  $a \geq b$ , there is only a lower bound on the unstable range of  $\gamma_0$ .

For fixed  $\gamma_0$ , Eq. (6) implies that the beam is unstable only within a finite region of the space between the walls, as shown in Fig. 3. As one gets close to the inner or outer wall, the beam becomes stable. The growth rates in Fig. 3 were obtained by numerical solution of Eq. (4) and from the analytic expressions, Eqs. (5) and (7). Equation (5) gives a good approximation for the  $\lambda = 10$  curve except near the resonance point.

The first half of the inequality in Eq. (6) continues to hold even when the expansion in  $w_a$ ,  $w_b$  used to obtain it is no longer valid. Figure 3 shows that for  $\lambda$  as high as 90, the minimum unstable value of  $b$  is given by this inequality. The point of resonance (corresponding to the peaks in Fig. 3), however, is given by  $(b-a)/r_b = 1/\gamma_0^2$  only for  $1 \leq \lambda \leq 10$ . For higher  $\lambda$ , the point of resonance moves towards the outer wall. In Fig. 3, we assume for simplicity that  $\gamma_0$  remains constant as  $r_b$  changes. In

AD-A151 420

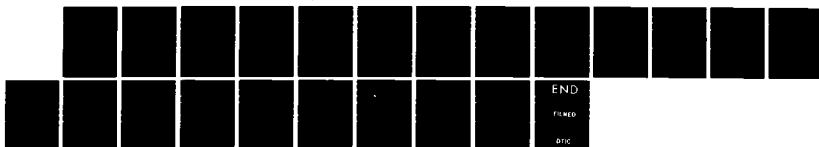
MODIFIED BETATRON ACCELERATOR STUDIES(U) MISSION  
RESEARCH CORP ALBUQUERQUE NM T P HUGHES ET AL. DEC 84  
RMRC-R-655 N60921-84-C-0078

2/2

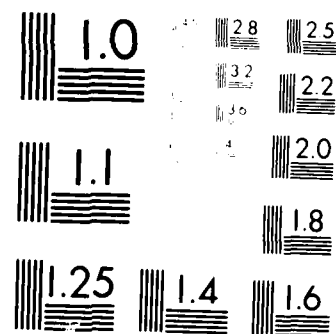
UNCLASSIFIED

F/G 20/7

NL



END  
FILED  
DRIC



MICROCOPY RESOLUTION TEST CHART  
Nikon Microscopy USA, Inc., Melville, NY

practice, space-charge effects can cause  $\gamma_0$  to vary. Also, finite layer-thickness effects are not treated in our model. They are expected to become important when the wavelength  $2\pi r_b/\lambda$  becomes comparable to the layer thickness.

For finite  $k$ , TE and TM field components are coupled. An analysis along the lines of that previously described, but involving considerably more algebra,<sup>9</sup> leads to the following dispersion relation for  $k \neq 0$

$$(\omega - \ell v_0 / r_b)^2 + \frac{\pi v}{\gamma_0 q^2} \left[ \frac{k^2 \ell^2 / r_b^2}{W_z(q)} + \frac{\omega^2 q^2}{W_\theta(q)} \right] = 0 \quad (8)$$

where  $q^2 = \omega^2 - k^2$ ,  $W_\theta$  is defined in Eq. (4), and

$$W_z = \frac{J_\ell(qr_2)Y_\ell(qr_1) - Y_\ell(qr_2)J_\ell(qr_1)}{[J_\ell(qr_b)Y_\ell(qr_1) - Y_\ell(qr_b)J_\ell(qr_1)][J_\ell(qr_b)Y_\ell(qr_2) - Y_\ell(qr_b)J_\ell(qr_2)]}$$

As  $k$  varies from 0 to  $\ell/r_b$ , the growth rate drops, and the energy threshold above which the instability sets in increases, as shown in Fig. 2. This behavior is related to the increasing gap between the beam mode frequency  $\omega \sim \ell v_0 / r_b$  and the TE mode frequency  $\omega \sim (k^2 + \ell^2 / r_b^2)^{1/2}$  as  $k$  increases. For  $k = \ell/r_b$ , the growth rate is zero, but a very weak instability persists for  $k > \ell/r_b$ .

Finally, we make the connection between this work and previous work on the negative-mass instability in electron layers. In the notation of Ref. 5, the imaginary part of the frequency  $\Omega_i$  is given by

$$\Omega_i^2/c^2 = 2\ell v M / \gamma_0 r_b^2 (b_+ + b_-), \quad (9)$$

where  $M$  contains the dynamics of the layer, and  $b_+$ ,  $b_-$  are the "wave admittances". The stability of the layer clearly depends on the sign of both  $M$  and  $b_+ + b_-$ . For  $M < 0$ , Eq. (9) gives the usual negative-mass instability, provided  $b_+ + b_- > 0$ . The fact that one can have  $b_+ + b_- < 0$ , thereby stabilizing the layer, was first pointed out by Briggs and Neil.<sup>6</sup> When a strong azimuthal magnetic field is present, however,  $M > 0$ , and the condition for stability is reversed. The layer is unstable when  $b_+ + b_- < 0$ , i.e., when Eq. (6) is satisfied. The occurrence of the type of instability we have discussed here in a toroidal system, where the analysis is considerably more complex,<sup>10</sup> will be discussed in a future publication.

ACKNOWLEDGEMENT

This work was supported by the Office of Naval Research.

## REFERENCES

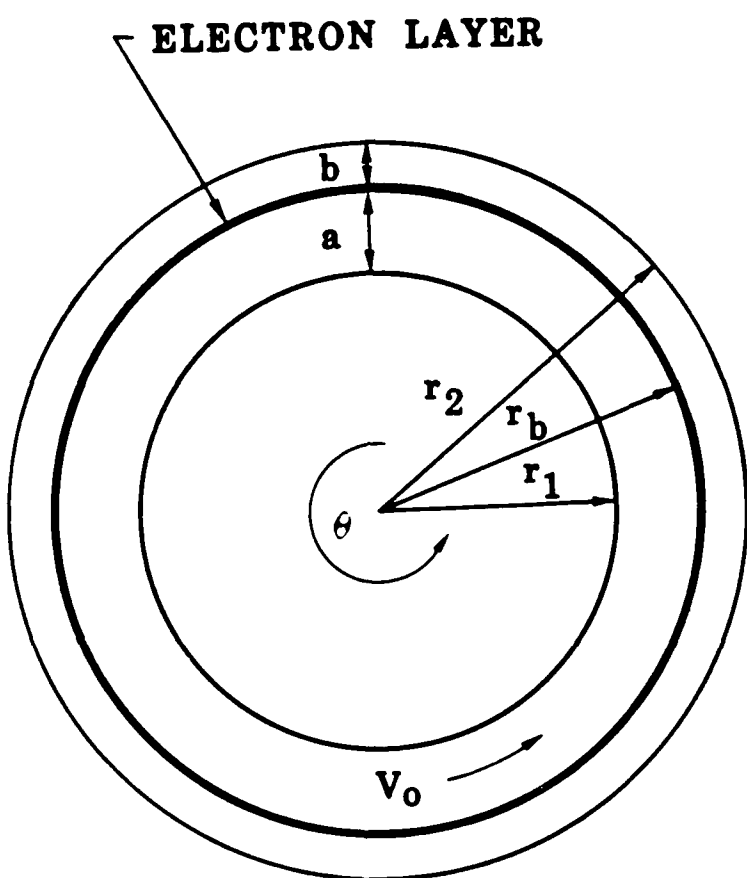
1. R. H. Levy, Phys. Fluids 8, 1288 (1965).
2. V. K. Neil and W. Heckrotte, J. Appl. Phys. 36, 2761 (1965).
3. M. Friedman, D. A. Hammer, W. M. Manheimer and P. Sprangle, Phys. Rev. Lett. 31, 753 (1973).
4. R. W. Landau and V. K. Neil, Phys. Fluids 9, 2412 (1966).
5. Y. Y. Lau and D. Chernin, Phys. Rev. Lett. 52, 1425 (1984); D. Chernin and Y. Y. Lau, Phys. Fluids 27, 2319 (1984), and references therein.
6. R. J. Briggs and V. K. Neil, Plasma Physics 9, 209 (1967).
7. P. Sprangle, C. A. Kapetanakos, and S. J. Marsh, Proc. IVth Intl. Conf. on High Power Electron and Ion Beams (Palaiseau, France, 1981).
8. G. N. Watson, Theory of Bessel Functions (Cambridge University Press, Cambridge, 1966), p. 76.
9. B. B. Godfrey, unpublished.
10. B. B. Godfrey and T. P. Hughes, AMRC-R-655, Mission Research Corporation, Albuquerque, December 1984.

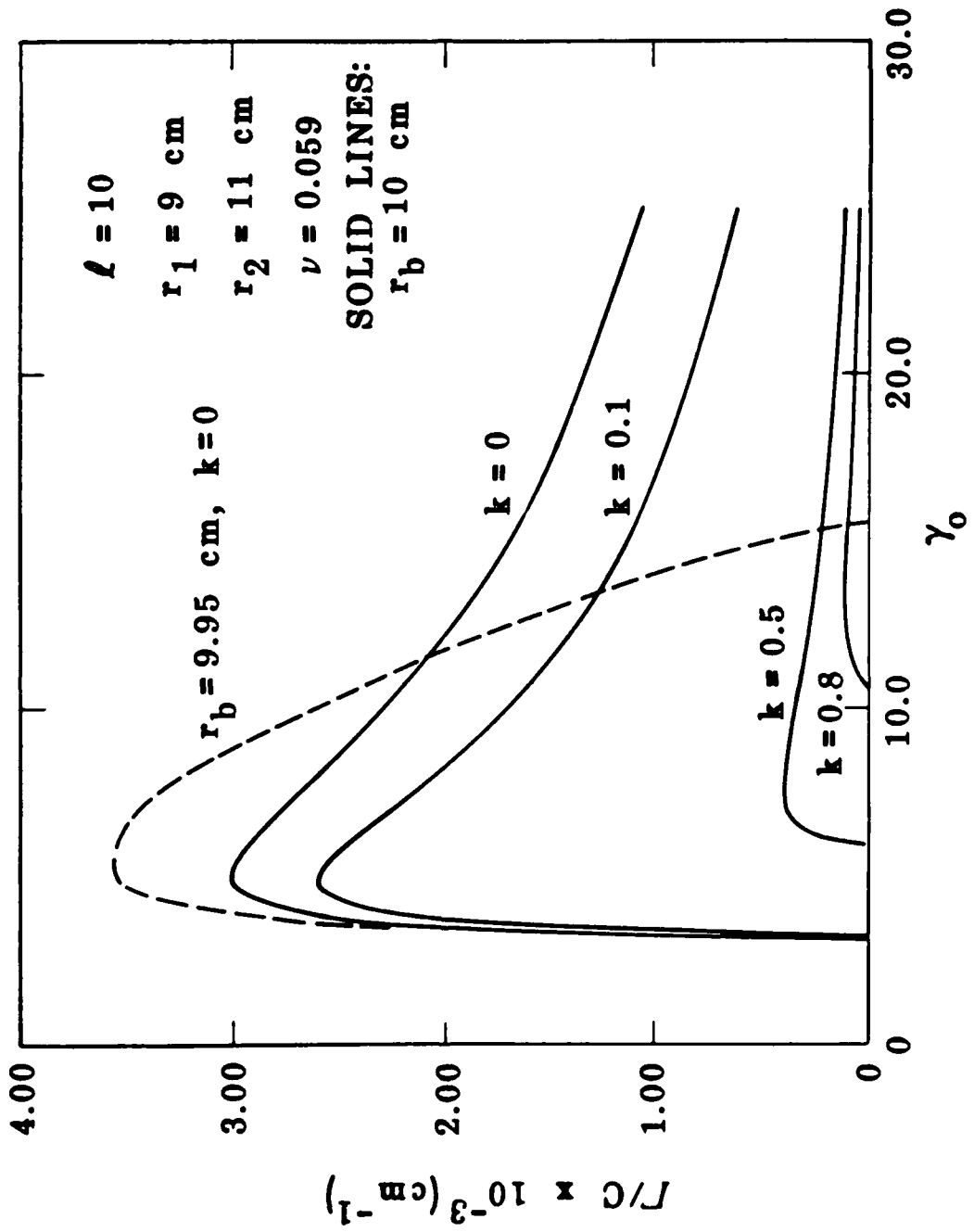
## FIGURE CAPTIONS

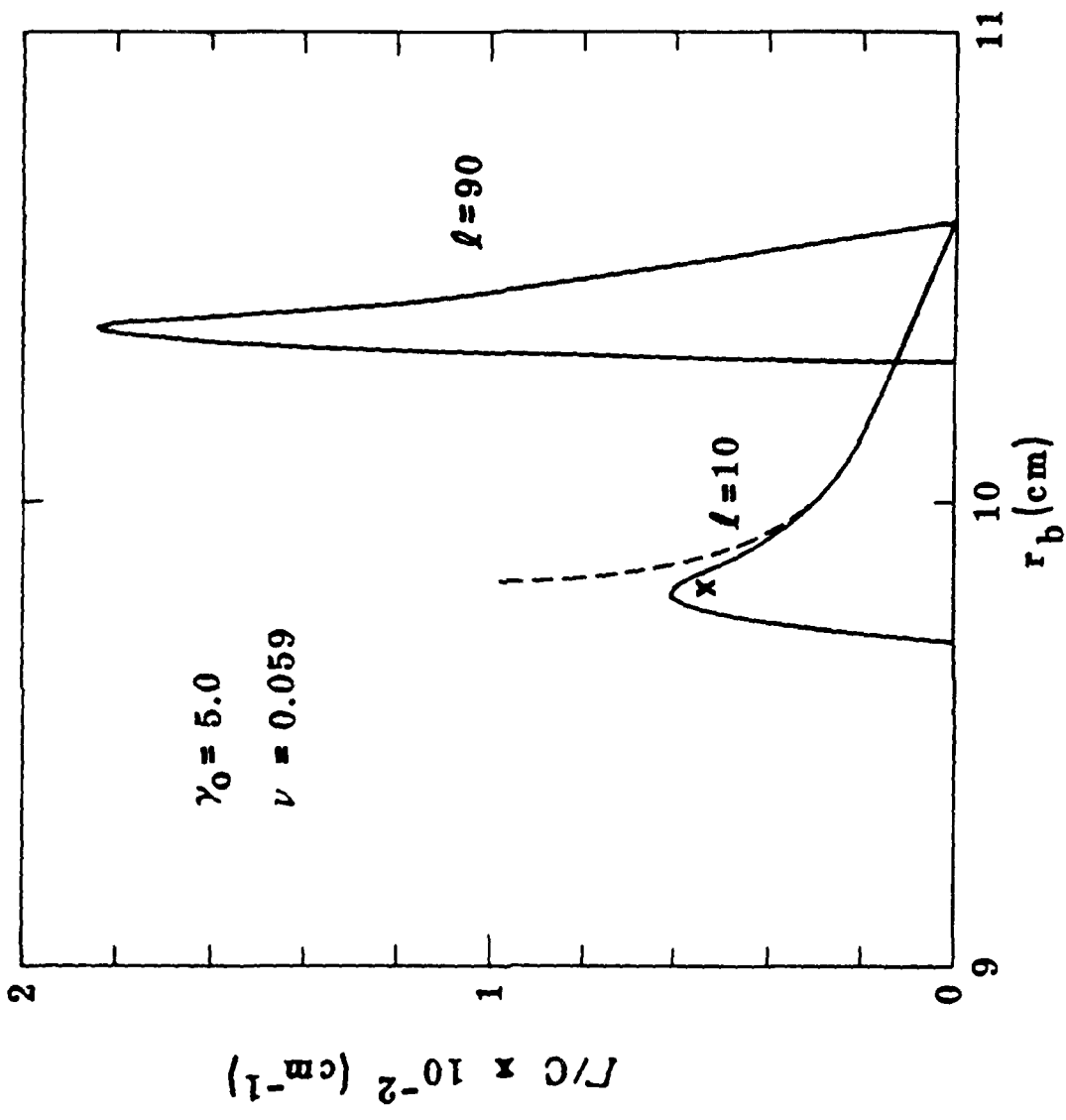
Figure 1. The thin layer of electrons of radius  $r_b$  and infinite axial extent rotates with azimuthal velocity  $v_0$  between two concentric cylindrical conductors.

Figure 2. Growth rate  $\Gamma$  of  $\lambda = 10$  mode versus  $\gamma_0$ . For  $r_b = 9.95$  cm ( $b > a$ ) both an upper and lower cutoff exist. For  $r_b = 10$  cm ( $a = b$ ) only a lower cutoff exists.  $\Gamma$  goes to zero as  $k \rightarrow \lambda/r_b$  ( $= 1.0 \text{ cm}^{-1}$  for this figure).

Figure 3. Instability growth rate as a function of beam position. Solid and dashed lines give numerical and analytic results, respectively. The layer is stable near walls at  $r_1 = 9$  cm and  $r_2 = 11$  cm. The X gives the analytic growth rate at the TE resonance (Eq. (7)).







A-15

## APPENDIX B

### SINGLE-PARTICLE ORBITS IN THE STELLATRON ACCELERATOR

## APPENDIX B

### SINGLE-PARTICLE ORBITS IN THE STELLATRON ACCELERATOR

T. P. Hughes and B. B. Godfrey

Mission Research Corporation

Albuquerque, NM 87106

#### Abstract

The stellatron accelerator provides strong focusing for an intense electron ring through the application of a helical quadrupole magnetic field. Single-particle orbits in this configuration are studied. It is found that for certain initial conditions, the amplitude of the particle orbit increases as the focusing strength is increased. Implications for particle injection into a stellatron are discussed.

## I. INTRODUCTION

The modified betatron device allows one to confine a large current of electrons using a combination of a vertical mirror field  $B_z$  and a toroidal field  $B_t$ . A drawback of this device is that the vertical field must be finely matched to the beam energy  $\gamma$  to keep the beam from drifting off-center and striking the wall. The allowed mismatch is given by

$$\frac{\Delta\gamma}{\gamma} = (1/2 - n_s a^2/b^2) b/r_0 \quad (1)$$

where  $r_0$  is the major radius,  $b$  is the minor radius of the torus  $n_s$  is the self-field index ( $n_s = 2v r_0^2/(a^2\gamma^3)$ , where  $a$  is the beam radius and  $v$  is Budker's parameter). The stellatron configuration<sup>2</sup> adds strong focusing to the modified betatron fields by applying a helical quadrupole magnetic field (Fig. 1). The effect of the strong focusing is to create a deeper and narrower "potential well" in the center of the torus than that supplied by the weak focusing of the vertical field. The allowed mismatch in beam energy is then

$$\frac{\Delta\gamma}{\gamma} = (1/2 - n_s a^2/b^2 + \mu^2(m^2 + mp - 1/2 + n_s a^2/b^2)^{-1}) b/r_0 \quad (2)$$

where  $p$  is the ratio of the toroidal magnetic field to the vertical field,  $\mu$  is the amplitude of the quadrupole field gradient on axis, and  $m$  is the wavenumber of the quadrupole field. By increasing the value of  $\mu$ , the allowable mismatch can become quite large.<sup>2,3</sup>

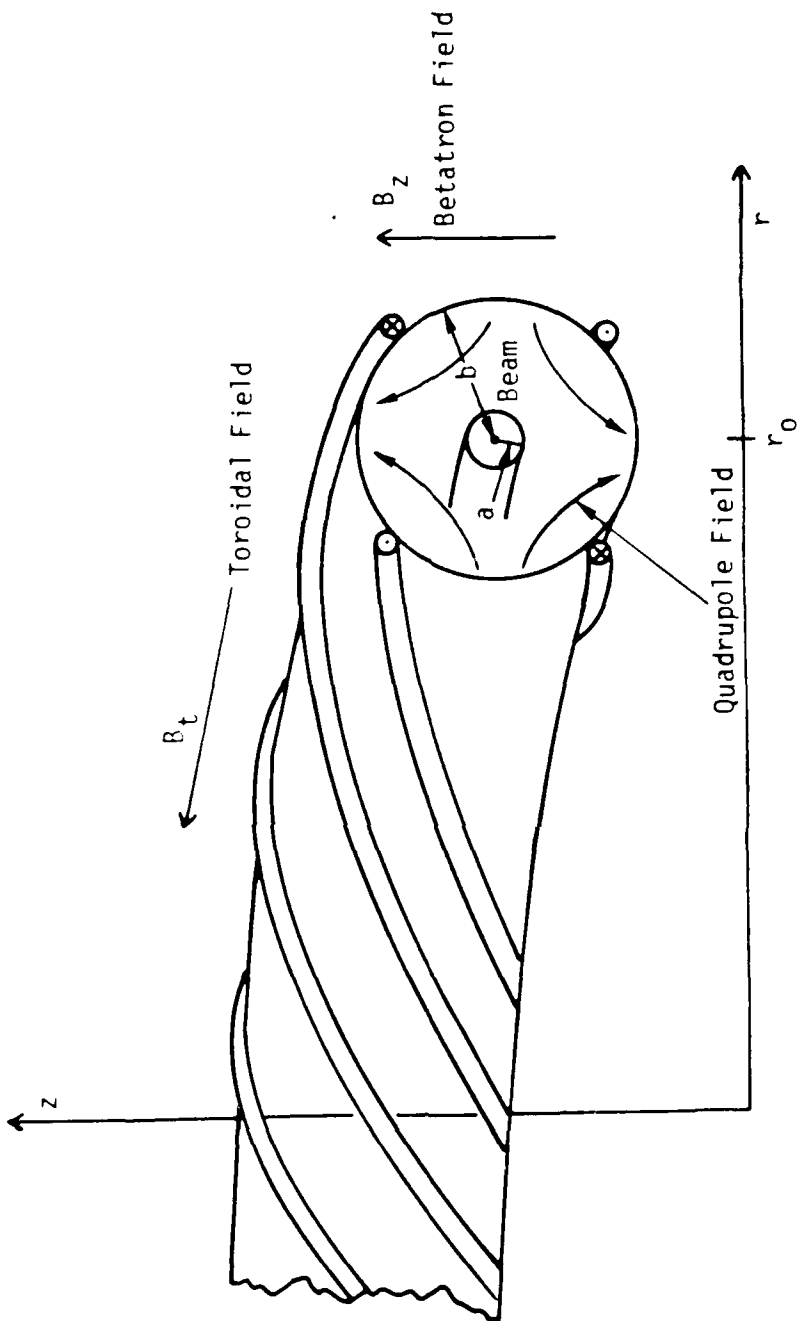


Figure 1. Magnetic field configuration in the stellatron device, showing the superposition of a vertical mirror field, a toroidal guide field, and a helical quadrupole field.

In order to look at the effect of the stellatron fields on individual particles, rather than on the beam centroid, we take the linearized equations of motion for a single particle and compute the general solution (Sec. II). In Sec. III, we obtain the amplitude of the orbits for some specific conditions, and in Sec. IV show how the amplitude depends on the strength of the focusing field. These results are compared to results from a code which numerically integrates the equations of motion.

### II. GENERAL SOLUTION OF LINEAR PARTICLE EQUATIONS

The stellatron magnetic fields are those of the modified betatron, namely, the vertical field  $B_z$  and toroidal field  $B_t$ , together with a helical quadrupole field of the form

$$\begin{aligned} B_r &= \frac{1}{2} \epsilon m B_t (\tilde{z} \cos m\theta - \tilde{r} \sin m\theta) \\ B_z &= \frac{1}{2} \epsilon m B_t (\tilde{z} \sin m\theta + \tilde{r} \cos m\theta) \end{aligned} \quad (3)$$

where  $\tilde{r}$ ,  $\tilde{z}$  denote deviations of the particle positions from  $r = r_0$ ,  $z = 0$ , and  $\epsilon = 2\mu/m_p$ . From Ref. 2, the linearized single particle equations of motion in these fields are

$$\begin{aligned} \ddot{\tilde{r}} + \left(\frac{1}{2} - n_s\right) \omega_0^2 \tilde{r} - \Omega \dot{\tilde{z}} + \mu \omega_0^2 \cos m\theta \tilde{r} + \mu \omega_0^2 \sin m\theta \tilde{z} &= 0 \\ \ddot{\tilde{z}} + \left(\frac{1}{2} - n_s\right) \omega_0^2 \tilde{z} + \Omega \dot{\tilde{r}} - \mu \omega_0^2 \cos m\theta \tilde{z} + \mu \omega_0^2 \sin m\theta \tilde{r} &= 0 \end{aligned} \quad (4)$$

where  $\omega_0 = B_z/\gamma$ ,  $\Omega = B_t/\gamma$ . Letting  $\tilde{r} + i\tilde{z} = \xi e^{im\theta/2}$ , where  $m$  is an even integer, we obtain

$$\ddot{\xi} + i(\Omega + m\omega_0) \dot{\xi} + \omega_0^2 \left( \frac{1}{2} - n_s - \frac{mp}{2} - \frac{m^2}{4} \right) \xi + \mu\omega_0^2 \xi^* = 0 \quad (5)$$

Next, suppose  $\xi = \sum_{\pm} a_{\pm} e^{-iv_{\pm}t} + b_{\pm} e^{iv_{\pm}t}$ , where  $a_{\pm}$ ,  $b_{\pm}$  are complex numbers, then we obtain as in Ref. 2,

$$\frac{v_{\pm}^2}{\omega_0^2} = \frac{1}{2} - n_s + \frac{1}{4} p^2 + \frac{1}{4} (m + p)^2 \pm [(\frac{1}{2} - n_s + \frac{1}{4} p^2)(m + p)^2 + \mu^2]^{1/2} \quad (6)$$

The orbit is stable provided  $v_{\pm}$  are real. The coefficients  $a_{\pm}$ ,  $b_{\pm}$  are related by

$$b_{\pm} = a_{\pm}^* \frac{\mu\omega_0^2}{\frac{v_{\pm}^2}{\omega_0^2} + v_{\pm} \omega_0 (p + m) - \omega_0^2 (\frac{1}{2} - n_s - \frac{1}{2} mp - \frac{1}{4} m^2)} \equiv \beta_{\pm} a_{\pm}^* \quad (7)$$

The general solution can then be written as

$$\xi = \sum_{\pm} a_{\pm} e^{-iv_{\pm}t} + \beta_{\pm} a_{\pm}^* e^{iv_{\pm}t} \quad (8)$$

To see what kind of geometric shape this represents, write  $a_{\pm}$  as  $\alpha_{\pm} e^{iv_{\pm}t_{\pm}}$  where the  $\alpha_{\pm}$  are real numbers. Then we obtain

$$\tilde{r} + i\tilde{z} = \exp(im\omega_0 t/2) \sum_{\pm} \alpha_{\pm} [(\beta_{\pm} + 1) \cos v_{\pm}(t - t_{\pm}) + i(\beta_{\pm} - 1) \sin v_{\pm}(t - t_{\pm})] \quad (9)$$

Thus, in a frame rotating as  $\exp(i\omega_0 t/2)$ , the typical orbit is a sum of two ellipses with major axes  $|\alpha_{\pm}(\beta_{\pm}+1)|$  and minor axes  $|\alpha_{\pm}(\beta_{\pm}-1)|$ . From this way of visualizing the orbits, we can at once conclude that the amplitude of the orbit  $|\xi|$  satisfies

$$\begin{aligned} & \min\{||\alpha_+(\beta_++1)| - |\alpha_-(\beta_-+1)||, ||\alpha_+(\beta_+-1)| - |\alpha_-(\beta_--1)||\} \leq |\xi| \\ & \leq \max\{|\alpha_+(\beta_++1)| + |\alpha_-(\beta_-+1)|, |\alpha_+(\beta_+-1)| + |\alpha_-(\beta_--1)|\} \end{aligned} \quad (10)$$

### III. INITIAL CONDITIONS

The general particle orbit above involves four unknown constants  $\alpha_{\pm}$  and  $t_{\pm}$ . By specifying initial conditions, we can determine these constants. We look at two simple cases.

Case a). Suppose that at  $t = 0$  the particle is at position  $r = |\xi_0|$ ,  $z = 0$ ,  $\theta = 0$ , and the transverse velocities are zero. Then we obtain  $t_{\pm} = 0$ , and

$$\alpha_+ = |\xi_0| \{v_-(\beta_- - 1) + \frac{m\omega_0}{2} (\beta_- + 1)\} / D, \quad \alpha_- = |\xi_0| \{v_+(\beta_+ - 1) + \frac{m\omega_0}{2} (\beta_+ + 1)\} / D$$

where

$$D = (\beta_+ + 1)[v_-(\beta_- - 1) + \frac{m\omega_0}{2} (\beta_- + 1)] - (\beta_- + 1)[v_+(\beta_+ - 1) + \frac{m\omega_0}{2} (\beta_+ + 1)] \quad (11)$$

For the particular initial conditions chosen, we can make the following ad hoc arguments about the amplitude of the orbit. Since the particle has zero radial velocity initially, it is at one of the radial turning points of the orbit. (Here we are using the term radial to refer to  $|\xi|$ ). Further, since the quadrupole focusing force on the particle is inward at its initial coordinates, we infer that the turning point in question is the outer turning point. Therefore, for these initial conditions, the orbit amplitude obeys

$$\min\{||\alpha_+(\beta_++1)| - |\alpha_-(\beta_-+1)||, ||\alpha_+(\beta_+-1)| - |\alpha_-(\beta_--1)||\} \leq |\xi| \leq |\xi_0| \quad (12)$$

where  $\alpha_{\pm}$  are given by Eq. (11).

Case b). Now let us consider a particle initially at  $r = 0, z = |\xi_0|, \theta = 0$ , again with zero transverse velocities. The particle is again at a turning point, but, assuming the quadrupole force is stronger than the weak focusing force, the initial net force on the particle is outward. Therefore the initial position is at an inner turning point, and  $|\xi|$  obeys

$$|\xi_0| \leq |\xi| \leq \max\{|\alpha_+(\beta_++1)| + |\alpha_-(\beta_-+1)|, |\alpha_+(\beta_+-1)| + |\alpha_-(\beta_--1)|\} \quad (13)$$

where  $\alpha_{\pm}$  are given by Eq. (11) above with the replacement  $\pm 1 \rightarrow \mp 1$ .

If we were to start the particle off at a toroidal position  $m\theta = \pi/2$  instead of  $\theta = 0$ , then the behavior of the two cases described above becomes interchanged. The particle initially at  $r = |\xi_0|, z = 0$  obeys Eq. (13), and the one at  $r = 0, z = |\xi_0|$  obeys Eq. (12). This is because the quadrupole fields have rotated 90 degrees.

#### IV. RESULTS

It can be seen from Eqs. (12) and (13) that the amplitude of the particle motion is a function of the strength of the quadrupole field, i.e., of  $\epsilon$ . To see the implications of this we take some typical stellatron parameters ( $r_0 = 1$  m,  $B_t = 5$  kG,  $\gamma = 7$ ,  $m = 20$ ), and plot the turning points obtained from these equations versus  $\epsilon$  (Fig. 2). For case b), the outer turning radius increases monotonically with  $\epsilon$ , so that the orbit can intersect the wall, even though the particle motion is "stable" ( $v_\pm^2 > 0$ ). The numerical integration of Eq. (4) for the parameters in Fig. 2 with  $\epsilon = 1$  gives the orbits shown in Fig. 3. The inner and outer turning points in this figure agree well with the analytical results of Fig. 2. Cases a) and b) are limiting cases. For particles with the same initial value of  $|\xi_0|$  as a) and b), but different  $\tilde{r}, \tilde{z}$  values, the turning points lie within the bounds shown in Fig. 2.

As one would expect, the bounds on the particle orbits are linearly proportional to the initial value of  $|\xi_0|$ . Apart from this, we have not tried to extract any simple scalings for the amplitudes.

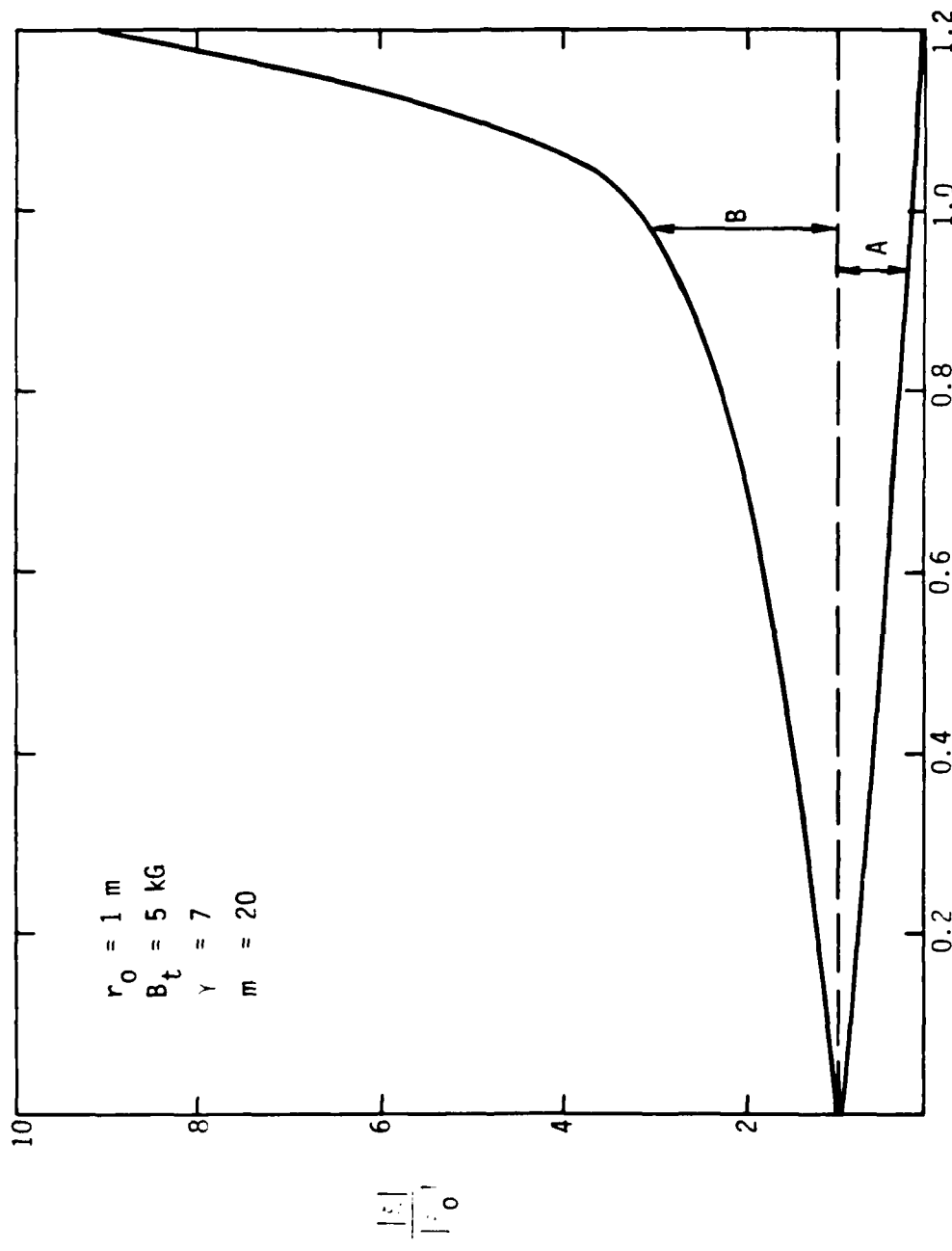
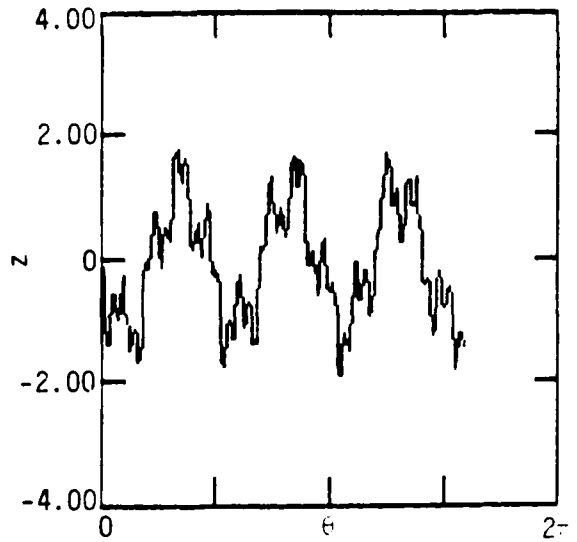
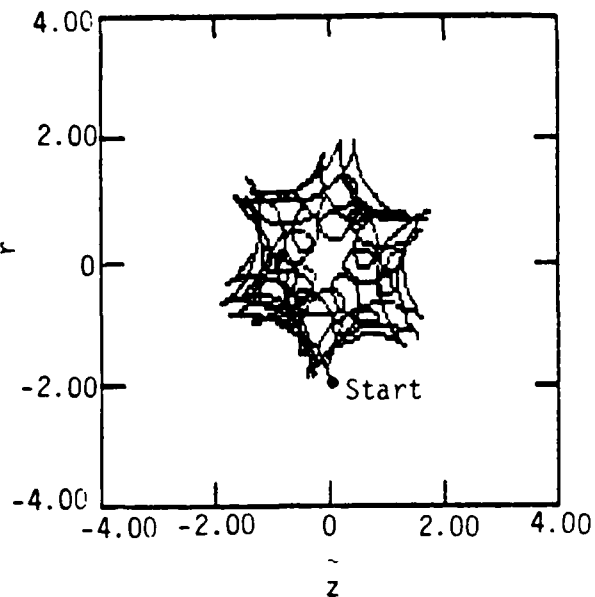
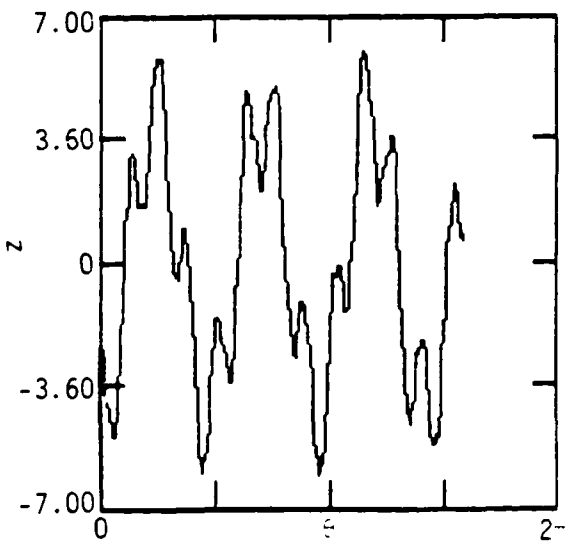
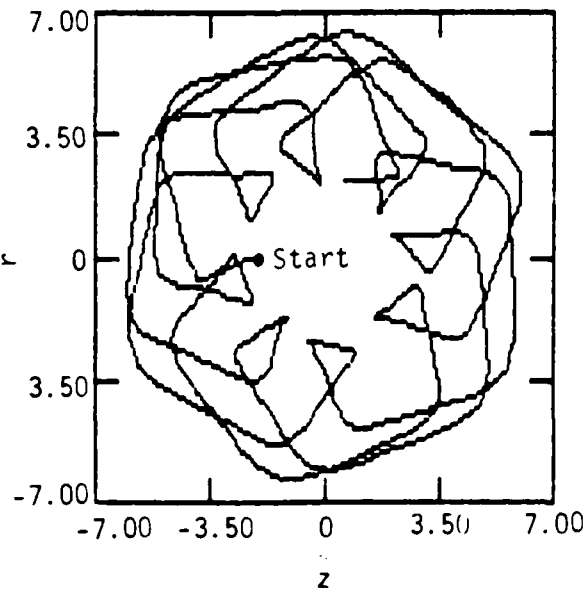


Figure 2. Dependence of amplitude of particle orbits on strength of quadrupole field, as measured by  $\xi$ . For initial conditions of case (a) (see text), the particle oscillates over the range denoted by A, for case (b) the particle oscillates over the range B.



a)



b)

Figure 3. Numerically integrated orbits of particles which start at a)  
 $\dot{r} = -2 \text{ cm}, \dot{z} = 0, \dot{\theta} = 0$ , b)  $z = -2 \text{ cm}, \dot{r} = 0, \dot{\theta} = 0$ . Note that  
the dimensions of the boxes are different for a) and b).

It is clear from the results presented that the initial conditions, as well as energy mismatch, must be considered in determining whether a particle is confined or not. This has practical implications for injection of particles into a stellatron. In the University of California at Irvine experiment, the injector is located inside the torus, offset some distance  $r_1$  from the center of the minor cross section. In order to create a beam of the smallest possible radius, the injector should be located at a toroidal location corresponding to case a) above, i.e., where the focusing of the quadrupole field in the  $r$  direction is a maximum. In that case, the beam will have a radius no larger than  $r_1$ .

Finally, it should be noted that while orbit amplitudes can put an upper bound on the strength of the quadrupole focusing, one can achieve substantial improvement in the energy mismatch characteristics of the device without approaching this upper bound. Thus, from Fig. 2 we see that for  $\epsilon = 0.5$ , a particle will, at worst, make excursions to 1.6 times its initial amplitude. As shown in Ref. 2, however, this value of  $\epsilon$  allows 50% energy mismatch without loss of confinement.

7

REFERENCES

1. P. Sprangle, C. A. Kapetanakos, and S. J. Marsh, Proc. 4th Intl. Conf. on High Power Electron and Ion Beams (Palaiseau, France, 1981).

2. C. W. Roberson, A. Mondelli, and D. Chernin, Phys. Rev. Lett. 50, 507 (1983).

3. A. Mondelli, D. Chernin, and C. W. Roberson, Proc. 5th Intl. Conf. on High Power Particle Beams (San Francisco, CA, 1983), p. 442.

**END**

**FILMED**

**5-85**

**DTIC**